


Spring 5-2010

Nanomaterials From Biologically Active Molecules: Self-Assembly and Molecular Recognition

Min Yu

University of Southern Mississippi

Follow this and additional works at: <https://aquila.usm.edu/dissertations>

 Part of the [Materials Chemistry Commons](#), and the [Polymer Chemistry Commons](#)

Recommended Citation

Yu, Min, "Nanomaterials From Biologically Active Molecules: Self-Assembly and Molecular Recognition" (2010). *Dissertations*. 919.

<https://aquila.usm.edu/dissertations/919>

This Dissertation is brought to you for free and open access by The Aquila Digital Community. It has been accepted for inclusion in Dissertations by an authorized administrator of The Aquila Digital Community. For more information, please contact Joshua.Cromwell@usm.edu.

The University of Southern Mississippi

NANOMATERIALS FROM BIOLOGICALLY ACTIVE MOLECULES:
SELF-ASSEMBLY AND MOLECULAR RECOGNITION

by

Min Yu

Abstract of a Dissertation
Submitted to the Graduate School
of The University of Southern Mississippi
in Partial Fulfillment of the Requirements
for the Degree of Doctor of Philosophy

May 2010

ABSTRACT

NANOMATERIALS FROM BIOLOGICALLY ACTIVE MOLECULES:

SELF-ASSEMBLY AND MOLECULAR RECOGNITION

by Min Yu

May 2010

This dissertation describes the development of molecular assemblies and molecular recognition of phospholipids (PLs) that exhibit potential applications in emerging nanotechnologies. It consists of two parts: (1) structural features of PLs responsible for recognition of synthetic copolymers, and (2) design, synthesis and analysis of magnetic nanotubes obtained from PLs with a common theme of colloidal synthesis served as a platform for film formation and nano-assemblies of nanotubes. Poly(methyl methacrylate/*n*-butyl acrylate) (p-MMA/nBA) colloidal particles that were stabilized by 1,2-dilauroyl-*sn*-glycero-3-phosphocholine (DLPC) PLs were synthesized, and upon the particle coalescence, PL stratification resulted in the formation of surface localized ionic clusters (SLICs). These entities were capable of recognizing MMA/nBA monomer interfaces along the p-MMA/nBA copolymer backbone and forming crystalline SLICs at the monomer interface. Utilizing spectroscopic analysis combined with *ab initio* calculations, we determined the nature of their interactions, where the two neighboring MMA and nBA units along the polymer backbone provided conducive environments to signal and attract amphiphilic groups of DLPC, thus initiating SLIC formation. Further studies were conducted on synergistic stimuli-responsive behaviors of p-MMA/nBA colloidal dispersions in the presence of sodium dioctyl sulfosuccinate (SDOSS) and DLPC. Spectroscopic analysis of p-MMA/nBA colloidal dispersions revealed the

formation and the preferential orientation of SLICs at the film-air (F-A) or film-substrate (F-S) interfaces in response to the combined stimulus effects.

Using bioactive 1,2-bis(10,12-tricosadiynoyl)-sn-glycero-3-phosphocholine (DC_{8,9}PC) nanotube-forming PL as templates, concentric ferromagnetic iron oxide-carbon-iron oxide nanotubes (FMNTs) were synthesized. Their structural and morphological features were further investigated by utilizing x-ray diffraction, selected area electron diffraction, high-resolution transmission electron microscopy, and Mössbauer spectroscopy, which revealed that concentric magnetite (Fe₃O₄)/carbon/magnetite multilayer structures, where the carbon layer was sandwiched between two magnetite layers as well as magnetite was present inside the carbon interlayer. Furthermore, using the synthetic approaches, controllable and uniform diameter, wall thickness, and length of FMNTs were obtained. Further studies focused on the surface modifications of different nano-objects such as C₆₀, multi-walled carbon nanotubes, FMNTs, and carbon fibers, which resulted in inhibition of gram positive bacteria and cytotoxicity. This was accomplished by utilizing microwave plasma reactions of maleic anhydride as well as attaching polyethylene glycol spacer and penicillin.

COPYRIGHT BY

MIN YU

2010

ACKNOWLEDGEMENTS

I would like to thank my research advisor, Dr. Marek Urban, for his kindly guidance, support, and encouragement during my graduate studies. Through his guidance and leadership, he empowered me with the creative ability in scientific research. His insightful comments and scientific suggestions during my research work allowed me to obtain numerous knowledge and thoughts that will benefit me throughout my professional career. I would also like to appreciate him for acquiring the funding necessary to support me through the Ph.D. program in Polymer Science and Engineering.

I would also like to thank my graduate committee members Dr. Kenneth Mauritz, Dr. Sara Morgan, Dr. Jeffrey Wiggins, and the late Dr. Charles Hoyle for their advice and support throughout my graduate studies.

In addition, I would like to appreciate Dr. Yanling Guo, Dr. Jaegab Lee (Kookmin University), Dr. Yinghong Sheng (Florida Gulf Coast University), Dr. Jane Hou (Oak Ridge National Lab), and Dr. James Weston (University of Alabama) for advisement in collaboration works.

Special appreciation goes to the Urban Research Group for their friendship and great support. Financially, this work was supported primarily by the National Science Foundation Materials Research Science Engineering Center (NSF MRSEC) program under award number DMR 0213883.

TABLE OF CONTENTS

ABSTRACT.....	ii
ACKNOWLEDGEMENTS.....	iv
LIST OF ILLUSTRATIONS.....	vii
LIST OF TABLES.....	xiii
INTRODUCTION.....	1
CHAPTER	
I. MOLECULAR RECOGNITION AND PHOSPHOLIPID SELF-ASSEMBLY.....	5
Introduction	
Molecular Recognition	
Phospholipid Self-Assembly	
Magnetic Nanotubes	
References	
II. MOLECULAR RECOGNITION AT METHYL METHACRYLATE/N-BUTYL ACRYLATE (MMA/NBA) MONOMER UNIT BOUNDARIES OF PHOSPHOLIPIDS AT P-MMA/NBA COPOLYMER SURFACES.....	40
Introduction	
Experimental	
Results and Discussion	
Conclusions	
References	
III. STIMULI-RESPONSIVE STRATIFICATION OF PHOSPHOLIPIDS ACROSS P-MMA/NBA FILMS CONTROLLED BY SYNERGISTIC EFFECTS OF PH, IONIC STRENGTH AND ENZYME LEVELS.....	63
Introduction	
Experimental	
Results and Discussion	
Conclusions	
References	

IV. CONCENTRIC FERROMAGNETIC NANOTUBES FROM BIOLOGICALLY ACTIVE PHOSPHOLIPIDS	
PART I: SYNTHESIS.....	84
Introduction	
Experimental	
Results and Discussion	
Conclusions	
References	
Part II: STRUCTURAL AND MORPHOLOGICAL FEATURES.....	96
Introduction	
Experimental	
Results and Discussion	
Conclusions	
References	
V. MORPHOLOGICAL CONTROL OF FERROMAGNETIC NANOTUBES: WALL THICKNESS, DIAMETER, AND LENGTH.....	119
Introduction	
Experimental	
Results and Discussion	
Conclusions	
References	
VI. FORMATION OF ANTIBACTERIAL SURFACES ON CARBON BASED NANOMATERIALS: THE EFFECT OF ANTIBIOTICS ON CYTOTOXICITY	139
Introduction	
Experimental	
Results and Discussion	
Conclusions	
References	
VII. CONCLUDING REMARKS.....	156

LIST OF ILLUSTRATIONS

Figure

1.1. Interactions between PL and a transmembrane α -helix in a lipid bilayer ³⁴	23
1.2. Structure of a phospholipid.....	24
1.3. Aggregation forms of the amphiphilic molecules in water: (A) micelle; (B) bilayer; (C) liposome ³⁸	25
1.4. Schematic process of emulsion polymerization ⁴⁰	26
1.5. TEM micrograph of the acorn-shaped morphology of the synthesized colloidal particles (A) and an optical image of acorns from nature (B) ⁴⁴	27
1.6. TEM micrographs of p-MMA/nBA containing DCPC using extrusion polymerization ⁴⁶	28
1.7. Schematic diagram illustrating the mobility of SDOSS/DLPC and DLPC stabilizing components to the F-A and F-S interfaces in response to temperature, ionic strength, pH and phospholipase A ₂ changes ⁴⁸	29
1.8. Proposed formation mechanism of lipid tubules resulting from chiral molecular self-assembly ⁶⁵	30
1.9. Schematic diagram of Ar microwave plasma reactions in the presence of maleic anhydride leading to the formation of -COOH groups, followed by PEG attachment and bioactive molecules to functionalized surfaces ^{118,122-124}	31
2.1. Cross-polarized optical micrographs of DLPC stabilized p-MMA/nBA film surfaces recorded from the F-A interface.....	54
2.2. Polarized ATR-FTIR spectra of p-MMA/nBA copolymer films containing DLPC at: (A) F-A, TE polarization; (A') F-A, TM polarization; (B) F-S, TE polarization; (B') F-S, TM polarization; and reference sample: (C) p-MMA/nBA copolymer containing SDOSS/DLPC; (D) DLPC, and (E) p-MMA/nBA copolymer containing SDOSS.....	55
2.3. Schematic diagram depicting interactions between DLPC and SDOSS.....	56
2.4. ATR-FTIR spectra of DLPC stabilized p-MMA and p-nBA recorded from the F-A interface: (A) p-MMA/p-nBA blend, TE polarization; (A') p-MMA/p-nBA blend, TM polarization; (B) p-MMA, TE polarization; (B') p-MMA, TM polarization; (C) p-nBA, TE polarization; (C') p-nBA, TM polarization.....	57

2.5.	Proposed SLIC models resulting from the interaction between copolymer components and DLPC: (A) p-MMA/nBA copolymer; (A') 3D localized p-MMA/nBA copolymer–phospholipid interactions; (A'') 3D model of SLICs; (B) p-MMA homopolymer; (B') 3D localized p-MMA homopolymer–phospholipid interactions; (C) p-nBA homopolymer; (C') 3D localized nBA homopolymer–phospholipid interactions; (D) p-MMA/p-nBA blend; (D') 3D localized p-MMA/p-nBA blend-phospholipid interactions.....	58
2.6.	Comparison of (A) combined TE and TM polarized ATR-FTIR spectrum of DLPC stabilized p-MMA/nBA collected from the F-A interface; (B) Calculated IR spectrum from the Model A in Figure 2.5, (C) Calculated IR spectrum from the Model D in Figure 2.5.....	59
2.7.	Selected area diffraction images of: (A) DLPC; (B) p-MMA/nBA polymer containing SDOSS; (C) p-MMA/nBA containing DLPC; (D) proposed crystal lattice models for SLICs.....	60
3.1.	Cross-polarized optical micrographs of SDOSS/DLPC stabilized p-MMA/nBA films recorded from F-A and F-S interfaces at (A1) F-A; (A2) F-S; (B1) F-A, 0.5/1.0 CaCl ₂ /DLPC, PLA ₂ ; (B2) F-S, 0.5/1.0 CaCl ₂ /DLPC, PLA ₂ ; (C1) F-A, 1.0/1.0 CaCl ₂ /DLPC, PLA ₂ ; (C2) F-S, 1.0/1.0 CaCl ₂ /DLPC, PLA ₂	74
3.2.	Polarized ATR-FTIR spectra at F-A interface (2A) and F-S interface (2B) of p-MMA/nBA copolymer films containing SDOSS/DLPC: (A) TE; (A') TM, and colloidal dispersions treated with CaCl ₂ /DLPC molar ratios: (B) 0.5/1.0, TE; (B') 0.5/1.0, TM; (C) 1.0/1.0, TE; (C') 1.0/1.0, TM in the presence of PLA ₂	75
3.3.	Analysis of colloidal residue of p-MMA/nBA dispersions containing DLPC treated with CaCl ₂ /DLPC molar ratios: (A) 0.5/1.0 CaCl ₂ /DLPC; (B) 1.0/1.0 CaCl ₂ /DLPC in the presence of PLA ₂ including TEM images (A1) and (B1), IRIRI images (A2) and (B2), and IR spectra (A3) and (B3).....	76
3.4.	Schematic diagram depicting preferentially oriented manifestations at the F-A and F-S interfaces of SDOSS/DLPC and DLPC stabilized p-MMA/nBA copolymer prepared in the presence of CaCl ₂ /DLPC molar ratios and PLA ₂	77
3.5.	A. Polarized ATR-FTIR spectra at F-A interface of p-MMA/nBA copolymer films containing SDOSS/DLPC treated with PLA ₂ and 0.5/1.0 CaCl ₂ /DLPC and adjusted to pH: (A) 2.0, TE; (A') 2.0, TM (B) 5.0, TE; (B') 5.0, TM; (C) 8.0, TE; (C') 8.0, TM. B. Polarized ATR-FTIR spectra at F-S interface of p-MMA/nBA copolymer films containing SDOSS/DLPC treated with PLA ₂ and 0.5/1.0 CaCl ₂ /DLPC and adjusted to pH: (A) 2.0, TE; (A') 2.0, TM (B) 5.0, TE; (B') 5.0, TM; (C) 8.0, TE; (C') 8.0, TM.....	78

3.6. A. Polarized ATR-FTIR spectra at F-A interface of p-MMA/nBA copolymer films containing SDOSS/DLPC treated with PLA ₂ and 1.0/1.0 CaCl ₂ /DLPC and adjusted to pH: (A) 2.0, TE; (A') 2.0, TM (B) 5.0, TE; (B') 5.0, TM; (C) 8.0, TE; (C') 8.0, TM. B. Polarized ATR-FTIR spectra at F-S interface of p-MMA/nBA copolymer films containing SDOSS/DLPC treated with PLA ₂ and 1.0/1.0 CaCl ₂ /DLPC and adjusted to pH: (A) 2.0, TE; (A') 2.0, TM (B) 5.0, TE; (B') 5.0, TM; (C) 8.0, TE; (C') 8.0, TM.....	79
3.7. A. Polarized ATR-FTIR spectra at F-A interface of DLPC stabilized p-MMA/nBA copolymer films (A) TE; (A') TM, and treated with PLA ₂ and various ratios of CaCl ₂ /DLPC and adjusted to pH 8: (B) 0.5/1.0 CaCl ₂ /DLPC, TE; (B') 0.5/1.0 CaCl ₂ /DLPC, TM; (C) 1.0/1.0 CaCl ₂ /DLPC, TE; (C') 1.0/1.0 CaCl ₂ /DLPC, TM. B. Polarized ATR-FTIR spectra at F-S interface of DLPC stabilized p-MMA/nBA copolymer films (A) TE; (A') TM, and treated with PLA ₂ and various ratios of CaCl ₂ /DLPC and adjusted to pH 8: (B) 0.5/1.0 CaCl ₂ /DLPC, TE; (B') 0.5/1.0 CaCl ₂ /DLPC, TM; (C) 1.0/1.0 CaCl ₂ /DLPC, TE; (C') 1.0/1.0 CaCl ₂ /DLPC, TM.....	80
3.8. Schematic diagram depicting molecular-level interactions between SDOSS and DLPC species in the presence of Ca ²⁺ and PLA ₂	81
3.9. Schematic diagram depicting preferentially oriented manifestations at the F-A and F-S interfaces of SDOSS/DLPC stabilized dispersions and DLPC stabilized dispersions treated with various ratios of CaCl ₂ /DLPC and PLA ₂ and adjusted to various pH.....	82
4.1.1. Schematic diagram illustrating reaction mechanisms responsible for formation of FMNTs.....	90
4.1.2. TEM images of nanotubes: (A) Step 1 — self-assembly of DC _{8,9} PC into nanotubes; (B) Step 2 — reactions of (NH ₄) ₂ Fe(SO ₄) ₂ and H ₂ O ₂ ; (C) Step 3 — thermal exposure to 550 °C for 0.5 hour.....	91
4.1.3. Raman spectra in the 3200-200 cm ⁻¹ region of nanotubes after Step 1 (A) and Step 2 (B), Optical image (C) and Raman image (D) of nanotubes after Step 2.....	92
4.1.4. Magnetic hysteresis loops of nanotubes after Steps 2 (A) and 3 (B) in Figure 4.1.1.....	93
4.2.1. Schematic diagram of FMNT formation: (A) Step 1 — self-assembly of DC _{8,9} PC into nanotubes; (B) Step 2 — addition of (NH ₄) ₂ Fe(SO ₄) ₂ ; (C) Step 3 — reactions of H ₂ O ₂ ; (D) Step 4 — thermal exposure to 550 °C for 0.5 hour. TEM images of nanotubes in each step are show in A'-D'.....	106

4.2.2. X-ray diffraction (XRD) of FMNTs (A) and Fe ₃ O ₄ (B).....	107
4.2.3. Selected area electron diffraction (SAD) of FMNTs.....	108
4.2.4. (A) High-resolution TEM image of FMNT surface and images (A') and (A'') demonstrate enlarged images of selected area where insert images a' and a'' show their diffraction patterns. a' reveals a diffraction pattern in 400 lattice spacing of 2.09 Å and 311 lattice spacing of 2.53 Å, while a'' represents the 111 lattice spacing of 4.85 Å, 220 lattice spacing of 2.95 Å, and 511 lattice spacing of 1.61 Å; (B) and (B') TEM images of FMNT wall structures; (C) and (C') schematic diagram of structures of FMNT, which consist of concentric multilayered carbon sheet and iron oxide layers. Gray squares represent iron oxide single crystals and black rings represent carbon layers.....	109
4.2.5. (A) TEM image of FMNT; (B) height contrast TEM image of selected area on FMNT; (C) energy dispersive X-ray spectroscopy (EDS) of element distribution along the arrow as draw in B, where trace a, b, c and d represent Fe, C, O, and S elements, respectively.....	111
4.2.6. Mössbauer spectra of FMNTs recorded at various temperatures: (A) 295 K; (B) 240 K; (C) 180 K; (D) 130 K; (E) 77 K; (F) 40 K; (G) 4.2 K.....	112
4.2.7. (A) Crystal lattice structure of magnetite: red-oxygen, blue-tetrahedral Fe ³⁺ and green-octahedral Fe ²⁺ /Fe ³⁺ ; (B) Polyhedral network of magnetite.....	113
4.2.8. Raman spectra in the 900-200 cm ⁻¹ region (A) and 2000-1000 cm ⁻¹ region (B): (a) FMNT; (b) FMNT after acid reactions; (c) PL powder annealed at 550 °C; (d) standard Fe ₃ O ₄	114
4.2.9. (A) Schematic diagram of measuring conductivity of a nanotube; (B) focused ion beam (FIB) image of FMNT; (B') Current-voltage (I-V) characteristics of FMNT; (C) FIB image of FMNT after acid treatment; (C') I-V characteristics of FMNT after acid treatment.....	115
4.2.10. A. Electrical resistivity and conductivity comparisons: (A) FMNT; (B) FMNT after HCl reactions; (C) standard magnetite; (D) multi-walled carbon nanotube (MWNT). B. Saturation magnetization (M _r) comparisons: (A) FMNT; (B) FMNT after HCl reactions (paramagnetic behaviors and the magnetization value recorded at the magnetic field of 10k Oe); (C) standard magnetite; (D) multi-walled carbon nanotube (MWNT).....	116
5.1. Schematic diagram of FMNT, which is a concentric magnetite nanotube separated by a carbon sheet concentric layer.....	129

- 5.2. TEM images of nanotubes prepared from: (A) 2 mg/mL PL in 85/15 methanol/water; (B) 5 mg/mL PL in 85/15 methanol/water; (C) 2 mg/mL PL in 70/30 ethanol/water. Each enlarged image is shown in A', B' and C'. Respective thickness of carbon layers are: 6 nm (A), 10 nm (B), and 50 nm (C).....130
- 5.3. Schematic diagram of nanotubes prepared from (A) 2 mg/mL PL in methanol/water; (B) 5 mg/mL PL in methanol/water; (C) 2 mg/mL PL in ethanol/water. Images A', B' and C' illustrate interactions between PL and solvents, respectively. A'' and C'' show the H-bonding interactions between PL and methanol as well as PL and ethanol.....131
- 5.4. TEM images of nanotubes prepared with various PL: Fe²⁺: H₂O₂ molar ratios of (A) 1:20:20; (B) 1:40:40; (C) 1:60:60; and (D) 1:80:80; Images A', B', C', and D' illustrate corresponding nanotubes after further annealing at 550 °C.....132
- 5.5. SEM images of FMNTs extruded through a 3 μm polycarbonate membrane without magnetic field (A) and (A'), and within magnetic field paralleling to the membrane (B) and (B').....133
- 5.6. TEM images of nanotubes prepared from (A) DC₇PC/DC_{8,9}PC, (B) DC₉PC/DC_{8,9}PC, and (C) DC_{8,9}PC.....134
- 5.7. Magnetic hysteresis loops of FMNTs prepared with various PL: Fe²⁺: H₂O₂ molar ratios of (A) 1:20:20; (B) 1:40:40; (C) 1:60:60; and (D) 1:80:80, which have increasing thickness of magnetite layers from 12 to 45 nm.....135
- 5.8. A. Schematic diagram of FMNT alternating alignment in polyester in the presence of magnetic field; B. SEM images of FMNT alternating alignment in polyester and enlarged images shown in B1 and B2; C. SEM image of FMNT in polyester without the presence of magnetic field.....136
- 6.1. Schematic diagram of surface reactions on FMNTs: Step 1, Ar microwave plasma reaction and hydrolysis of MA-modified FMNTs; Step 2, conversion of acid group and PEG reaction; Step 3, PEN reaction.....148
- 6.2. TEM images of (A) C₆₀; (A') PEN-PEG-MA-C₆₀; (B) MNCTs; (B') PEN-PEG-MA-MNCTs; (C) carbon fibers; (C') PEN-PEG-MA-carbon fibers; (D) FMNTs; (D') PEN-PEG-MA-FMNTs.....149
- 6.3. A. ATR FT-IR spectra of (A) C₆₀; (B) MA-C₆₀; (C) PEG-MA-C₆₀; (D) PEN-PEG-MA-C₆₀. B. ATR FT-IR spectra of (A) MWNTs; (B) MA-MWNTs; (C) PEG-MA-MWNTs; (D) PEN-PEG-MA-MWNTs. C. ATR FT-IR spectra of (A) carbon fibers; (B) MA-carbon fibers; (C) PEG-MA-carbon fibers; (D) PEN-PEG-MA-carbon fibers. D. ATR FT-IR spectra of (A) FMNTs; (B) MA-FMNTs; (C) PEG-MA-FMNTs; (D) PEN-PEG-MA-FMNTs.....150

6.4. The volume concentration for C ₆₀ , MWNT, carbon fiber and FMNTs for each step.....	151
6.5. Photographs of agar plates containing (A) C ₆₀ ; (A') PEN-PEG-MA-C ₆₀ ; (B) MWNTs; (B') PEN-PEG-MA-MWNTs; (C) carbon fibers; (C') PEN-PEG-MA-carbon fibers; (D) FMNTs; and (D') PEN-PEG-MA-FMNTs in <i>Staphylococcus aureus</i> cultures.....	152
6.6. Cytotoxicity analysis of specimens: (A) C ₆₀ ; (A') PEN-PEG-MA-C ₆₀ ; (B) MNCTs; (B') PEN-PEG-MA-MNCTs; (C) carbon fibers; (C') PEN-PEG-MA-carbon fibers; (D) FMNTs; (D') PEN-PEG-MA-FMNTs; Optical images of cell growth on the specimens: (d) FMNTs; (d') PEN-PEG-MA-FMNTs.....	153

LIST OF TABLES

Table

- 2.1. Experimental and calculated IR bands obtained from ATR FT-IR measurements and ab initio calculations using Models A and D.....53

- 3.1. Dichroic Ratios of Selected IR Bands^a of SDOSS/DLPC stabilized p-MMA/nBA colloidal dispersions. ^a $R = A_{\parallel} / A_{\perp}$, where A_{\parallel} and A_{\perp} are band areas for parallel (TE) and perpendicular (TM) polarizations. R values were obtained by ratioing the baseline corrected IR bands of interest. For each band, the same wavenumber range was used to determine the band area for TE and TM polarizations.....72

- 3.2. Dichroic Ratios of Selected IR Bands^b of DLPC stabilized p-MMA/nBA colloidal dispersions. ^b $R = A_{\parallel} / A_{\perp}$, where A_{\parallel} and A_{\perp} are band areas for parallel (TE) and perpendicular (TM) polarizations. R values were obtained by ratioing the baseline corrected IR bands of interest. For each band, the same wavenumber range was used to determine the band area for TE and TM polarizations.....73

INTRODUCTION

This dissertation is concerned with new advances in assembly and molecular recognition using phospholipids (PLs) and consists of two parts: Part (1) (Chapters II-III) outlines structural features of PLs responsible for recognition of synthetic copolymers, and Part (2) (Chapters IV-VI) focuses on design, synthesis and analysis of magnetic nanotubes obtained from PLs templates.

Chapter I focuses on a review of the recent advances of molecular recognition, PL self-assembly, and magnetic nanotubes as well as elucidates the promising opportunities of bioactive PLs to create different shapes, exhibiting stimuli-responsive and specific recognizing ability. Due to PL amphiphilic nature, versatile self-assembled morphologies can be achieved ranging from micelles, liposomes, bilayers, to nanotubes. The incorporation of biocompatible PL as stabilizing agents into colloidal dispersions offers a potential opportunity to prepare novel biomaterials, which may exhibit stimuli-responsive features and selective recognition.

Chapter II investigates the molecular recognition of surface localized ionic clusters (SLICs) formation as well as their structural features formed on polymer surfaces. Poly(methyl methacrylate/*n*-butyl acrylate) (p-MMA/*n*BA) colloidal particles that were stabilized by 1,2-dilauroyl-*sn*-glycero-3-phosphocholine (DLPC) PLs were synthesized. Upon particle coalescence, PL stratification resulted in the formation of surface localized ionic clusters (SLICs). These entities were capable of recognizing MMA/*n*BA monomer interfaces along the p-MMA/*n*BA copolymer backbone and form crystalline SLICs at the monomer interface. Utilizing attenuated total reflectance Fourier transform infrared (ATR FT-IR) spectroscopy and selected area electron diffraction (SAD) combined with ab

initio calculations, we determined the nature of the interactions between anionic phosphate groups, cationic quaternary ammonium groups of the phospholipid, and carbonyl groups of the neighboring MMA and nBA units of p-MMA/nBA copolymer, where the two neighboring MMA and nBA units along the polymer backbone provided conducive environments to signal and attract amphiphilic groups of DLPC, thus initiating SLIC formation.

Chapter III describes synergistic stimuli-responsive behaviors of the p-MMA/nBA colloidal dispersions in the presence of sodium dioctyl sulfosuccinate (SDOSS) and 1,2-dilauroyl-*sn*-glycero-3-phosphocholine (DLPC). Stimuli-responsive behaviors such as the combined effects of ionic strength, enzyme, and pH of these colloidal dispersions were investigated on the mobility of dispersion stabilizing agents within p-MMA/nBA copolymer matrixes during and after coalescence. ATR FT-IR spectroscopy of p-MMA/nBA colloidal dispersions revealed the formation and the preferential orientation of SLICs at the film-air (F-A) or film-substrate (F-S) interfaces in response to the combined stimulus effects. Using this approach it is possible to control surface morphologies of coalesced films.

Chapter IV addresses the synthesis and structural features of concentric ferromagnetic iron oxide-carbon-iron oxide nanotubes (FMNTs) using biologically active 1,2-bis(10,12-tricosadiynoyl)-*sn*-glycero-3-phosphocholine (DC_{8,9}PC) nanotube-forming PL as templates, which consists of two parts. While Part I focuses on the synthesis of FMNTs, Part II analyzes the structural and morphological features. In Part I, this was accomplished by polymerization of DC_{8,9}PC in the presence of Fe²⁺/H₂O₂ redox agents which leads to the formation of amorphous iron oxide concentric nanotubes. Further

exposure to 550 °C resulted in the partial removal and crosslinking of the organic phase and conversion of amorphous iron oxide to concentric iron oxide-carbon-iron oxide nanotubes. FMNTs exhibited the remanent magnetization (M_r) of 4.62 emu/g, the saturation magnetization (M_s) of 46.12 emu/g, the squareness (M_r/M_s) of 0.1002, and the coercivity (H_c) of 51.35 Oe. In Part II, by combining the analysis of x-ray diffraction (XRD), SAD, high-resolution transmission electron microscopy (HRTEM), and Mössbauer spectroscopy, concentric magnetite (Fe_3O_4)/carbon/magnetite nanotubes were revealed, where the carbon layer was sandwiched between two magnetite layers as well as magnetite was present inside the carbon interlayer. These nanotubes can be utilized not only in devices with tunable ferromagnetic properties, but also as nano-conductors. Electrical resistivity of FMNTs and FMNTs after the removal of iron oxide layers by acid reactions are 3.3×10^{-2} and $5.06 \times 10^{-4} \Omega\cdot\text{m}$, respectively, indicating that these properties can be also tailored for specific applications.

Chapter V reports the synthetic approaches producing controllable and uniform diameter, wall thickness, and length of FMNTs. While the thicknesses of the carbon layers can be controlled by the chemistry of PL templates as well as their concentration and solvent environments, variable wall thicknesses of magnetite layers can be achieved by changing concentration levels of the reactive species. Furthermore, in order to obtain desirable lengths of FMNTs, we developed extrusion through a porous polycarbonate membrane, which combined with the diameter changes of nanotubes achieved by incorporating saturated phospholipid spacers into PL templates, thus resulting in the aspect ratio changes ranging from 10 to 80. Consequently, a spectrum of magnetic properties, such as saturation magnetizations increase (from 40 to 79 emu/g) as well as

the geometry parameter β and parallel magnetization states. In addition, by alternating magnetic field direction, the preparation of FMNTs/polyester nanocomposites containing alternating alignment of FMNTs was demonstrated.

Chapter VI illustrates the development of surface modifications of C_{60} , multi-walled carbon nanotubes (MWNTs), FMNTs, and carbon fibers that resulted in inhibition of gram positive bacteria and cytotoxicity. This was accomplished by the sequence of reactions, which involved microwave plasma reactions of maleic anhydride (MA) and subsequent hydrolysis leading to the formation of carboxylic acid groups, conversion of carboxylic acid to carboxylic chloride groups, followed by reactions of a polyethylene glycol (PEG) spacer, and the subsequent chemical attachment of penicillin (PEN). Each step of surface reactions was analyzed spectroscopically, and the PEN reaction sequences revealed the presence of ester linkages due to the reactions between PEN and PEG functionalities. Furthermore, introduction of PEG serving as a molecular spacer allowed PEN molecules desirable mobility, thus making it surface effective against formation of microbial films. Antimicrobial tests revealed highly effective anti-bacterial activity toward gram-positive *Staphylococcus aureus* bacteria, and cytotoxicity experiments illustrated no toxicity against mouse embryonic stem cells.

CHAPTER I

MOLECULAR RECOGNITION AND PHOSPHOLIPID SELF-ASSEMBLY

Introduction

Progress in nanotechnologies has brought numerous new developments, challenges, and opportunities. Several notable developments are single-walled carbon nanotubes (SWNT),¹ molecular self-assemblies,² self-healing polymers,³ molecular recognition,⁴ biosensors.⁵ These new developments also created a spectrum of challenges among which is the ability of incorporating synthetic and natural monomers or macromonomers to generate smart nanomaterials with sustainable biocompatibility that exhibit stimuli-responsiveness as well as a specific recognition. Among a variety of bioactive species phospholipids (PLs) are of particular interest as these entities are essential components in cell membranes, capable of forming bilayers, micelles, liposomes and tubules. Due to PL amphiphilic nature, versatile self-assembled morphologies can be achieved ranging from micelles, liposomes, bilayers to nanotubes. The incorporation of biocompatible PL as stabilizing agents into colloidal dispersions offers a potential opportunity to prepare novel biomaterials, which may exhibit stimuli-responsive features and selective recognitions. Furthermore, due to their unique structural and morphological features, PL may serve as templates for developing nanomaterials with tailored properties.

Molecular Recognition

In nature, biological molecules such as proteins and DNA are able to recognize each other as well as numerous other molecular sequences through specific interactions. During this process, formulation of complex entities facilitating the various necessary

functions to maintain living activities occurs, and examples of these interactions are avidin-biotin, antigen-antibody, DNA-protein, sugar-lectin, and others.⁶ The primary driving forces responsible for selective recognitions are through non-covalent interactions, including H-bonding, electrostatic forces, hydrophobic interactions, and metal-ligand coordinations.⁷ One of the notable and well-studied examples of these interactions is biotin and avidin. Biotin molecules using carboxylic acid groups can form selective binding with the lysine and tryptophan of avidin, a tetrameric protein containing four identical subunits, that plays an important role in gluconeogenesis.⁸

Aside from molecular recognitions in bimolecular systems, synthetic macromolecules have been shown to bind target molecules and mimic biological recognitions, which are potentially utilized in therapeutic and diagnostic applications. This field is quite open and there are many opportunities for new advances to further understand a variety of recognitions at a molecular level. In order to achieve specific recognitions, often natural recognitions of specific proteins were utilized to immobilize them to various polymer platforms, such as polymer brushes,⁹⁻¹² colloidal nanoparticles,^{12,13} and stimuli-responsive polymer surfaces.^{14,15} Resulting from a high density of reactive groups as well as good swellability, polyacrylic acid brushes were grafted onto a gold substrate and further reactions introduced a nitrilotriacetic acid ligand in the presence of Cu^{2+} , which showed a good reversible binding capacity with proteins such as lysozyme, myoglobin and bovin serum albumine.⁹ Polymer nanoparticles with a polystyrene core and a glucosyloxyethyl methacrylate (GEMA) oligomer shell were also prepared, which exhibited good binding ability with a concanavalin A lectin.¹³ Stimuli-responsive polymers, such as poly(N-isopropyl acrylamide) (PNIPAAm) by chemically

bonded with Streptavidin, were also utilized for responsive molecular recognition.¹⁴ Due to stimuli-responsive features of PNIPAAm, this polymer has shown reversible binding with biotin below LCST of 32 °C, whereas above LCST no binding was observed as a result of polymer collapse leading to block binding sites.¹⁴ Using the concept of folded or expanded conformations of proteins, multi-type monomers, such as anionic acrylic acid, cationic methacryl-amido-propyl-trimethyl-ammonium chloride (MAPTAC), and thermo-responsive NIPAAm were copolymerized and formed heterogels, where two phases were obtained: swollen and collapsed phases. At the collapsed state, such functional anionic or cationic groups are close to each others, thus forming a receptor-like recognition site for the specific molecular detection.¹⁶ For example, p-MAPTAC/NIPAAm heterogels were able to reversibly bind negatively charged pyranine molecules through multiple ionic interactions in collapsed state at 55 °C and released pyranine in swollen phase at 25 °C.¹⁷ Similar recognitions were also applied to p-NIPAAm/acrylic acid polymeric gels, which exhibited the reorganizing ability of norephedrine and adrenaline.¹⁸

Another approach to facilitate the recognition ability is designing molecular cavities where other molecular entities can fit and selectively bind. Molecular imprinting polymer (MIP) technique is one of the commonly accepted methods for molecular recognition, which enables creating cavities in the polymer network.¹⁹⁻²² This approach is based on prepolymerization and crosslinking of functional monomers in the presence of template molecules which interact with a monomer through covalent or non-covalent bonds, or metal-ligand coordinations. Upon removing the template molecules using solvent extraction, three-dimensional porous polymer networks are formed, which

contain cavities which are able to recognize specific template molecules. Hydrogels are cross-linked and hydrophilic polymeric networks. As a result of significant water content, hydrogels exhibit good biocompatibility as well as similar flexibility to natural tissues. Such hydrogels as polyacrylamide,²¹ polyacrylic acid,²² and polymethacrylic acid¹⁹ were mostly investigated to be utilized as the MIP networks.

Because acrylic acid or acrylic amide functional groups are able to interact with template molecules through H-bonding in non-polar solvents or ionic interactions in aqueous solutions, interpenetrating polymer network hydrogels containing chitosan and polyacrylamide were prepared, which showed a significant adsorption capacity for hemoglobin.²¹ The advantage of introducing chitosan into the polymeric network is its higher affinity to proteins due to the presence of a significant number of amino and hydroxyl groups in chitosan. In contrast with MIP without chitosan or nonimprinted hydrogel, MIP containing chitosan exhibit much higher protein adsorption.²¹ Another notable example is copolymerization of methacrylic acid and trimethylolpropane trimethacrylate to form MIPs in the presence of magnetic particles.²² Due to magnetic properties, particles can be easily separated and manipulated as well as localized to designated sites by external magnetic field. This magnetic MIP exhibits good specific recognition and further controlled release of aspirin.²²

Although synthetic polymers rarely have identical structures to multi-functional proteins, heteropolymers randomly synthesized using multi-monomers were found to offer recognition ability, which were contributed to a portion of polymers with the same distribution of functional groups as the target molecule, thus leading to the strong binding between polymers and target and therefore recognition ability.²³⁻²⁸ Dextran polymers

were randomly modified with sulphonate, carboxylate, amino acid sulphamide and amide groups, and they were found to interact with the complement component 3b (C3b) protein and subsequently inhibit the activation of the complement system which is a crucial process in the immune response.^{24,25} Similar random heteropolymers containing biomimetic functional groups were also prepared to recognize insulin secretion,^{26,27} or fibronectin protein.²⁸

Although numerous experiments are conducted every year to determine specificity of recognition in biological systems, complexity of interactions and a lack of probes to establish molecular events leading to these interactions often prohibit detailed molecular understanding. Thus, how to understand the mechanisms of molecular recognition on a molecular level continues to be a challenge. However, using computational simulations combined with experimental evidence may play a significant role in elucidating the principles of molecular recognitions. Typical simulation approaches includes Monte Carlo approach, molecular dynamics, density functional theory (DFT), ab initio calculations, and molecular mechanics.²⁹ The recognition of DNA and protein with phospholipids has been studied,³⁰⁻³⁴ which depends on the intermolecular interactions resulting from their structural features. In an aqueous salt solution, resulting from the molecular electrostatic and elastic interactions, cationic PL and DNA were found to form various relatively stable complexes including flat-bilayer, honeycomb, and cylindrical structures.^{30,31} A phase diagram was further proposed to elucidate PL and DNA interactions.³² Molecular mechanics approaches were also employed to reveal the presence of a cationic bridge in the complexes and emphasize the effect of primary structure of nucleic acid on the intramolecular interactions.³³ The

interactions between transmembrane proteins and a lipid bilayer were examined using molecular dynamics simulation, and the results are shown in Figure 1.1.³⁴ As seen, the lysine groups of protein form H-bondings to phosphate and ester oxygens of PL, and there are also H-bonding interactions between the tryptophan groups of protein and ester oxygens of PL.³⁴ Recently, molecular simulation method have been utilized to study the mechanisms of molecular recognition by MIPs.³⁵⁻³⁷ The all-atom kinetic gelation model where the position and interactions of all atoms were traced was employed to study the polymer formation as well as recognizing and binding ability.³⁵ Several MIPs for recognizing biotin were prepared and using the molecular mechanism method, their binding and dissociation ability with biotin were compared, which revealed that p-methacrylic acid had a highest binding energy and sufficient biotin dissociation constants were obtained.³⁶ The effect of solvents on the molecular recognition capability of MIPs using DFT theory and showed that maximum selectivity was obtained when chloroform were utilized in the MIP synthesis, which is in good agreement with experimental results.³⁷

Although these examples demonstrate significant interest in this field, there are many advances to be made. As the above examples demonstrate, the majority of studies are concerned with biological systems, where specific recognitions between individual entities were established using a sequence of empirical methods. Recognition of synthetic molecules and naturally occurring species remain uncharted areas. One of the challenges will be how to mimic biologically active species using synthetic materials at molecular levels and in view of these considerations and limited literature data, PLs are of particular

interest due to their unique structural features, biocompatibility, and the ability to self-assemble.

Phospholipid Self-Assembly

Phospholipids are the principal components of biomebranes and the matrix of the biological membrane is a lipid bilayer composed of phospholipids, which serves as a permeability barrier for essential molecular diffusion. As shown in Figure 1.2, phospholipids are derived from glycerol-3-phosphate esterified at its C1 and C2 positions to fatty acid chains and the phosphoryl group to a head moiety. These amphiphatic species contain hydrophilic polar head groups and hydrophobic long hydrocarbon chains which are capable of self-assembling in an aqueous phase. When such amphiphatic molecules are mixed with water, they spontaneously form various aggregates depending on the chemical makeup, concentration levels, ionic strength of the solution, and preparation methods. Figure 1.3 schematically illustrates possible aggregation forms which are attributed to hydrophilic and hydrophobic groups.³⁸ When the cross-sectional area of the head group is larger than that of the tails, such as sodium dioctylsulfosuccinate (SDOSS), typical micelle structures are formed as shown in Figure 1.3, A. However, when the cross-sectional areas of the head group and the tails are similar, such as in 1,2-dilauroyl-*sn*-glycero-3-phosphocholine (DLPC) phospholipid, bilayer formation is favored as illustrated in Figure 1.3, B. Furthermore, hydrophobic tails at bilayer edges are in contact with water transiently and the bilayer sheet is not quite stable, thus capable of forming a hollow sphere, or liposome shown in Figure 1.3, C, which is much more stable in water.³⁸

Due to their amphiphilic nature leading to versatile aggregation forms, PLs were recently successfully utilized as surfactants and templates in emulsion polymerization to stabilize colloidal particles and control particle morphology by altering interfacial tensions resulting in different shapes. In emulsion polymerization^{39,40} monomers are polymerized using a free-radical initiator in an aqueous solution of a surfactant to form colloidal particles which are dispersed in an aqueous medium. The main ingredients of the emulsion polymerization include monomers, surfactants, initiators, and water. The schematic diagram of the emulsion process is shown in Figure 1.4. When the surfactant concentration surpasses its critical micelle concentration (CMC), the excess surfactants aggregate to form micelles. As monomer molecules diffuse to micelles through the aqueous phase from the monomer droplets, in the presence of initiators which may cleave thermally or photochemically, polymerization begins. Monomers continue to diffuse to active particles until monomer droplets are exhausted and polymerization reactions stop until the remaining monomers are consumed.³⁹ In recent years, composite colloidal particles with tailored physical properties and versatile morphologies have been prepared through consecutive emulsion polymerization processes using different monomers, where typically the second-step monomer is polymerized in the presence of the seed particles prepared in a separate process. Although a number of variables during seed polymerization are believed to result in various particle morphologies³⁹, including core-shell,⁴¹ inverted core-shell,^{42,43} hemispherical,^{43,44} sandwich structures.⁴⁵ Recently, pentafluorostyrene (PFS) was copolymerized with methyl methacrylate (MMA) and n-butyl acrylate (nBA) in a two-step emulsion polymerization process which generated acorn-shaped stable colloidal particles, where one hemisphere of the nanoparticles

contained p-PFS phase and the other hemisphere consisted of p-MMA/nBA phase.⁴⁴

Figure 1.5, A and B illustrate a TEM image of these particles and a photograph of acorns, respectively. Upon film coalescence, these acorn-shaped particles exhibited self-assembly ability depending on the surface energy of a substrate, where the p-PFS phase localized itself near the film-air (F-A) interface for a high surface tension substrate and in contrast the p-PFS phase dominated the film-substrate (F-S) interface for a low surface energy substrate.⁴⁴

How to control and predict particle morphologies becomes a crucial issue because minute chemical-physical alterations may lead to drastic property changes. Surfactants play a significant role in stabilizing particles and controlling particle morphology by altering interfacial tensions. For traditional surfactants, such as sodium dioctylsulfosuccinate (SDOSS) or sodium dodecyl sulfate (SDS), micelles to stabilize the spherical colloidal dispersions are formed. However, by changing the surfactant from sodium lauryl sulfate to natural pectin, particle morphologies were altered from particle/oil droplets to completely encapsulated oil droplets (core-shell).³⁹

Recently, phospholipids such as 1,2-bis(10,12-tricosadiynoyl)-*sn*-Glycero-3-Phosphocholine (DC_{8,9}PC),^{46,47} DLPC,⁴⁸ 1-myristoyl-2-hydroxy-*sn*-glycero-phosphocholine (MHPC)⁴⁹ and hydrogenated soybean phosphatidylcholine (HSPC)⁵⁰ have been employed as cosurfactants in the emulsion polymerization of p-MMA/nBA copolymer, which forms non-spherical colloidal dispersions as well as contains stimuli-responsive features. For example, cocklebur-shape particles were obtained to polymerize MMA and n-BA in the presence of SDOSS and DCPC stabilizing species using a nano-extruder, which is illustrated in Figure 1.6.⁴⁶ As seen, upon extrusion, p-MMA/nBA

colloidal particles containing tubules pointing outward were prepared resulting from DC_{8,9}PC phospholipids present at the particles surfaces. Using traditional emulsion polymerization, MMA and n-BA were also polymerized into stable colloidal particles in the presence of SDOSS and liposome forming DLPC phospholipids,⁴⁸ which showed that hollow colloidal particles were obtained for DLPC stabilized p-MMA/nBA and stable monomodal spherical particles for DLPC and SDOSS stabilized p-MMA/nBA. The presence of DLPC along with SDOSS exhibited stimuli-responsive behaviors during film formation and these stabilizing components can be driven to the film-air (F-A) or film-substrate (F-S) interface in response to thermal, ionic, pH, and enzymatic stimuli, which is depicted in Figure 1.7. As seen, in response to these stimuli, migration direction (labeled) changes and during film formation particles containing SDOSS/DLPC release stabilizing species to the F-S interface at elevated temperature and low ionic strength, or to the F-A interface, at higher pH environments and enzymatic degradation of DLPC.⁴⁸ In contrast, when HSPC acts as cosurfactant with SDOSS in the p-MMA/nBA colloidal dispersions,⁵⁰ formation of bimodal particle distribution was observed, which was attributed to dissimilar hydrophobicity and compatibility of HSPC and SDOSS. Upon coalescence, PLs were released at F-A interface and their preferential orientation to the F-A interface were varied as changing ionic strength.

PL can also serve as facilitators of non-spherical particle synthesis. Using DLPC copolymerization of heptadecafluorodecyl methacrylate (FMA) with MMA/nBA was accomplished.^{51,52} Although several efforts⁵³⁻⁵⁶ have been made to prepare fluorinated colloidal dispersions, relatively low solids and fluorine contents (8.5% w/w) were obtained resulting from their limited solubility in an aqueous phase. However, the

incorporation of DLPC into the synthesis of fluorinated monomers led to stable non-spherical particles with up to 15% w/w FMA contents, which is attributed to the lower CMC of DLPC,⁵¹ and the ability to facilitate monomer transport usually not achievable using traditional surfactants. Morphologies of these particles were able to be varied depending on MMA/nBA ratios, and spherical particles were obtained for higher MMA content, whereas non-spherical morphologies were observed for higher nBA content, which is resulting from monomer starved conditions and the reactivity ratio differences, thus forcing copolymerization of FMNA on the p-MMA/nBA particle surfaces. Upon particle coalescence, such films exhibited ultralow static and kinetic coefficients of frictions due to FMA phase stratification during film formation.⁵²

Aside from the versatile self-assemble forms of PL, DC_{8,9}PC is a unique PL which can form hollow cylinders, namely “tubules.” Previous studies^{57,58} showed that DC_{8,9}PC are able to form liposomes in an ethanol/water solution above its hydrocarbon chain melting temperature (T_m), which forms a disordered high-temperature L_α phase, and these liposomes can be converted to stable hollow tubules at lower temperatures, corresponding to an ordered low-temperature L_β phase. The dimensions of these tubules vary from 0.4 μm to 1 μm in diameter and tens to several hundreds of micrometers in length, with walls that vary from two to ten bilayers in thickness, usually 10-50 nm. Two approaches of tubule preparation have been widely utilized: the liposome process which forms phospholipid liposomes in ethanol/water solution and then cools down the solution, and the precipitation process,⁵⁹ where water is added into an ethanol/phospholipid solution and tubules are precipitated. The tubules prepared from the liposome process often contain one or more trapped liposomes that can immobilize aqueous content within

the tubules but prevent the tubule lumen from being a true open cylinder, while the tubules from precipitation process have no trapped liposomes so that they are true open hollow cylinders.⁵⁹ Besides multilayer tubules, other morphologies such as unilamellar cylinders,⁶⁰ coaxially nested cylinders,⁶⁰ cones⁶¹ are found, depending on the solvent.

Formation of PL different shape assemblies in water has been of significant interest, in particular tubule formation. There are three general concepts that attempted to explain tubule formations: electrostatic interactions, proposed by de Gennes;⁶² elasticity of orientational order, proposed by Lubensky and Prost,⁶³ and the chirality theory, proposed by Schnur.⁶⁴ While the first two concepts provided rather general explanation regarding inter-molecular interactions, they did not account for experimental observations such as specificity of orientations of individual molecules. Currently, the chirality theory is well accepted to elucidate how diacetylene phospholipids form tubules. Due to chirality, PL molecules are unable to pack parallel together, so that each molecule packs at certain favored angle with respect to the other nearest molecule and the twist from a molecule to a molecule leads the bilayer to twist out of the plane, thus forming a tubule. Figure 1.8⁶⁵ illustrates the formation of tubular structure resulting from the chirality of individual molecules and as shown above T_m , PLs preferentially form liposomes, and upon cooling below T_m , there are two possible paths to form tubules. The first path, as shown in Figure 1.8a, results from a decrease of the helical pitch of the ribbon while maintaining a constant tape width. The second path as shown in Figure 1.8b involves an increase of the tape width which keeps a constant helical pitch, which is more common based on the literature.

Lipid tubules are of significant interest, because they may have many potential applications ranging from slow release and nano-fluidic devices to delivery systems, or molecular traps for self-healing applications, electronic devices, and many others. Since they are fragile and unstable at elevated temperatures, lipid tubules serve as templates and due to ionic phosphocholine groups they are able to be coated with metal,⁶⁶⁻⁷³ silica,⁷⁴ clay,⁷⁵ oppositely charged polymers and nanoparticles^{76,77} or make polypyrrole strands.⁷⁸ For example, nickel were coated onto DC_{8,9}PC tubules using electroless deposition, followed by embedding in epoxy resin and such nickel tubules/epoxy composite were demonstrated to the fabrication of a cathode for vacuum field emission.⁷⁹ In addition, resulting from their hollow cylinder structures thus offering encapsulation and controlled release ability through diffusion, copper coated DC_{8,9}PC tubules were mixed with antifouling agents in epoxy matrix and such coating were applied to surfaces exposed to the marine environments, which showed good antifouling properties and the slow-release of antifouling agents for many months.⁷³

In summary, the presence of hydrophilic head groups and hydrophobic tails facilitates the formation of the unique amphiphilic structural features of PL, which provide the ability to form diverse self-assemble shapes. Thus, there are numerous opportunities in creating shapes by serving as stabilizing agents for colloidal dispersions as well as templating of depositing other species, which may open new avenues in development of nanomaterials with various shapes. One potential aspect is to use PLs as templates to prepare magnetic nanotubes, and the following section will introduce the preparation and recent advance of magnetic nanotubes.

Magnetic Nanotubes

Magnetic nanomaterials are of particular interest due to their potential applications. Of particular interest are geometrical parameters because they will dictate magnetic properties.^{80,81} One of the recent examples of utilization of superparamagnetic nanoparticles was their ability to repair mechanically damaged polymer matrix upon exposure to the oscillating magnetic field.⁸² Although many attempts have been made to explore the use of magnetic nanoparticles in many biomedical applications, the control of the sizes and surface composition remain to be still challenging.^{83,84} One of the difficulties is the formation of aggregates as well as limited controllable surface modifications. In spite of favorable size in the range of a few nanometers allowing penetration of biological cells in many applications, magnetic nanotubes are indispensable. Aside from the ability to modify inner and outer surfaces, diameter, wall thickness, and lengths are of particular interest in many materials applications ranging from drug delivery systems to biosensing devices.

Among several methods of synthesis of magnetic nanotubes probably the most common one was to use templates of other materials. For example, anodized aluminum oxide (AAO) templates were utilized to prepare magnetite (Fe_3O_4)/silica,^{85,86} cobalt/polystyrene,⁸⁷ Ni,⁸⁸ Co,⁸⁸ FePt, Fe_3O_4 ,^{89,90} NiFe_2O_4 ,⁹¹ and Fe_3O_4 / polypyrrole nanotubes.⁹² In addition, Fe_3O_4 /polymer⁹³ and Fe_3O_4 /polypeptide nanotubes⁹⁴ were prepared using the layer-by-layer assembly of polyelectrolyte or polypeptide and Fe_3O_4 in the presence of the porous polycarbonate templates. Other template methods involve in the pulsed laser deposition of Fe_3O_4 onto MgO nanowires,⁹⁵ mineralization of tobacco mosaic virus (TMV) template,⁹⁶ bacterial Fe_3O_4 nanocrystal onto peptide nanotubes,⁹⁷

and α -Fe₂O₃ nanotube templates to prepare Fe₃O₄ and γ -Fe₂O₃ nanotubes by hydrothermal methods.⁹⁸ Biologically active DC_{8,9}PC PL nanotubes⁹⁹ were also utilized as a template to form ferromagnetic iron oxide/carbon nanotubes (FMNTs).¹⁰⁰

As shape contributes to magnetic properties,^{80,81} magnetic nanotubes resulting from its unique hollow cylinder structures provide an opportunity for diversified applications. The equilibrium magnetization states of magnetic nanotubes have been identified as a ferromagnetic state with all the magnetic moments are parallel to the tube axis, and a flux-closure vortex state. To determine which configuration is dominant depends on geometrical factors¹⁰¹⁻¹⁰³ such as the diameters of the nanotubes and their aspect ratios as well as the structure features.^{102,104} It was found that the ferromagnetic state exists in the middle part of nanotubes with enough length, while the end of nanotubes exhibits a vortex state.^{105,106} Preferential parallel magnetic orientation is observed in composite cobalt/polystyrene nanotubes with small diameters and isotropic magnetic features for larger diameters.⁸⁷

Due to continuous demand of biocompatible synthetic nanomaterials utilized in biological systems, understanding of interactions of nanomaterials with biological systems is also very important, and particularly the influence of nano-size and shapes on cell cytotoxicity are of significance. Recent studies that utilized carbon nanotubes and fullerenes indicated that interactions of these species with living cells or other biosystems are complex and not well understood. Although cytotoxicity of carbon nanotubes and fullerenes have been attributed to size,^{107,108} shape,^{109,110} surface functionalizations,^{111,112} and even the choice of a test method,^{113,114} further detailed studies are needed to resolve these issues. There is a common agreement that these materials, however, exhibit

antimicrobial properties.^{108,115,116} For example, highly purified single wall carbon nanotubes showed antimicrobial activities against *Escherichia coli* (E. coli) and their cytotoxicity resulted from a direct contact with a bacterial cell membrane, causing severe cell membrane damage.¹¹⁵ Ideally, one would like to control cytotoxicity while maintaining antimicrobial functions and thus controlling these properties of nanomaterials are of particular interest, which may open up many potential applications in various fields of medicine. Although magnetic particles and nanotubes have been utilized in biological applications, their cytotoxicity and biocompatibility are still under investigation, which may be influenced by impurities or preparation methods.

Incorporation of synthetic and natural objects to generate smart devices with sustainable biocompatibility and multifunctions remains to be a challenge. Unfortunately, the majority of synthetic materials in contact with bio-systems become problems due to either microbial growth or cytotoxicity. One approach to alleviate and control interactions of bioorganisms on surfaces while maintaining useful bulk characteristics is to modify their surfaces. In order to overcome the compatible limitation of magnetic nanotubes in biological applications, surface modification methods were utilized. Fe₃O₄/silica nanotubes were differentially functionalized on their outer or inner surfaces by physical absorption,⁸⁵ whereby upon inner surface modification by octadecyltriethoxysilane these nanotubes exhibited hydrophobic inner surface and hydrophilic outer surface, as a result, they were easily dispersed in water as well as extracted and separated hydrophobic dye molecules through hydrophobic interactions. Alternatively, human Immunoglobulin G (IgG) and poly(ethylene glycol) (PEG) silane were also functionalized onto their inner and outer surface, which demonstrated a magnetic bioseparation of anti-human IgG

through antigen-antibody interactions. In addition, magnetic nanotubes upon inner surface modification with amino-silane were filled with several drug molecules in order to study the drug release and influence of hydrogen-bonding interactions, which indicated that the drug containing carboxylic acid group exhibited a slow releasing rate through strong hydrogen-bonding.⁸⁵ Magnetic Fe₃O₄ nanotubes containing polypeptide were able to adsorb plasmid DNA through electrostatic interactions, which demonstrated their potential applications in gene transfer areas.⁹⁴ Superparamagnetic Fe₃O₄/polymer nanotubes capable of adsorbing poly(ethylene oxide)-b-poly(methacrylic acid) block copolymers to enhance colloidal stability were also able to adsorb and further release low molecular weight anionic dye and drug molecules.⁹³

Compared to physisorption modification methods, the advantages of covalently bonded species to the surfaces provide more stability and uniformity of surface entities. Since covalent bonding to surfaces using grafting-to^{117,118} and grafting-from^{117,119-121} reactions offer significantly greater control over the surface chemistry as well as surface morphologies, various synthetic paths were utilized. However, key components for successful covalent attachments of other species are to create a reactive surface group as well as a molecular spacer. While a surface reactive group facilitates an anchor for further reactions, the presence of a spacer provides mobility to bioactive species attached to the end of the spacer. For example, antibiotics such as penicillin (PEN)^{119,122} and ampicillin (AM)¹²³ which prevent bacteria protein synthesis, were successfully chemically attached to expanded poly(tetrafluoroethylene) (ePTFE) surfaces using plasma reactions and grafting of poly(ethylene glycol) (PEG) spacer through carboxylic acid groups as well as the attachment of bioactive molecules, which are illustrated in

Figure 1. 9. As seen, the first step is the attachment of an anchor molecule through the reaction of maleic anhydride to form acid groups using microwave plasma reactions, followed by reactions of a PEG spacer to provide mobility to the active antibiotic molecule attached to the other end of the spacer. These studies showed high effectiveness against both gram positive and negative bacteria. Such surface reactions are appealing because they may be utilized in the surface modifications of nano-objects such as carbon nanotubes, fullerene, and magnetic nanotubes, which may open a new avenue for creation of biocompatible nanomaterials.

In summary, as new developments in nanotechnologies progress, the formation of nanomaterials with diverse shapes with sustainable and biocompatible properties continues to be a challenge. The incorporation of bioactive PLs into nanomaterials provides another promising opportunity because due to their unique amphiphilic nature, PLs are able to form versatile shapes, thus offering unexploited avenues for creating new materials with various shapes which may exhibit stimuli-responsive features and the ability of recognizing other species.

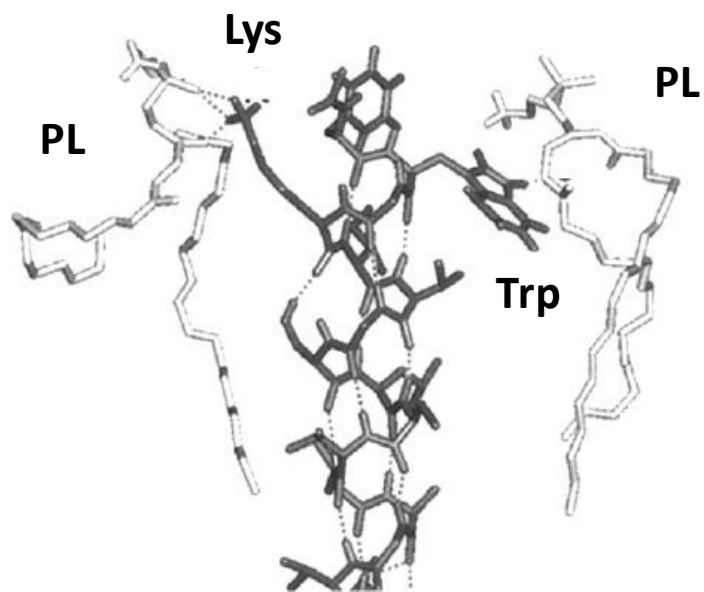


Figure 1.1. Interactions between PL and a transmembrane α -helix in a lipid bilayer.³⁴

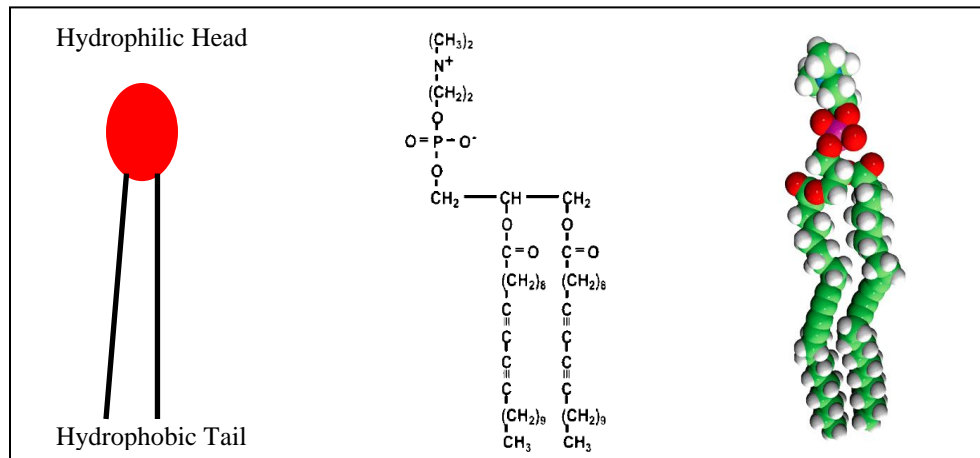


Figure 1.2. Structure of a phospholipid.

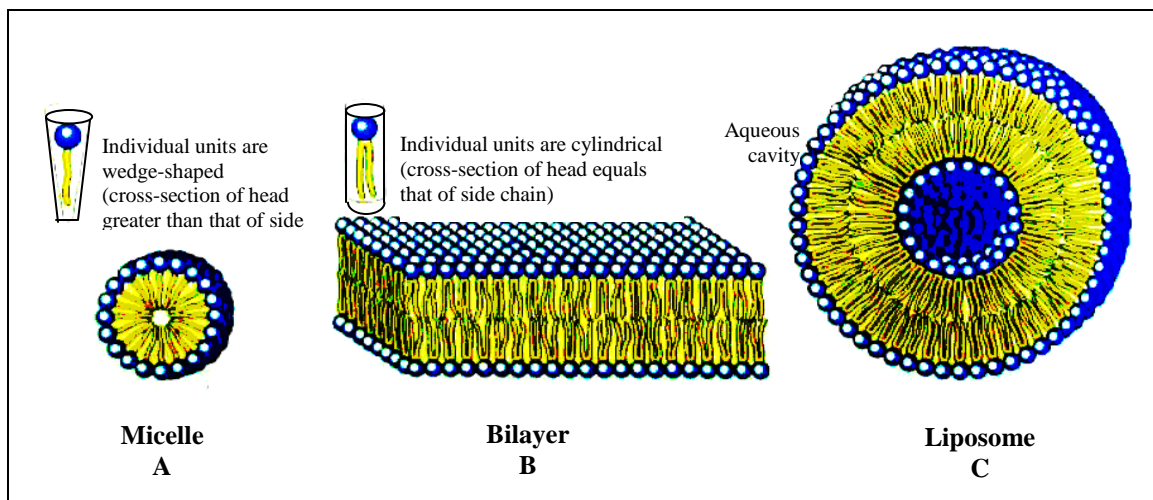


Figure 1.3. Aggregation forms of the amphiphilic molecules in water: (A) micelle; (B) bilayer; (C) liposome.³⁸

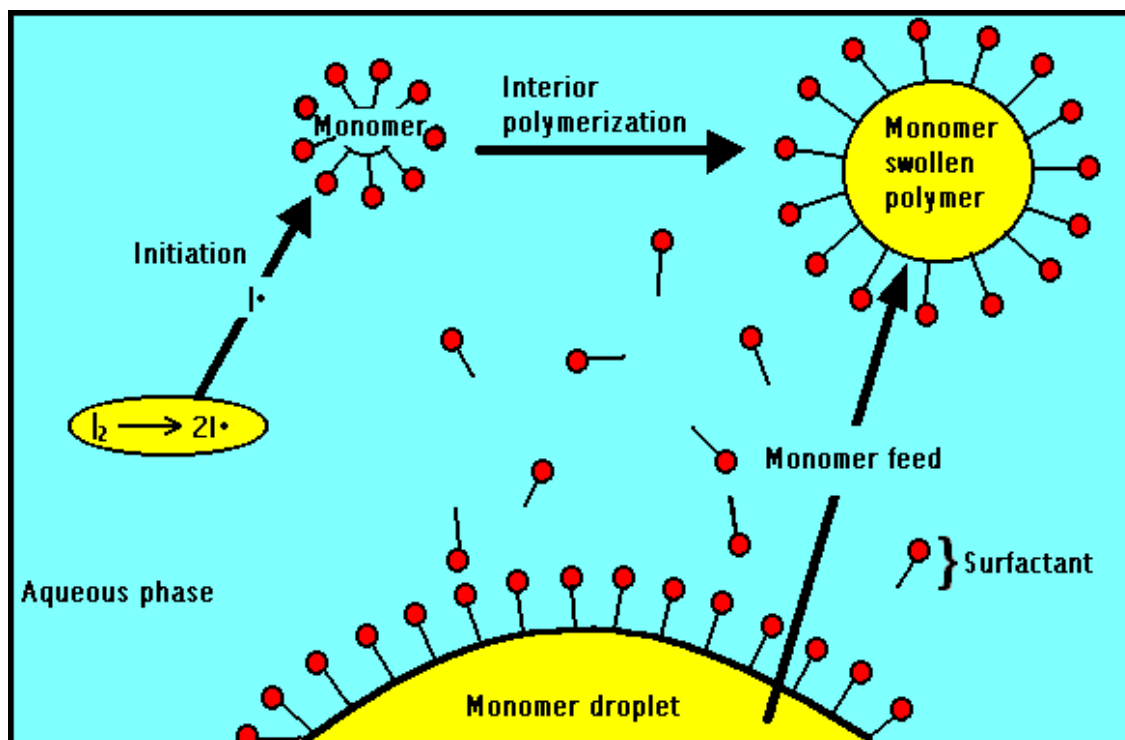


Figure 1.4. Schematic process of emulsion polymerization.⁴⁰

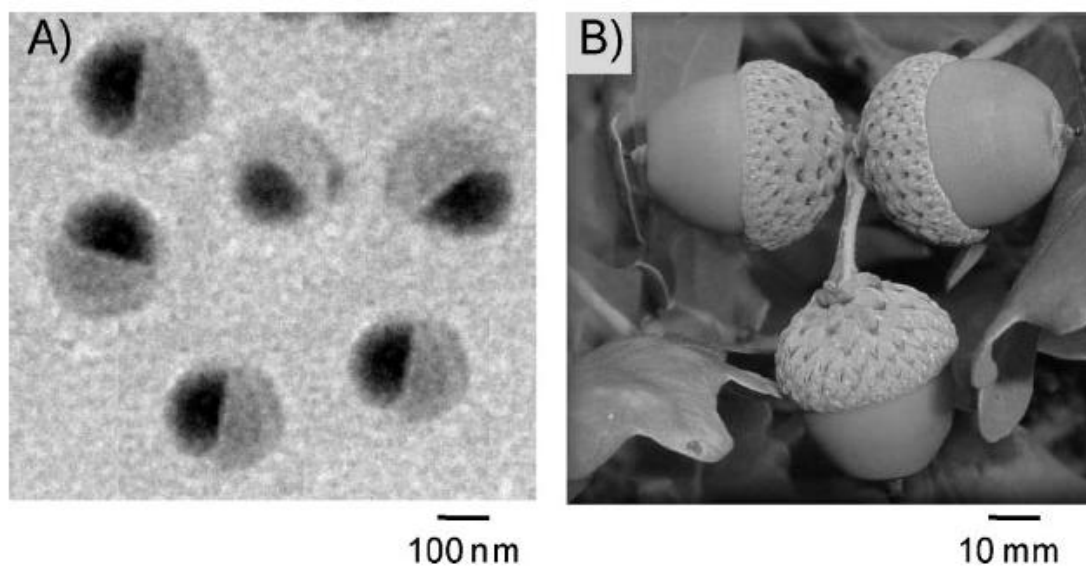


Figure 1.5. TEM micrograph of the acorn-shaped morphology of the synthesized colloidal particles (A) and an optical image of acorns from nature (B).⁴⁴

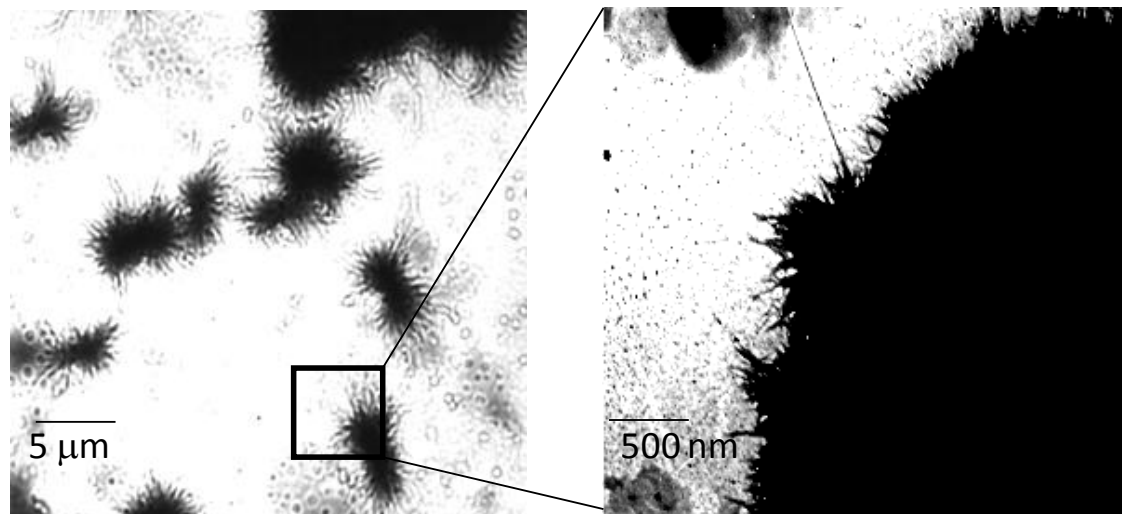
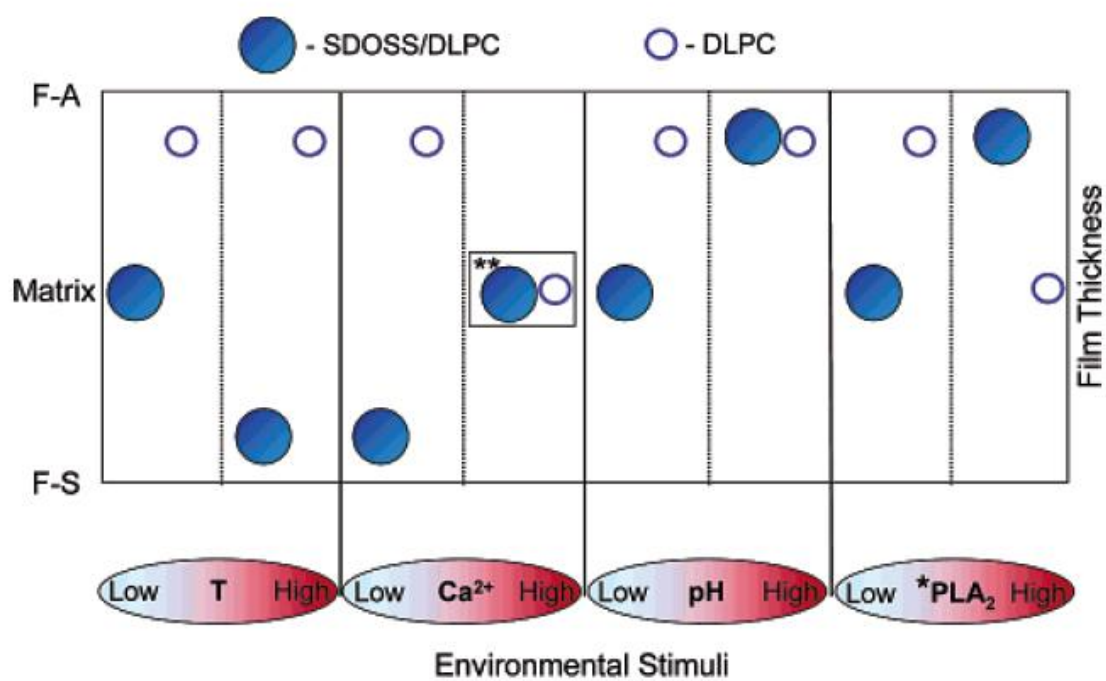


Figure 1.6. TEM micrographs of p-MMA/nBA containing DCPC using extrusion polymerization.⁴⁶



*PLA₂ enzyme at low and high pH values.

**Excessive coagulation.

Figure 1.7. Schematic diagram illustrating the mobility of SDOSS/DLPC and DLPC stabilizing components to the F-A and F-S interfaces in response to temperature, ionic strength, pH and phospholipase A₂ changes.⁴⁸

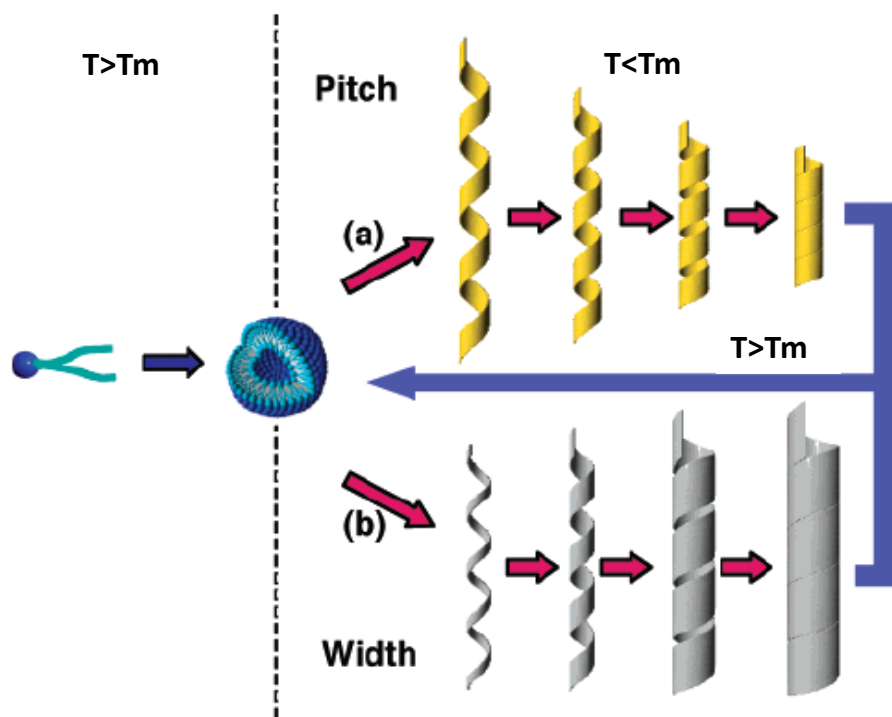


Figure 1.8. Proposed formation mechanism of lipid tubules resulting from chiral molecular self-assembly.⁶⁵

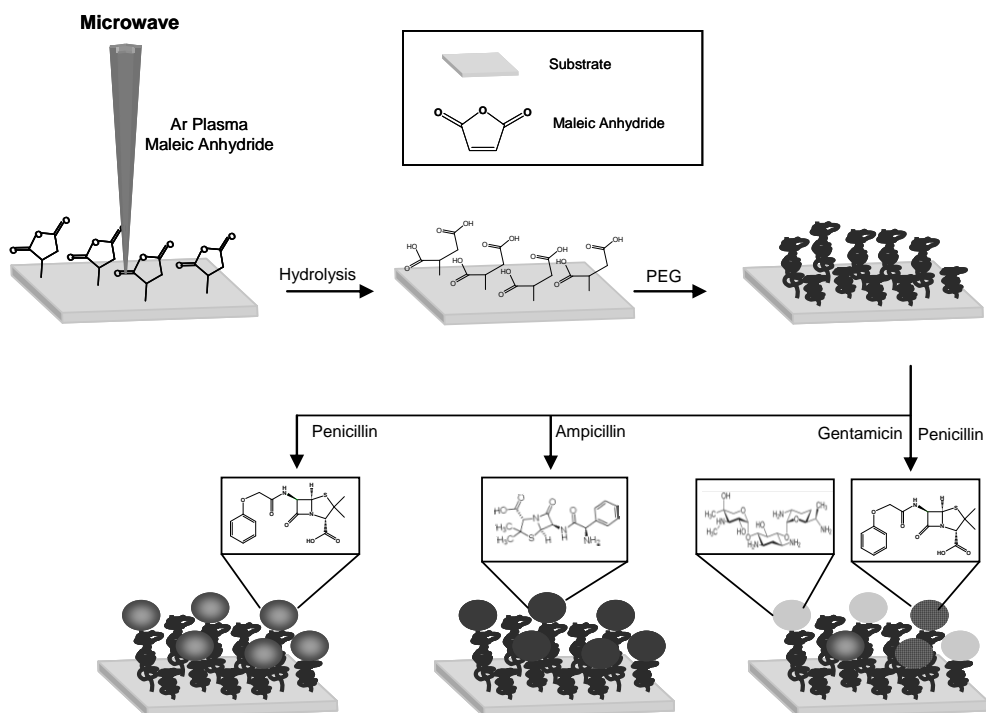


Figure 1.9. Schematic diagram of Ar microwave plasma reactions in the presence of maleic anhydride leading to the formation of -COOH groups, followed by PEG attachment and bioactive molecules to functionalized surfaces.^{119,123-125}

References

- (1) Iijima, S. *Nature* **1991**, *354*, 56.
- (2) Lehn, J. M. *Angew. Chem. Int. Ed.* **1988**, *27*, 89.
- (3) Ghosh, B.; Urban, M. W. *Science* **2009**, *323*, 1458.
- (4) Gellman, S. H. *Chem. Rev.* **1997**, *97*, 1231.
- (5) Lin, V. S. Y.; Motesharei, K.; Dancil, K.-P. S.; Sailor, M. J.; Ghadiri, M. R. *Science* **1997**, *278*, 840.
- (6) Peczuh, M. W.; Hamilton, A. D. *Chem. Rev.* **2000**, *100*, 2479.
- (7) Kruppa, M.; Konig, B. *Chem. Rev.* **2006**, *106*, 3520.
- (8) Pugliese, L.; Coda, A.; Malcovati, M.; Bolognesi, M. *J. Mol. Biol.* **1993**, *231*, 698.
- (9) Dai, J.; Bao, Z.; Sun, L.; Hong, S. U.; Baker, G. L.; Bruening, M. L. *Langmuir* **2006**, *22*, 4274.
- (10) Verma, A.; Rotello, V. M. *Chem. Commun.* **2005**, 303.
- (11) Arvizo, R. R.; Verma, A.; Rotello, V. M. *Super. Chem.* **2005**, *17*, 155.
- (12) Goodman, C. M.; Rotello, V. M. *Mini-Rev. Org. Chem.* **2004**, *1*, 103.
- (13) Serizawa, T.; Yasunaga, S.; Akashi, M. *Biomacromolecules* **2001**, *2*, 469.
- (14) Stayton, P. S.; Shimoboji, T.; Long, C.; Chilkoti, A.; Chen, G.; Harris, J. M.; Hoffman, A. S. *Nature* **1995**, *378*, 472.
- (15) Hashidzume, A.; Harada, A. *Polymer* **2006**, *47*, 3448.
- (16) Annaka, M.; Tanaka, T. *Nature* **1992**, *30*, 430.
- (17) Oya, T.; Enoki, T.; Grosberg, A. Y.; Masamune, S.; Sakiyama, T.; Takeoka, Y.; Tanaka, K.; Wang, G.; Yilmaz, Y.; Feld, M. S.; Dasari, R.; Tanaka, T. *Science* **1999**, *286*, 1543.

- (18) Watanabe, M.; Akahoshi, T.; Tabata, Y.; Nakayama, D. *J. Am. Chem. Soc.* **1998**, *120*, 5577.
- (19) Bergmann, N. M.; Peppas, N. A. *Prog. Polym. Sci.* **2008**, *33*, 271.
- (20) Kan, X. W.; Geng, Z. R.; Zhao, Y.; Wang, Z. L.; Zhu, J. J. *Nanotechnology* **2009**, *20*, 165601.
- (21) Xia, Y. Q.; Guo, T. Y.; Song, M. D.; Zhang, B. H.; Zhang, B. L. *Biomacromolecules* **2005**, *6*, 2601.
- (22) Kan, X.; Geng, Z.; Zhao, Y.; Wang, Z.; Zhu, J.-J. *Nanotech.* **2009**, *20*, 165601.
- (23) Jozefowicz, M.; Jozefonvicz, J. *Biomaterials* **1997**, *18*, 1633.
- (24) Mauzac, M.; Maillet, F.; Jozefonvicz, J.; Kazatchkine, M. D. *Biomaterials* **1985**, *6*, 61.
- (25) Thomas, H.; Maillet, F.; Letourneur, D.; Jozefonvicz, J.; Kazatchkine, M. D. *Biomaterials* **1995**, *16*, 1163.
- (26) Aubert, N.; Reach, G.; Serne, H.; Jozefowicz, M. *J. Biomed. Mater. Res.*, **1987**, *21*, 585.
- (27) Oturan, N.; Serne, H.; Reach, G.; Jozefowicz, M. *J. Biomed. Mater. Res.* **1993**, *27*, 705.
- (28) Stanilawski, L.; Serne, H.; Stanilawski, M.; Jozefowicz, M. *J. Biomed. Mater. Res.* **1993**, *27*, 619.
- (29) Leach, A. R. *Molecular Modelling: Principles and Applications*; 2nd ed.; Pearson Education Limited: Harlow, England, 2001.
- (30) Koltover, I.; Salditt, T.; Radler, J. O.; Safinya, C. R. *Science* **1998**, *281*, 78.
- (31) Dan, N. *Biochim. Biophys. Acta* **1998**, *1369*, 34.

- (32) May, S.; Harries, D.; Ben-Shaul, A. *Biophys. J.* **2000**, 78, 1681.
- (33) D'yachkov, P. N.; Fedorov, B. B.; Bischoff, R.; Bischoff, G.; Zhdanov, R. I. *Bioelectrochem.* **2002**, 58, 47.
- (34) Shrivastava, I. H.; Capener, C. E.; Forrest, L. R.; Sansom, M. S. P. *Biophys. J.* **2000**, 78, 79.
- (35) Henthorn, D. B.; Peppas, N. A. *Ind. Eng. Chem. Res.* **2007**, 46, 6084.
- (36) Piletska, E.; Piletsky, S.; Karim, K.; Terpetschnig, E.; Turner, A. *Anal. Chim. Acta* **2004**, 504, 179.
- (37) Donga, W.; Yan, M.; Liu, Z.; Wu, G.; Li, Y. *Separ. Purif. Tech.* **2007**, 53, 183.
- (38) Lehninger, A. L. *Principles of Biochemistry*, 2001.
- (39) Lovell, P. A.; El-Aasser, M. S. *Emulsion Polymerization and Emulsion Polymers*; John Wiley and Sons, 1997.
- (40) Odian, G. *Principles of Polymerization*; John Wiley and Sons, 1991.
- (41) Zhao, Y.; Urban, M. W. *Macromolecules* **2000**, 33, 8426.
- (42) Cho, I.; Lee, K. W. *J. Appl. Polym. Sci.* **1985**, 30, 1903.
- (43) Chen, Y. C.; Dimonie, V. L.; El-Aasser, M. S. *J. Appl. Polym. Sci.* **1991**, 42, 1049.
- (44) Misra, A.; Urban, M. W. *Macro. Rapid Commun.* **2009**, 30, DOI: 10.1002/marc.200900233.
- (45) Chen, Y. C.; Dimonie, V. L.; El-Aasser, M. S. *Macromolecules* **1991**, 24, 3779.
- (46) Lestage, D. J.; Urban, M. W. *Langmuir* **2005**, 21, 10254.
- (47) Lestage, D. J.; Urban, M. W. *Langmuir* **2005**, 21, 6753.
- (48) Lestage, D. J.; Urban, M. W. *Biomacromolecules* **2005**, 6, 1561.
- (49) Lestage, D. J.; Urban, M. W. *Langmuir* **2005**, 21, 2150.

- (50) Lestage, D. J.; Schleis, D. J.; Urban, M. W. *Langmuir* **2004**, *20*, 7027.
- (51) Misra, A.; Dreher, W. R.; Urban, M. W. *Langmuir* **2006**, *22*, 524.
- (52) Misra, A.; Jarrett, W. L.; Urban, M. W. *Macromolecules* **2007**, *40*.
- (53) Landfester, K.; Rothe, R.; Antonietti, M. *Macromolecules* **2002**, *35*, 1658.
- (54) Ha, J.; Park, I.; Lee, S.; Kim, D. *Macromolecules* **2002**, *35*, 6811.
- (55) Dreher, W. R.; Singh, A.; Urban, M. W. *Macromolecules* **2005**, *38*, 4666.
- (56) Dreher, W. R.; Jarrett, W. L.; Urban, M. W. *Macromolecules* **2005**, *38*, 2205.
- (57) Yager, P.; Schoen, P. E. *Mol. Cryst. Liq. Cryst.* **1984**, *106*, 371.
- (58) Schoen, P. E.; Yager, P. *J. Polym. Sci. Polym. Phys. Ed.* **1985**, *23*, 2203.
- (59) Georger, J. H.; Singh, A.; Price, R. R.; Schnur, J. M.; Yager, P.; Schoen, P. E. *J. Am. Chem. Soc.* **1987**, *109*, 6169.
- (60) Ratna, B. R.; Baral-Tosh, S.; Kahn, B.; Schnur, J. M.; Rudolph, A. S. *Chem. Phys. Lipids* **1992**, *63*, 47.
- (61) Mishra, B. K.; Thomas, B. N. *J. Am. Chem. Soc.* **2002**, *124*, 6866-6871.
- (62) de Gennes, P. G. *C. R. Acad. Sci* **1987**, *304*, 259.
- (63) Lubensky, T. C.; Prost, J. *J. Phys. II* **1992**, *2*, 371.
- (64) Spector, M. S.; Selinger, J. V.; Singh, A.; Rodriguez, J. M.; Price, R. R.; Schnur, J. *M. Langmuir* **1998**, *14*, 3493.
- (65) Shimizu, T.; Masuda, M.; Minamikawa, H. *Chem. Rev.* **2005**, *105*, 1401.
- (66) Schnur, J. M.; Price, R.; Schoen, P.; Yager, P.; Calvert, J. M.; Georger, J.; Singh, A. *Thin Solid Films* **1987**, *152*, 181.
- (67) Krebs, J. J.; Rubinstein, R.; Lubitz, P.; Harford, M. Z.; Baral, S.; Shashidhar, R.; Ho, Y. S.; Chow, G. M.; Qadri, S. *J. Appl. Phys.* **1991**, *70*, 6404.

- (68) Chappell, J. S.; Yager, P. *J. Mater. Sci. Lett.* **1992**, *11*, 633.
- (69) Markowitz, M.; Baral, S.; Brandow, S.; Singh, A. *Thin Solid Films* **1993**, *224*, 242.
- (70) Letellier, D.; Cabuil, V. *Prog. Colloid Polym. Sci.* **2001**, *118*, 248.
- (71) Patil, A. J.; Muthusamy, E.; Seddon, A. M.; Mann, S. *Adv. Mater.* **2003**, *15*, 1816.
- (72) Yang, B.; Kamiya, S.; Shimizu, Y.; Koshizaki, N.; Shimizu, T. *Chem. Mater.* **2004**, *16*, 2826.
- (73) Price, R.; Patchan, M.; Clare, A.; Ricttschof, D.; Bonaventura, J. *Biofouling* **1992**, *6*, 207.
- (74) Baral, S.; Schoen, P. *Chem. Mater.* **1993**, *5*, 145.
- (75) Patil, A. J.; Muthusamy, E.; Seddon, A. M.; S., M. *Adv. Mater.* **2003**, *15*, 1816.
- (76) Lvov, Y. M.; Price, R. R.; Selinger, J. V.; Singh, A.; Spector, M. S.; Schnur, J. M. *Langmuir* **2000**, *16*, 5932.
- (77) Lvov, Y. M.; Price, R. R. *Colloids Surf., B* **2002**, *23*, 251.
- (78) Goren, M.; Qi, Z.; Lennox, R. B. *Chem. Mater.* **2000**, *12*, 1222.
- (79) Schnur, J. M. *Science* **1993**, *262*, 1669.
- (80) Wachowiak, A.; Wiebe, J.; Bode, M.; Pietzsch, O.; Morgenstern, M.; Wiesendanger, R. *Science* **2002**, *298*, 577.
- (81) Choe, S. B.; Acremann, Y.; Scholl, A.; Bauer, A.; Doran, A.; St öhr, J.; Padmore, H. A. *Science* **2004**, *304*, 420.
- (82) Corten, C.; Urban, M. W. *Adv. Mater.* **2009**, DOI: 10.1002/adma.200901940.
- (83) Pankhurst, Q. A.; Connolly, J.; Jones, S. K.; Dobson, J. J. *Phys. D: Appl. Phys.* **2003**, *36*, R167.

- (84) Lu, A. H.; Salabas, E. L.; Schuth, F. *Angew. Chem. Int. Ed.* **2007**, *46*, 1222.
- (85) Son, S. J.; Reichel, J.; He, B.; Schuchman, M.; Lee, S. B. *J. Am. Chem. Soc.* **2005**, *127*, 7316.
- (86) Ma, H.; Tarr, J.; DeCoster, M. A.; McNamara, J.; Caruntu, D.; Chen, J. F.; O'Connor, C. J.; Zhou, W. L. *J. Appl. Phys.* **2009**, *105*, 07B309.
- (87) Nielsch, K.; Castano, F. J.; Matthias, S.; Lee, W.; Ross, C. A. *Adv. Eng. Mater.* **2005**, *7*, 217.
- (88) Daub, M.; Knez, M.; Goesele, U.; Nielsch, K. *J. Appl. Phys.* **2007**, *101*, 09J111.
- (89) Sui, Y. C.; Skomski, R.; Sorge, K. D.; Sellmyer, D. J. *J. Appl. Phys.* **2004**, *95*, 7151.
- (90) Suber, L.; Imperatori, P.; Ausanio, G.; Fabbri, F.; Hofmeister, H. *J. Phys. Chem. B* **2005**, *109*, 7103.
- (91) Li, F.; Song, L. J.; Zhou, D.; Wang, T.; Wang, Y.; Wang, H. B. *J. Mater. Sci.* **2007**, *42*, 7214.
- (92) Liu, L.; Kou, H.; Mo, W.; Liu, H.; Wang, Y. *J. Phys. Chem. B* **2006**, *110*, 15218.
- (93) Lee, D.; Cohen, R. E.; Rubner, M. F. *Langmuir* **2007**, *23*, 123.
- (94) He, Q.; Tian, Y.; Cui, Y.; Mohwald, H.; Li, J. B. *J. Mater. Chem.* **2008**, *18*, 748.
- (95) Liu, Z. Q.; Zhang, D. H.; Han, S.; Li, C.; Lei, B.; Lu, W. G.; Fang, J. Y.; Zhou, C. W. *J. Am. Chem. Soc.* **2004**, *127*, 6.
- (96) Shenton, W.; Douglas, T.; Young, M.; Stubbs, G.; Mann, S. *Adv. Mater.* **1999**, *11*, 253.
- (97) Banerjee, I. A.; Yu, L. T.; Shima, M.; Yoshino, T.; Takeyama, H.; Matsunaga, T.; Matsui, H. *Adv. Mater.* **2005**, *17*, 1128.

- (98) Lv, B. L.; Xu, Y.; Wu, D.; Sun, Y. H. *Particuology* **2008**, *6*, 334.
- (99) Schnui, J. M. *Science* **1993**, *262*, 1669.
- (100) Yu, M.; Urban, M. W. *J. Mater. Chem.* **2007**, *17*, 4644.
- (101) Escrig, J.; Landeros, P.; Altbir, D.; Vogel, E. E.; Vargas, P. *J. Magn. Magn. Mater.* **2007**, *308*, 233.
- (102) Escrig, J.; Altbir, D.; Nielsch, K. *Nanotechnology* **2007**, *18*, 225704.
- (103) Konstantinova, E. *J. Magn. Magn. Mater.* **2008**, *320*, 2721.
- (104) Escrig, J.; Landeros, P.; Altbir, D.; Vogel, E. E. *J. Magn. Magn. Mater.* **2007**, *310*, 2448.
- (105) Chen, A. P.; Usov, N. A.; Blanco, J. M.; Gonzalez, J. *J. Magn. Magn. Mater.* **2007**, *316*, e317.
- (106) Landeros, P.; Suarez, Q. J.; Cuchillo, A.; Vargas, P. *Phys. Rev.* **2009**, *79*, 024404.
- (107) Magrez, A.; Kasas, S.; Salicio, V.; Pasquier, N.; Seo, J. W.; Celio, M.; Catsicas, S.; Schwaller, B.; Forro, L. *Nano Lett.* **2006**, *6*, 1121.
- (108) Kang, S.; Herzberg, M.; Rodrigues, D. F.; Elimelech, M. *Langmuir* **2008**, *24*, 6409.
- (109) Jia, G.; Wang, H. F.; Yan, L.; Wang, X.; Pei, R. J.; Yan, T.; Zhao, Y. L.; Guo, X. *B. Environ. Sci. Technol.* **2005**, *39*, 1378.
- (110) Ding, Y. H.; Stilwell, J.; Zhang, T. T.; Elboudwarej, O.; Jiang, H. J.; Selegue, J. P.; Cooke, P. A.; Gray, J. W.; Chen, F. F. *Nano Lett.* **2005**, *5*, 2448.
- (111) Chen, X.; Tam, U. C.; Czapinski, J. L.; Lee, G. S.; Rabuka, D.; Zettl, A.; Bertozzi, C. R. *J. Am. Chem. Soc.* **2006**, *128*, 6292.

- (112) Dumortier, H.; Lacotte, S.; Pastorin, G.; Marega, R.; Wu, W.; Bonifazi, D.; Briand, J. P.; Prato, M.; Muller, S.; Bianco, A. *Nano Lett.* **2006**, *6*, 1522.
- (113) Worle-Knirsch, J. M.; Pulskamp, K.; Krug, H. F. *Nano Lett.* **2006**, *6*, 1261.
- (114) Zhu, Y.; Ran, T. C.; Li, Y. G.; Guo, J. X.; Li, W. X. *Nanotechnology* **2006**, *17*, 4668.
- (115) Kang, S.; Pinault, M.; Pfefferle, L.; Elimelech, M. *Langmuir* **2007**, *23*, 8670.
- (116) Nepal, D.; Balasubramanian, S.; Simonian, A. L.; Davis, V. A. *Nano Lett.* **2008**, *8*, 1896.
- (117) Kenawy, E. R.; Worley, S. D.; Broughton, R. *Biomacromolecules* **2007**, *8*, 1359.
- (118) Roy, D.; Knapp, J. S.; Guthrie, J. T.; Perrier, S. *Biomacromolecules* **2008**, *9*, 91.
- (119) Aumsuwan, N.; Heinhorst, S.; Urban, M. W. *Biomacromolecules* **2007**, *8*, 713.
- (120) Lee, S. B.; Koepsel, R. R.; Morley, S. W.; Matyjaszewski, K.; Sun, Y.; Russell, A. *J. Biomacromolecules* **2004**, *5*, 877.
- (121) Kidane, A. G.; Salacinski, H.; Tiwari, A.; Bruckdorfer, K. R.; Seifalian, A. M. *Biomacromolecules* **2004**, *5*, 798.
- (122) Aumsuwan, N.; Heinhorst, S.; Urban, M. W. *Biomacromolecules* **2007**, *8*, 3525.
- (123) Aumsuwan, N.; Danyus, R. C.; Heinhorst, S.; Urban, M. W. *Biomacromolecules* **2008**, *9*, 1712.
- (124) Bae, W. S.; Urban, M. W. *Langmuir* **2004**, *20*, 8372.
- (125) Zhao, Y.; Urban, M. W. *Langmuir* **1999**, *15*, 3538.

CHAPTER II

MOLECULAR RECOGNITION AT METHYL METHACRYLATE/N-BUTYL
ACRYLATE (MMA/NBA) MONOMER UNIT BOUNDARIES OF PHOSPHOLIPIDS
AT P-MMA/NBA COPOLYMER SURFACES

Introduction

Non-covalent interactions play an important role in biological systems and there are numerous examples of molecular recognition at interfaces ranging from crystal interfaces^{1,2} to base-pairing,³ peptide and DNA recognition,^{4,5} and sensing.⁶ Mother Nature has mastered these processes and, with just a few building blocks, is capable of signaling and recognizing subtle changes through manipulations of non-covalent, typically weak hydrogen bonding interactions. One biopolymer that is capable of encoding genetic data is DNA, and among other functions its sequence determines the type of organism or disease susceptibility, but its critical feature is the ability to precisely encode a specific protein sequence.⁵ The key component in these processes is molecular recognition and the ability of selective binding to specific molecular segments. Another example is proper matching between hydrophobic components of proteins with more flexible lipid molecules which tend to surround the former by matching sizes and shapes. Due to protein rigidity and relatively flexible lipids, the conditions of hydrophobic matching can be accomplished by structural rearrangements of lipid rafts. The main question in these and other studies is what chemical entities are responsible for structural matching and molecular recognition? Thus, one of the challenges, and at the same time opportunity for creating materials with supermolecular structures with signaling

characteristics, is their ability of recognizing other species not necessarily via covalent bond formation, but other typically weaker, but orchestrated interactions.

In view of these considerations, we recently explored film formation processes of colloidal particles that were deliberately stabilized by biologically active and surface stabilizing phospholipids (PL).⁷⁻¹⁰ These studies showed that colloid particle morphologies play an essential role in coalescence and exhibit particular influence on interfacial regions near the film-air (F-A) and film-substrate (F-S) interfaces. One of the outcomes of these studies was the formation of surface localized rafts that exhibit stimuli-responsive characteristics controlled by colloidal particle-phospholipid interactions as well as pH and temperature. These surface entities resemble the natural phenomena of membrane lipid rafts and may have significant implications on further advances leading to understanding mechanistic aspects of cell-cell signaling, endocytosis, and raft-raft cross-talk.^{11,12} During the course of these studies unique structural features were identified which were inherently associated with particle coalescence and copolymer composition, as well as structural features of biologically active phospholipids. It turns out that colloidal particle coalescence provides a unique environment for PLs stratification near the F-A and F-S interfaces, which is driven by an access of the surface energy at the interfacial regions, thus often facilitating PL mobility. One of the intriguing phenomena was the ability of PLs to form well organized surface entities referred to as surface localized ionic clusters (SLICs) which form only during particle coalescence and are composed of PLs or a combination of PL and other dispersing agents. Several mechanisms leading to stratification of these species were proposed.⁷⁻¹⁰

Since structural features and interactions of SLICs composed of PLs with polymer surfaces are important for facilitating either attachment or growth of biocomponents to or from polymeric surfaces, this study attempts to determine what structural features are responsible for molecular recognition of PLs and interactions that lead to SLIC formation on poly(methyl methacrylate/*n*-butyl acrylate) (p-MMA/*n*BA) film surfaces. For that reason synthetic and spectroscopic efforts along with molecular modeling will be employed to advance limited knowledge that may enhance comprehension of lipid-protein recognition and interactions between biological and synthetic systems.

As have been shown in our previous studies, during coalescence of p-MMA/*n*BA colloidal particles stabilized by biologically active phospholipid dispersing agents SLICs are formed at the F-A and F-S interfaces.⁷⁻¹⁰ Figure 2.1 illustrates an optical image obtained from the F-A of 1,2-dilauroyl-*sn*-glycero-3-phosphocholine (DLPC)-stabilized p-MMA/*n*BA films and show that crystalline SLIC entities are observed. The F-S interface does not show these features (not shown). For the same copolymer matrix, but prepared in the presence of sodium dioctylsulfosuccinate/1,2-dilauroyl-*sn*-glycero-3-phosphocholine (SDOSS/DLPC), these species are not observed under ambient conditions. If they were formed, their formation would occur only during coalescence of colloidal particles and a number of control experiments in which DLPC and other PLs were solidified from an aqueous phase resulted in the formation of a powdery PL. Thus, the formation of SLICs occurs only in certain areas of coalesced films, thus raising two questions: (1) what chemical entities at the p-MMA/*n*BA surfaces are responsible for the initiation of SLIC formation, and (2) why the presence of colloidal particles facilitates selective SLIC formation.

Experimental

Methyl methacrylate (MMA), *n*-butyl acrylate (nBA), sodium dioctylsulfosuccinate (SDOSS), and potassium persulfate (KPS) were purchased from Aldrich Chemical Co. 1,2-dilauroyl-*sn*-glycero-3-phosphocholine (DLPC) phospholipid was purchased from Avanti Polar Lipids, Inc. p-MMA/nBA copolymer emulsions stabilized by DLPC and SDOSS/DLPC were synthesized, following the procedure outlined earlier.⁹ p-MMA and p-nBA homopolymers containing DLPC were prepared by the same procedure.

The particle size measurements were performed on a Macrotrac Nanotrac 250 instrument. Optical micrographs of film surfaces were obtained using a Nikon Optiphot biological microscope equipped with cross-polarizers. Microscopic attenuated total reflectance Fourier transform infrared (ATR FT-IR) spectroscopic measurements were performed on the film-air (F-A) and film-substrate (F-S) interfaces using a Bio-Rad FTS-6000 FT-IR single-beam spectrometer with 4 cm⁻¹ resolution. The surfaces were analyzed using a 2 mm Ge crystal with a 45 ° angle maintaining constant contact pressure between the crystal and the specimens. All spectra were corrected for spectral distortions using software for the Urban-Huang algorithm.¹³ Selected area electron diffraction (SAD) patterns of samples were obtained using a Jeol JEM-2100 transmission electron microscope (TEM) operated at 200 kV.

Computer simulations were carried out in order to determine structural features of SLICs. The choice of theoretical level depends on the accuracy requested and the size of a system. It is well known that DFT-B3LYP method predicts excellent geometries,^{14,15} however, due to the large size of the SLICs systems under consideration, computer

simulations at AM1, HF/3-21G, B3LYP¹⁶⁻¹⁹/6-31G, and B3LYP/6-31G+(d) levels were employed. It has been proven that the HF/3-21G method well reproduces the geometrical parameters. Thus only the models optimized at the HF/3-21G²⁰⁻²² level are discussed in this work unless mentioned otherwise. The characteristics of the local minima were verified by vibration frequency calculations. The harmonic vibrational wavenumbers and absolute intensities were calculated at the same level using the HF/3-21G optimized structures. The values of the wavenumbers were scaled by a factor of 0.964 for HF/3-21G level of theory.^{23,24} All calculations were carried out using the Gaussian 03 package.²⁵

Results and Discussion

We utilized ATR FT-IR spectroscopy which allows us to analyze chemical entities at the F-A and F-S interfaces of p-MMA/nBA films. The results of the analysis are illustrated in Figure 2.2, and Traces A/A' and B/B' show spectra recorded from the F-A and F-S interfaces, respectively. The spectra were recorded using TE (Traces A, B) and TM (Traces A', B') polarizations in order to determine dichroic ratios of selected bands, and establish preferential spatial orientation of given species responsible for these vibrations. Analysis and comparison of the spectra recorded from the F-A and F-S interfaces show the presence of the bands at 1310, 1300, 1265, and 1250 cm⁻¹ which are not present at the F-S interface. Furthermore, enhanced intensity of the band at 1061 cm⁻¹ due to P-O-C segments of DLPC in the TM polarization is observed, with the dichroic ratio of 0.235. The P-O-C orientation changes originate from the ionic segments of DLPC. These observations indicate preferentially perpendicular orientation of the DLPC head groups with respect to the F-A interface. As shown in Trace C, no IR bands due to SLICs are detected in the films coalesced from the particles stabilized by SDOSS/DLPC.⁹ For

reference purposes, Traces D and E of Figure 2.2 illustrate the spectra of DLPC and p-MMA/nBA/SDOSS, respectively, and show virtually no resemblance of the spectra recorded from the F-A and F-S interfaces (Traces A/A' and B/B') with the exception of the strong bands at 1148 and 1162 cm^{-1} due to C-O of MMA and nBA units.

Before we attempt to address these spectroscopic differences reflecting significant chemical differences, it should be also noted that SDOSS/DLPC stabilized particles exhibit monomodal particle distribution with an average particle size of 132 nm, whereas the same DLPC-stabilized colloidal particles are 69 nm in diameter. These observations indicate that SDOSS/DLPC form larger miscible micelles and form monomodal particles during synthesis. In contrast, previous studies have shown that when hydrogenated soybean phosphatidylcholine (HSPC) and SDOSS are utilized, formation of bimodal particle distribution⁷ was observed, which was attributed to dissimilar hydrophobicity and compatibility of HSPC and SDOSS. Furthermore, as shown in Trace C of Figure 2.2, the presence of SDOSS inhibits DLPC mobility, and thus does not facilitate SLIC formation.⁷ This is attributed to ionic interactions between NH_3^+ of DLPC and SO_3^- of SDOSS at the particle interfaces, which inhibit DLPC migration, and is schematically illustrated in Figure 2.3, A. However, the presence of ionic interactions between NH_3^+ and PO_4^{2-} groups of two DLPC molecules and the hydrophilic nature of phosphocholine groups of DLPC facilitates SLICs formation. As water evaporates, DLPC molecules are released from the particle surfaces and migrate to the F-A interface being forced out of the interfacial regions. This is schematically depicted in Figure 2.3, B. Thus, there is a significant influence of dispersing agents and their interactions with colloidal particles on mobility and stratification during coalescence.

In an effort to establish the influence of the polymer matrix on SLIC formation, ATR FTIR spectra were recorded from the F-A interfaces of DLPC stabilized p-MMA and p-nBA homopolymers, and their blend films. As illustrated in Figure 2.4, Traces A/A', ATR FT-IR spectra collected from the F-A interface of a 50/50 p-MMA/p-nBA blend stabilized by DLPC reveal the presence of SLICs, as manifested by the presence of the bands at 1310, 1300, 1265, 1250, and 1061 cm^{-1} due to SLICs. In contrast, these bands are not detected in Traces B/B' and C/C', which represent the spectra recorded from the F-A interface of p-MMA and p-nBA homopolymers containing DLPC. Although these data suggest that the formation of SLICs is attributed to the simultaneous presence of MMA, nBA, and DLPC, further evidence is necessary to determine the origin of their formation and the location of SLICs on the p-MMA/nBA surface.

As indicated above, the formation of SLICs occurs only during particle coalescence, whereas disturbance of the particle surface by other species inhibits or promotes migration to the interfaces, depending upon the nature of chemical interactions. Numerous experimental attempts to recreate SLIC formation outside the colloidal environment resulted in failure, and it became clear that structural features of SLICs are unique, and a prerequisite for their formation is the particle coalescence. Although one could attribute the interfacial surface tension between collating particles generating capillary forces²⁶ as the main source for mobilizing DLPC to the F-A interface, we believe that this process is an intermediate stage that mobilizes PLs from particle surfaces. The first stage will require the displacement of PLs, such as depicted in Figure 2.3, B, followed by their transport via the capillary forces, and orchestrated alignment of DLPC at the F-A interface. While the first two stages are fairly well documented,²⁷ and several

factors contribute to these efforts, specific interactions that are responsible for the growth of the SLICs shown in Figure 2.1 in specific locations remain unknown.

In an effort to determine molecular entities responsible for SLIC formation, we calculated IR spectra shown in Figure 2.2 from molecular modeling experiments. For that purpose we utilized ab initio calculations in which polar ends of DLPC were allowed to interact with p-MMA/nBA copolymer backbone. This approach was stipulated by the experimental data discussed in conjunction with Figures 2.2 and 2.4. During simulations, p-MMA and p-nBA homopolymers were allowed to interact independently with DLPC through electrostatic and H-bonding attraction between the anionic phosphate-cationic quaternary ammonium pair and the carbonyls of the copolymer matrices. This choice resulted from ionic interactions detected spectroscopically and shown in Figure 2.3. Using an ab initio approach, we calculated spectral features responsible for IR bands to match experimentally determined spectra of SLICs shown in Figure 2.2. Based on the ab initio results that match the experimental data, structural features responsible for SLICs may be deduced.

Figure 2.5 A, B, C, and D illustrate possible interactions derived from the ab initio calculations and show that the most stable configuration is obtained for DLPC-p-MMA/nBA interactions. As seen in Figure 2.5, A, A', and A'', these interactions occur via DLPC-p-MMA/nBA segments and provide energetically the most stable structure. The distance between the carbonyl O of the MMA1 segment and H of the trimethylammonium of DLPC is 2.38 Å, which indicates an existence of a strong electrostatic and H-bonding interactions between them. In addition, the short distances between the carbonyl O from the nBA1 and three Hs of the trimethylammonium (2.25,

2.25, 2.94 Å) also stabilize the interaction. Although the MMA2 segment is slightly distorted away from DLPC, there is still an additional weak interaction between the carbonyl O of the MMA2 segment and three Hs of trimethylammonium of DLPC. The distances between the carbonyl O of MMA2 and three Hs of the trimethylammonium are in the range of 2.51 to 3.32 Å. Similarly, relatively weak interactions between the carbonyl O of nBA2 and the Hs of trimethylammonium on DLPC also stabilize the model A. It should be noted that the PO_2^- segment of DLPC is oriented towards the methyl of MMA and butyl groups of nBA resulting from attractive forces between the Hs of methyl and butyl groups of the polymer and O^- of PO_2^- . Based on these modeling studies, we conclude that the primary component responsible for SLIC formation results from the presence of neighboring MMA and nBA units and electrostatic attractions between DLPC at the MMA/nBA boundaries. This is illustrated in Figure 2.5, A”.

The same analysis conducted for p-MMA or p-nBA homopolymers at the MMA/MMA or nBA/nBA boundaries with structural features illustrated in Figure 2.5, B-B’ and C-C’ shows that these interactions are not stabilized. As seen in Figure 2.5, B-B’, the model for interactions between p-MMA and DLPC indicates that there are barely any interactions between the MMA1 segment and DLPC as well as the PO_2^- group and MMA1, resulting only from the interaction of methyl groups. In contrast, for p-nBA model illustrated in Figure 2.5, C-C’, the nBA2 unit is fairly distorted, and the structure is destabilized due to the presence of strong steric repulsions. These features lead to the conclusion that the binding energies of homopolymer structures are significantly less favorable and weaker than those obtained for the copolymer structure with MMA/nBA units.

In order to consider all possible scenarios of potential interactions we determined the feasibility of inter-molecular interactions between the neighboring chains of p-MMA and p-nBA homopolymer blends. The results are shown in Figure 2.5, D-D' which indicate that when a sequence of three MMA and nBA units in the neighboring chains, in the presence of DLPC, also forms SLICs. As seen, when two polymer chains are side-by-side, DLPC forms a bridge between the chains. In this case, H-bonding interactions between the carbonyl oxygen atoms of nBA1 and nBA2, the Hs of trimethyl ammonium of DLPC as well as the carbonyl oxygen atoms of MMA1, MMA2, and MMA3 with DLPC, stabilize the structure. As shown in Figure 2.5, D', which depicts the side and top views of the structure, the 50/50 p-MMA/p-nBA blend provides a similar environment for the SLIC formation as that observed for p-MMA/nBA copolymer shown in Figure 2.5, A-A". Because only three nBA units are involved in the interaction with DLPC on one side, p-nBA chains are less restrained, as that compared with that in p-MMA/nBA copolymer (Figure 2.5, A-A"), thus providing a more flexible environment for rigid pMMA chains to approach PO_2^- groups. Using ab initio calculations significant H-bonding interactions appear to play an important role in the SLIC formation. Specifically, as shown in Figure 2.5, D-D', MMA3 group can approach DLPC closer and H-bonding between the DLPC PO_2^- oxygen O2 atom and the H atoms of nBA3 and the near-neighbor MMA1 are responsible for SLIC formation. Other similar type interactions are also located between the DLPC PO_2^- oxygen O1 atom and the Hs of nBA1 and nBA3 groups which resembles the arm-chair-model structure of the copolymer.

Furthermore, this analysis shows that the existence of the neighboring of MMA and nBA units in the p-MMA/nBA backbone facilitates SLIC formation which is also

manifested by a comparison of the experimental and calculated IR spectra. Figure 2.6, Trace A, illustrates ATR FT-IR spectrum obtained by averaging of the spectra recorded in the TE and TM polarization modes at the F-A interface with the characteristic SLIC bands at 1310, 1300, and 1265, 1250, and 1061 cm^{-1} . For comparison, Trace B of 2.6 is the calculated IR spectrum obtained from the structure shown in Figure 2.5, A-A". Similar results are obtained for the 50/50 p-MMA and p-nBA homopolymer blend. Trace C of Figure 2.6 illustrates calculated IR spectrum from the structure shown in Figure 2.5, D-D'. Although not all experimental and theoretically predicted IR bands exactly match, the main calculated bands (Trace B) at 1316, 1296, 1269, 1240, 1079, 785 cm^{-1} show good agreement with the experimental results (Trace A). Similarly, for the blend (Trace C) the following bands are obtained: 1305, 1299, 1272, 1081, and 783 cm^{-1} . To illustrate which vibration contributes to specific structural features, characteristic vibrational bands and structural features responsible for these bands are summarized in Table 2.1. Table 2.1 also illustrates 3D vibrational modes responsible for the SLIC formation. The bands at 1310 and 1300 cm^{-1} are attributed to the C-(C=O) stretching and CH vibrational modes, whereas the bands at 1265 and 1250 cm^{-1} result from the CH₂ on backbone vibrational modes and C-(C=O) stretching vibrations, respectively. Finally, the band at 1061 cm^{-1} is due to P-O-C stretching, and the band at 736 cm^{-1} is attributed to P-O stretching vibrations.

Although these studies demonstrate for the first time that specificity of PL diester-type polymer interactions is attributed to the presence of MMA and nBA units next to each other, analysis of Figure 2.1 clearly illustrates the formation of crystallites. In order to determine the size of crystalline lattice of SLICs grown from the p-MMA/nBA surface,

SAD was utilized. Figure 2.7, A, illustrates the single crystal diffraction pattern of the orthorhombic lattice. Using these data we calculated the lattice constants which are 4.0 Å and 6.2 Å. As we recall the results of the ab initio calculations, the distance between DLPC molecules shown in Figure 2.5, A' gives the crystal lattice constants of 3.90 Å and 6.16 Å, which closely matches the SAD data shown in Figure 2.7, with the unit cell shown in Figure 2.7, B. For reference, Figures 2.7, C and D, illustrate electron diffraction patterns of DLPC and p-MMA/nBA containing SDOSS, respectively, which do not exhibit single crystal patterns, reinforcing earlier conclusions that the presence of colloidal particles facilitates mobility and transport of DLPC to the surface, while the presence of neighbouring MMA and nBA units next to each other facilitates SLIC formation.

Lipid-protein interactions have been studied intensively, but the detailed chemical nature of their interactions is not known. Specifically, questions that need to be address are how membrane proteins interact with the lipids surrounding the membrane proteins or do lipid molecules form shells around a membranes protein. These studies show for the first time that the presence of diester group separated by aliphatic C-C bonds facilitated by covalently bonded methyl methacrylate and n-butyl acrylate units provides a recognition site for the SLIC formation. These interactions are specific, and occur between C=O and N-(CH₃)₃ groups as H-bonding and electrostatic interactions. Although these interactions have been recognized in the protein-lipid studies, their specificity was not identified. After all, p-MMA/nBA copolymer structure and portions of protein structural features exhibit similar hydrophobic groups which may provide environments conducive for amphiphilic lipid crystallization and specific recognition site by PLs.

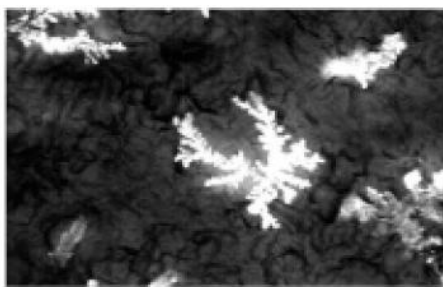
Conclusions

p-MMA/nBA colloidal dispersions were synthesized in the presence of biologically active phospholipids and upon coalescence lead to the formation of SLICs which are only formed during film formation of colloidal particles. Combination of experimental and theoretical approaches allowed us to determine the nature of the interactions between anionic phosphate groups, cationic quaternary ammonium groups of the phospholipid, and carbonyl groups of the neighboring MMA and nBA units of p-MMA/nBA copolymer. These studies show that the two neighboring MMA and nBA units along the polymer backbone provide conducive environments to signal and attract amphiphilic groups of DLPC, thus initiating SLIC formation. This process is believed to be driven by H-bonding and electrostatic interactions of both units which recognize amphiphatic characteristic species, thus resembling biological recognitions.

Table 2.1. Experimental and calculated IR bands obtained from ATR FT-IR measurements and ab initio calculations using Models A and D.

Experimental IR Band (cm ⁻¹)	Calculated IR Band (cm ⁻¹)	Vibrational Mode	3D Vibrational Modes
1310	1316 (c) 1305(b)	C-(C=O) stretching CH vibrational mode	
1300	1296 (c) 1299 (b)	C-(C=O) stretching CH vibrational mode	
1265	1269 (c) 1272 (b)	CH ₂ vibrational mode	
1250	1240 (c)	C-(C=O) stretching	
1061	1079 (c) 1081 (b)	P-O-C stretching	
736	785 (c) 783(b)	P-O stretching	

Note: c – denotes p-MMA/nBA copolymer
b – denotes 50/50 p-MMA/p-nBA homopolymer blend.



100 μm

Figure 2.1. Cross-polarized optical micrographs of DLPC stabilized p-MMA/nBA film surfaces recorded from the F-A interface.

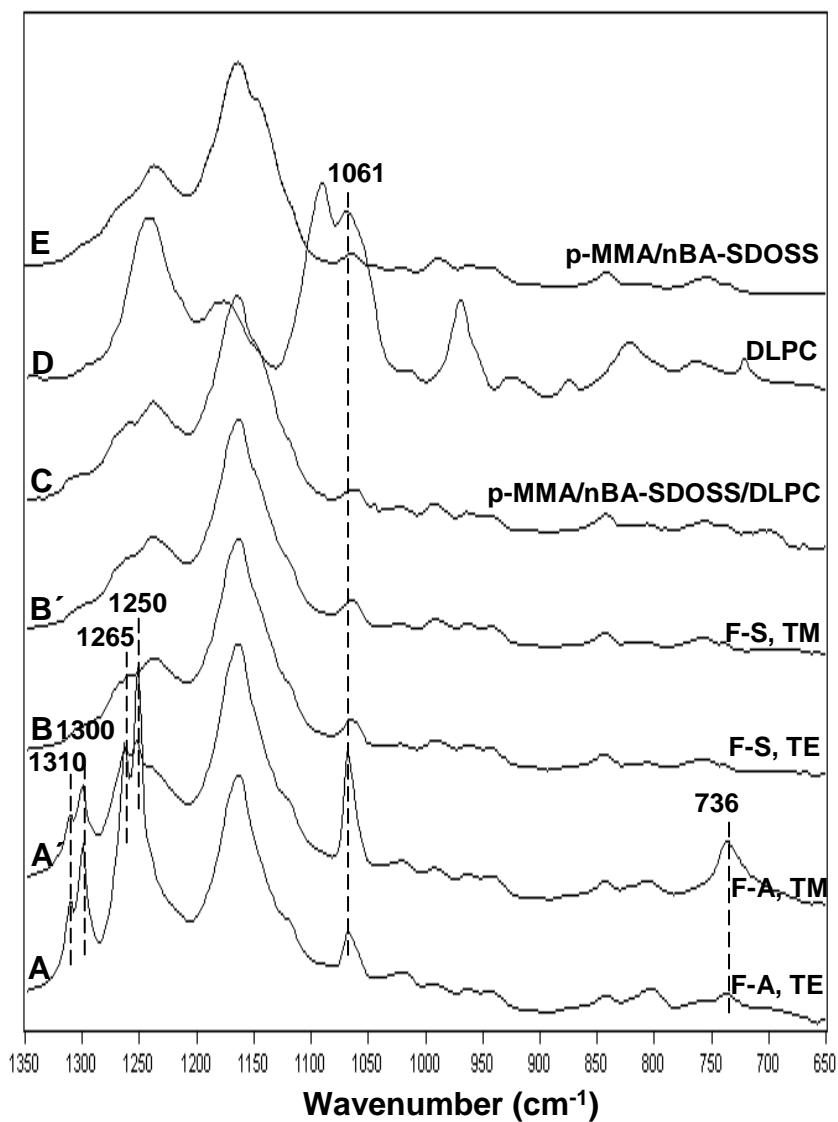


Figure 2.2. Polarized ATR-FTIR spectra of p-MMA/nBA copolymer films containing DLPC at: (A) F-A, TE polarization; (A') F-A, TM polarization; (B) F-S, TE polarization; (B') F-S, TM polarization; and reference sample: (C) p-MMA/nBA copolymer containing SDOSS/DLPC; (D) DLPC, and (E) p-MMA/nBA copolymer containing SDOSS.

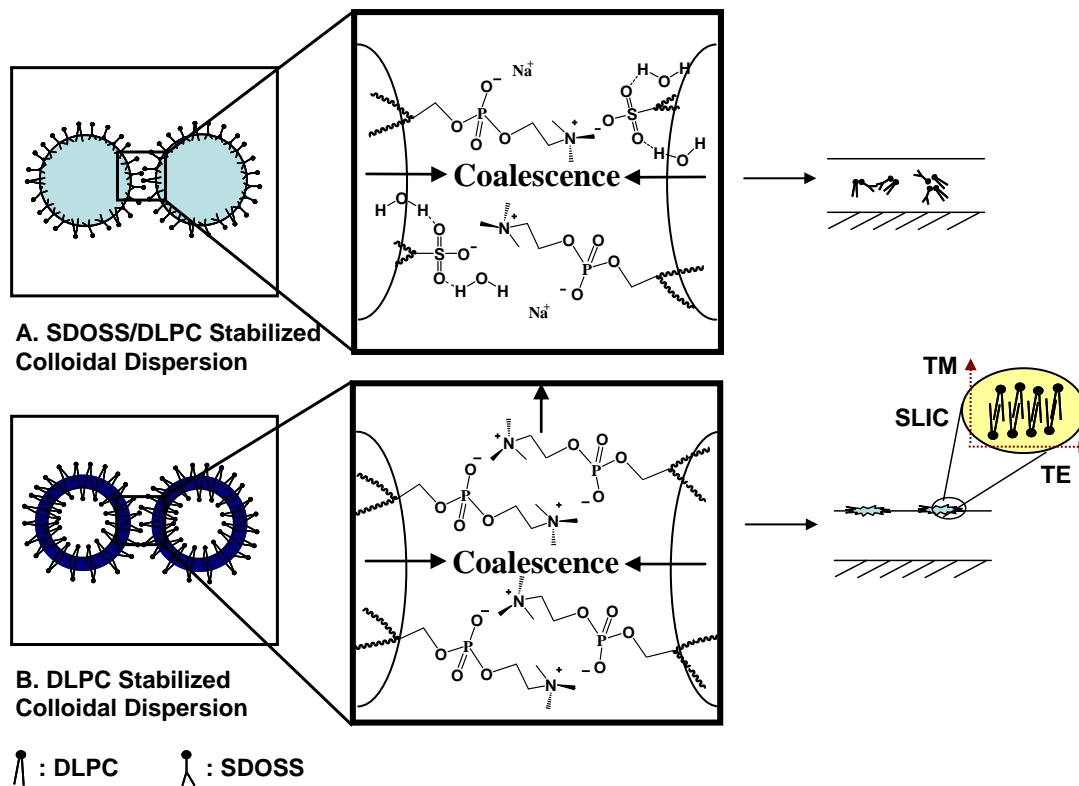


Figure 2.3. Schematic diagram depicting interactions between DLPC and SDOSS.

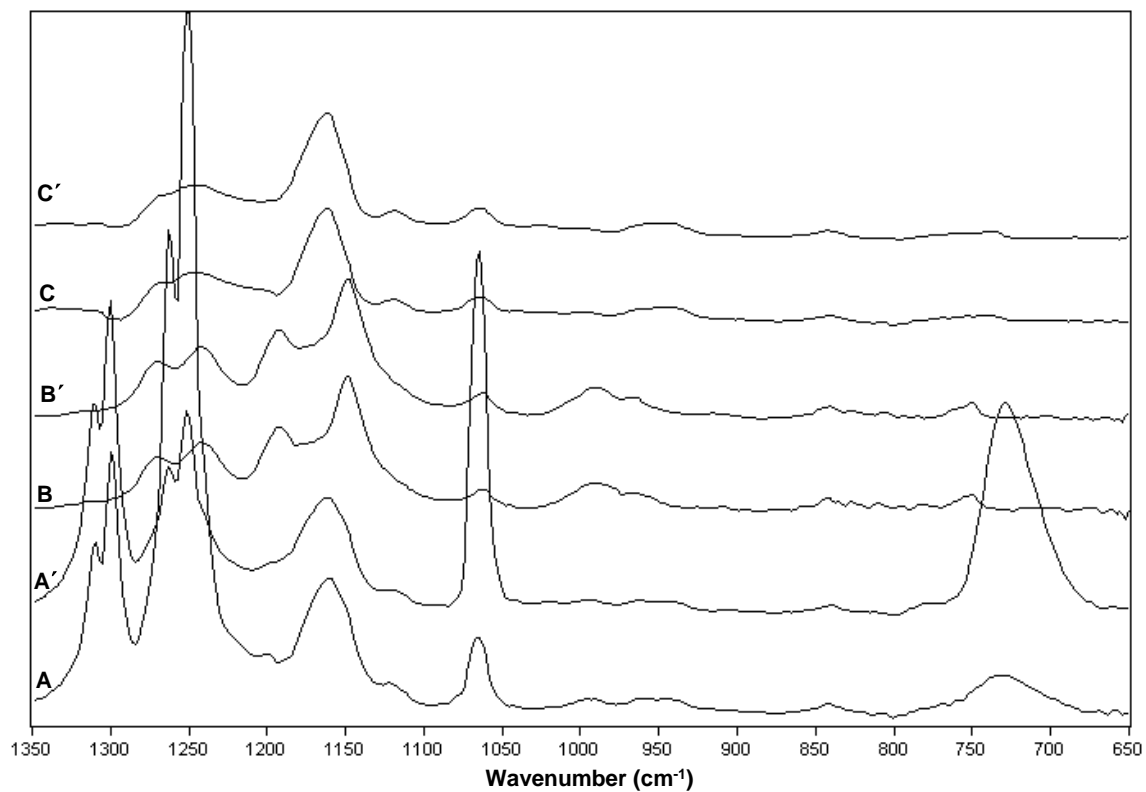


Figure 2.4. ATR-FTIR spectra of DLPC stabilized p-MMA and p-nBA recorded from the F-A interface: (A) p-MMA/p-nBA blend, TE polarization; (A') p-MMA/p-nBA blend, TM polarization; (B) p-MMA, TE polarization; (B') p-MMA, TM polarization; (C) p-nBA, TE polarization; (C') p-nBA, TM polarization.

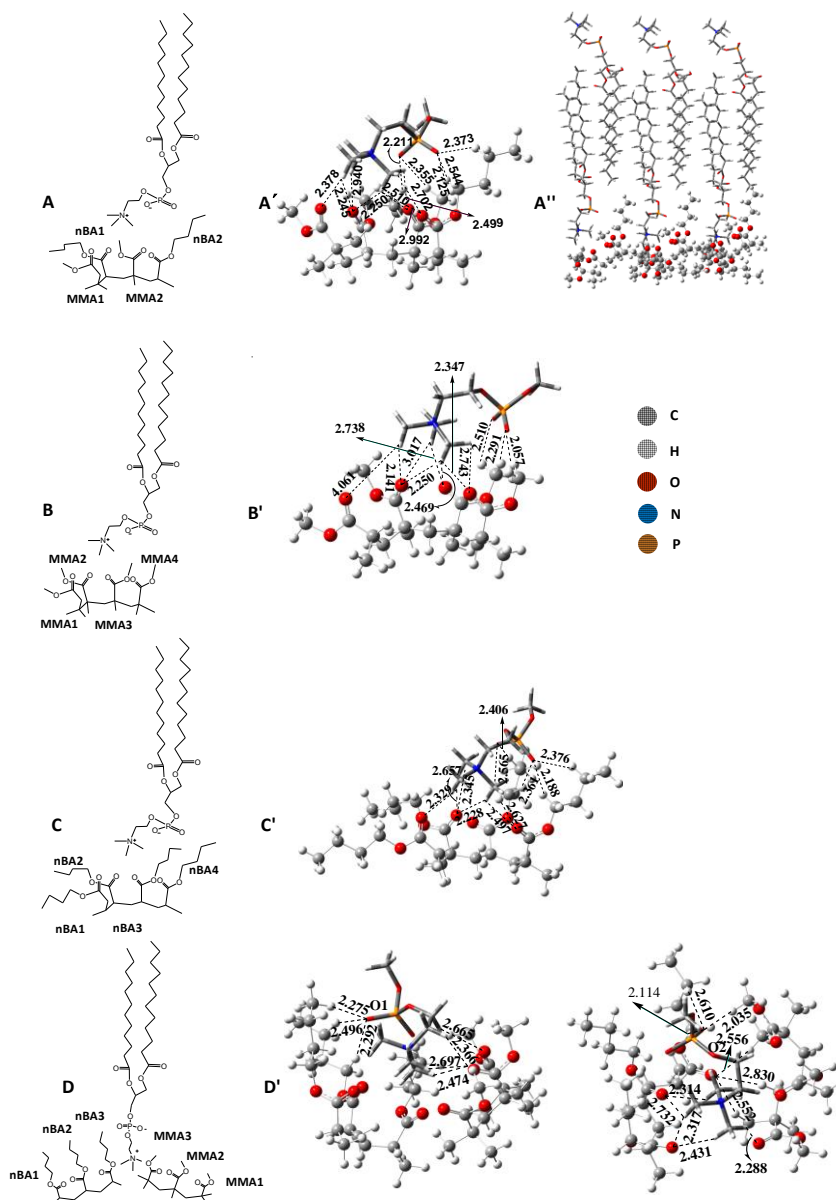


Figure 2.5. Proposed SLIC models resulting from the interaction between copolymer components and DLPC: (A) p-MMA/nBA copolymer; (A') 3D localized p-MMA/nBA copolymer–phospholipid interactions; (A'') 3D model of SLICs; (B) p-MMA homopolymer; (B') 3D localized p-MMA homopolymer–phospholipid interactions; (C) p-nBA homopolymer; (C') 3D localized nBA homopolymer–phospholipid interactions; (D) p-MMA/p-nBA blend; (D') 3D localized p-MMA/p-nBA blend-phospholipid interactions.

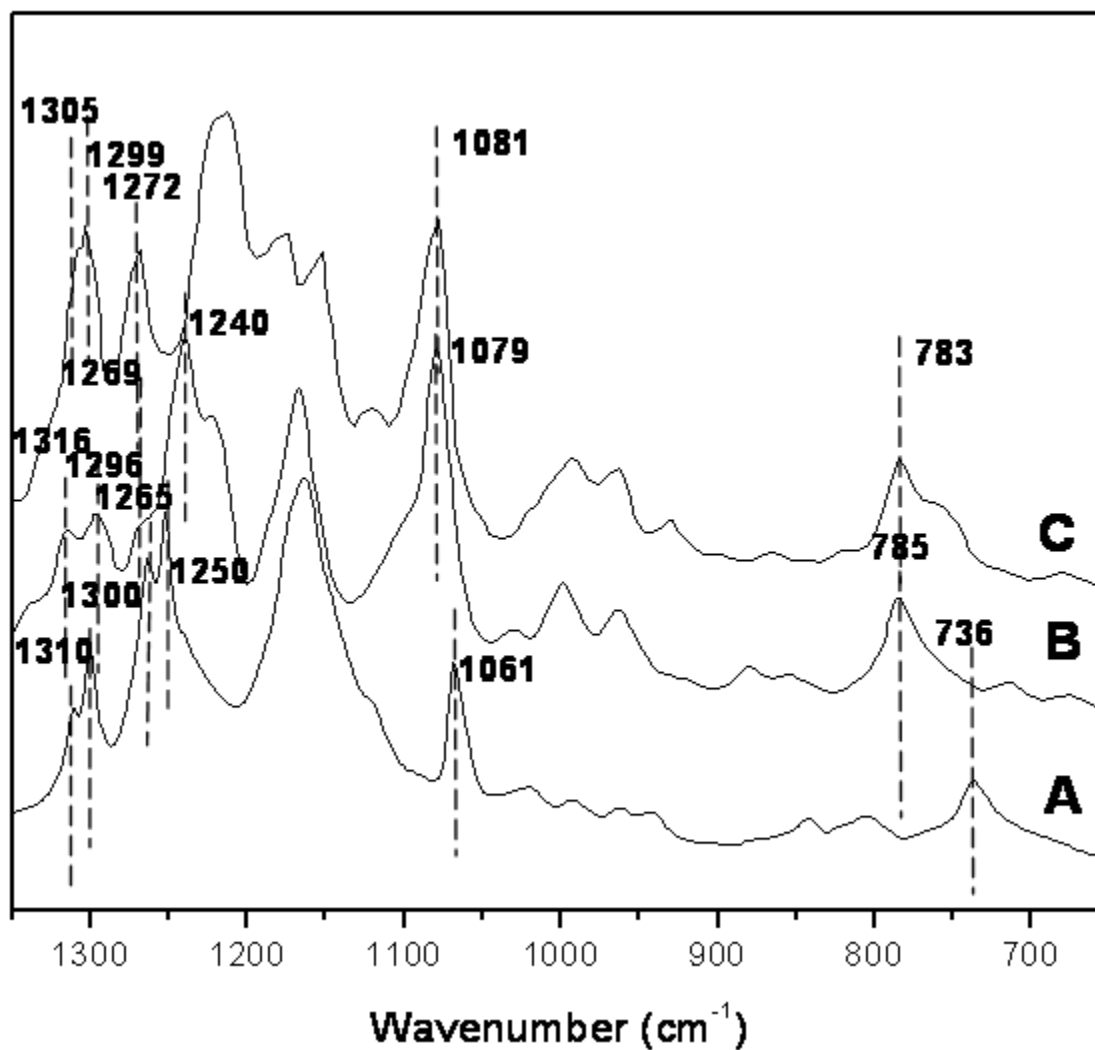


Figure 2.6. Comparison of (A) combined TE and TM polarized ATR-FTIR spectrum of DLPC stabilized p-MMA/nBA collected from the F-A interface; (B) Calculated IR spectrum from the Model A in Figure 2.5, (C) Calculated IR spectrum from the Model D in Figure 2.5.

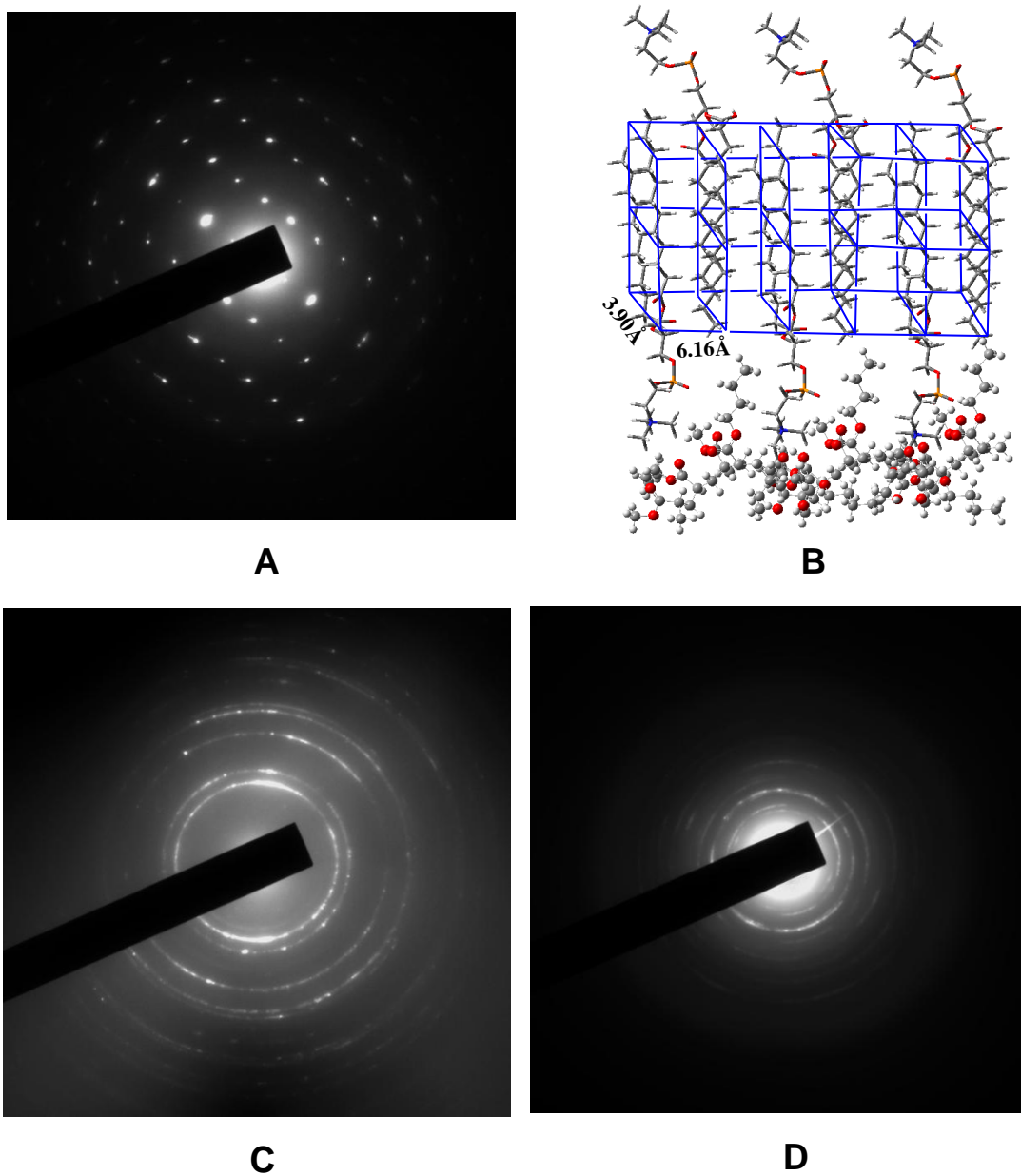


Figure 2.7. Selected area diffraction images of: (A) DLPC; (B) p-MMA/nBA polymer containing SDOSS; (C) p-MMA/nBA containing DLPC; (D) proposed crystal lattice models for SLICs.

References

- (1) Mcmurry, T. J.; Raymond, K. N.; Smith, P. H. *Science* **1989**, *244*, 938.
- (2) Weissbuch, I.; Addadi, L.; Lahav, M.; Leiserowitz, L. *Science* **1991**, *253*, 637.
- (3) Sessler, J. L.; Lawrence, C. M.; Jayawickramarajah, J. *Chem. Soc. Rev.* **2007**, *36*, 314 and references therein.
- (4) Collins, B. E.; Anslyn, E. V. *Chem. Eur. J.* **2007**, *13*, 4700.
- (5) Hannon, M. J. *Chem. Soc. Rev.* **2007**, *36*, 280.
- (6) Chiari, M.; Cretich, M.; Damin, F.; Carlo, G. D.; Oldani, C. *J. Chromatogr. B* **2008**, *866*, 89 and references therein.
- (7) Lestage, D. J.; Schleis, D. J.; Urban, M. W. *Langmuir* **2004**, *20*, 7027.
- (8) Lestage, D. J.; Urban, M. W. *Langmuir* **2005**, *21*, 2150.
- (9) Lestage, D. J.; Yu, M.; Urban, M. W. *Biomacromolecules* **2005**, *6*, 1561.
- (10) Lestage, D. J.; Urban, M. W. *Langmuir* **2005**, *21*, 6753.
- (11) Brown, D. A.; London, E. *J. Biol. Chem.* **2000**, *275*, 11722.
- (12) Simons, K.; van Meer, G. *Biochem.* **1988**, *27*, 6197.
- (13) Urban, M. W. *Attenuated Total Reflectance Spectroscopy of Polymers-Theory and Practice*; American Chemical Society: Washington DC, 1989.
- (14) Bauschlicher, C. W. *Chem. Phys. Lett.* **1995**, *246*, 40.
- (15) El-Azhary, A. A.; Suter, H. U. *J. Phys. Chem.* **1996**, *100*, 15056.
- (16) Becke, A. D. *J. Chem. Phys.* **1993**, *98*, 5648.
- (17) Lee, C.; Yang, W.; Parr, R. *Phys. Rev. B.* **1988**, *37*, 785.
- (18) Miehlisch, B.; Savin, A.; Stoll, H.; Preuss, H. *Chem. Phys. Lett.* **1989**, *90*, 5622.

- (19) Stephens, P. J.; Devlin, F. J.; Chabalowski, C. F.; Frisch, M. J. *J. Phys. Chem.* **1994**, *98*, 11623.
- (20) Roothan, C. C. *J. Rev. Mod. Phys.* **1951**, *23*, 69.
- (21) Pople J. A. ; Nesbet, R. K. *J. Chem. Phys.* **1954**, *22*, 571.
- (22) R., M.; Dierksen, G. *J. Chem. Phys.* **1968**, *49*, 4852.
- (23) <http://cccbdb.nist.gov/vibnotes.asp>.
- (24) Scott, A. P.; Radom, L. *J. Phys. Chem.* **1996**, *100*, 16502.
- (25) Gaussian 03, R. C., Frisch, M. J.; Trucks, G. W.; Schlegel, H. B.; Scuseria, G. E.; Robb, M. A.; Cheeseman, J. R.; Montgomery, Jr., J. A.; Vreven, T.; Kudin, K. N.; Burant, J. C.; Millam, J. M.; Iyengar, S. S.; Tomasi, J.; Barone, V.; Mennucci, B.; Cossi, M.; Scalmani, G.; Rega, N.; Petersson, G. A.; Nakatsuji, H.; Hada, M.; Ehara, M.; Toyota, K.; Fukuda, R.; Hasegawa, J.; Ishida, M.; Nakajima, T.; Honda, Y.; Kitao, O.; Nakai, H.; Klene, M.; Li, X.; Knox, J. E.; Hratchian, H. P.; Cross, J. B.; Bakken, V.; Adamo, C.; Jaramillo, J.; Gomperts, R.; Stratmann, R. E.; Yazyev, O.; Austin, A. J.; Cammi, R.; Pomelli, C.; Ochterski, J. W.; Ayala, P. Y.; Morokuma, K.; Voth, G. A.; Salvador, P.; Dannenberg, J. J.; Zakrzewski, V. G.; Dapprich, S.; Daniels, A. D.; Strain, M. C.; Farkas, O.; Malick, D. K.; Rabuck, A. D.; Raghavachari, K.; Foresman, J. B.; Ortiz, J. V.; Cui, Q.; Baboul, A. G.; Clifford, S.; Cioslowski, J.; Stefanov, B. B.; Liu, G.; Liashenko, A.; Piskorz, P.; Komaromi, I.; Martin, R. L.; Fox, D. J.; Keith, T.; Al-Laham, M. A.; Peng, C. Y.; Nanayakkara, A.; Challacombe, M.; Gill, P. M. W.; Johnson, B.; Chen, W.; Wong, M. W.; Gonzalez, C.; Pople, J. A. Gaussian, Inc., Wallingford CT, 2004.
- (26) Brown, G. L. *J. Polym. Sci* **1956**, *22*, 423.
- (27) Zhao, Y.-Q.; Urban, M. W. *Macromolecules* **2000**, *33*, 7573.

CHAPTER III
STIMULI-RESPONSIVE STRATIFICATION OF PHOSPHOLIPIDS ACROSS
P-MMA/NBA FILMS CONTROLLED BY SYNERGISTIC EFFECTS OF PH,
IONIC STRENGTH AND ENZYME LEVELS

Introduction

Although utilization of colloidal dispersions has been known for many years,¹⁻⁷ their ability to facilitate crystallization of self-assembling bioactive phospholipids (PLs) near the film surfaces and interfaces has been only recently observed.^{4,8-10} This stratification phenomenon was achieved using a combination of sodium dioctylsulfosuccinate (SDOSS) and dual-tailed PLs such as 1,2-bis(10,12-tricosadiynoyl)-*sn*-Glycerol-3-Phosphocholine (DC_{8,9}PC),⁸ 1,2-dilauroyl-*sn*-glycerol-3-phosphocholine (DLPC),⁹ 1-myristoyl-2-hydroxy-*sn*-glycerol-3-phosphocholine (MHPC)⁸ and hydrogenated soybean phosphatidylcholine (HSPC),^{4,10} which functioned as stabilizing agents in the emulsion polymerization of p-(methyl methacrylate/n-butyl acrylate) (p-MMA/nBA) copolymer. Such colloidal particles formed non-spherical dispersions as well as stimuli-responsive features. For example, while stable monomodal spherical colloidal particles were obtained in the presence of SDOSS and liposome forming DLPC phospholipids,¹¹ hollow colloidal particles were produced for DLPC stabilized p-MMA/nBA. The presence of DLPC along with SDOSS exhibited stimuli-responsive behaviors during film formation and these stabilizing components can be driven to the film-air (F-A) or film-substrate (F-S) interface. As a result, formation of surface localized ionic clusters (SLICs)^{4,8-10} at the interfaces during coalescence may occur. In response to thermal, ionic, pH, and enzymatic stimuli, during film formation

particles containing SDOSS/DLPC release stabilizing species to the F-S interface at elevated temperature and low ionic strength, or to the F-A interface with higher pH environments and enzymatic degradation of DLPC.¹¹ In view of the previous findings and the importance of understanding molecular level processes governing formation of biologically active surfaces and interfaces, these studies examine the origin of synergistic stimuli-responsive characteristics of PL stabilized p-MMA/nBA dispersions, with the particular focus on synergistic effects of ionic strength, enzyme concentration, and pH changes during and after coalescence of colloidal dispersions.

Experimental

Methyl methacrylate (MMA), *n*-butyl acrylate (nBA), sodium dioctylsulfosuccinate (SDOSS), potassium persulfate (KPS), CaCl₂, phospholipase A₂ (PLA₂) (1,283 units/mg) were purchased from Aldrich Chemical Co. 1,2-dilauroyl-*sn*-glycero-3-phosphocholine (DLPC) was purchased from Avanti Polar Lipids, Inc.

p-MMA/nBA copolymer emulsions stabilized by DLPC and SDOSS/DLPC respectively were synthesized as described elsewhere.⁹ CaCl₂ aqueous solutions were prepared by solubilizing CaCl₂ in DDI water at 6.9, 11.5, 13.8, 23.0, 27.6, and 45.0 mM. These concentrations correspond to CaCl₂/DLPC molar ratios of 0.5:1.0 and 1.0:1.0 in the emulsions prepared with DLPC and SDOSS/DLPC, respectively. 1.0 mg of PLA₂ enzyme (Aldrich) was dissolved in 1.0 mL of the CaCl₂ aqueous solutions. When applicable, each PLA₂/CaCl₂ solution was separately mixed with 1mL of emulsions containing DLPC and SDOSS/DLPC and adjusted to pH of 2.0, 5.0, and 8.0, and for the dispersion containing SDOSS/DLPC partial precipitation of p-MMA/nBA colloidal particles occurs, whereas for the dispersion containing DLPC, colloidal particles fully

precipitated. This behavior is attributed to a partial cleavage of DLPC at C2 position in the presence of PLA₂ to form a single tailed lysophospholipid and lauric acid,^{12,13} thus destabilizing colloidal particles and leading to partial precipitation. The nonprecipitated portions of the dispersions were allowed to coalesce to form uniform films and are subjects of further studies. Such colloidal dispersions were cast onto a poly(tetrafluoroethylene) (PTFE) mold to achieve free-standing colloidal films with an approximate film thickness of 100 μm. The films were allowed to coalesce for 72 h in a controlled environment at 60% relative humidity (RH) and 23 °C. Model studies were conducted in which DLPC, SDOSS, CaCl₂ and PLA₂ were dispersed in DI water.

Optical micrographs of film surfaces were obtained using a Nikon Optiphot biological microscope equipped with cross-polarizers. Polarized attenuated total reflectance Fourier transform infrared (ATR FT-IR) spectra were collected from the film-air (F-A) and film-substrate (F-S) interfaces using a Bio-Rad FTS-6000 FT-IR single-beam spectrometer with 4 cm⁻¹ resolution. The surfaces were analyzed using a 2 mm Ge crystal with a 45 ° angle maintaining constant contact pressure between the crystal and the specimens. The polarization modes of transverse electric (TE - 0 °) and transverse magnetic (TM - 90 °) were employed from which dichroic ratios (DR) were determined and listed in Tables 1 and 2. When DR < 1.0, molecular segments exhibit preferentially perpendicular orientation to the film interface, whereas for DR > 1.0, parallel alignment is anticipated. All spectra were corrected for spectral distortions using software for the Urban-Huang algorithm.¹⁴ Colloidal dispersion particle morphologies were analyzed using a Zeiss EM 109-T transmission electron microscope (TEM) in which colloidal

dispersions were diluted at a 20:1 vol. ratio (DDI H₂O: dispersion) and deposited on Formvar coated copper TEM grids.

Results and Discussion

The combined effects of ionic strength and enzyme on DLPC/SDOSS stabilized p-MMA/nBA colloidal dispersions are of particular interest because if designed properly, these entities will allow controllable mobility to the F-A and F-S interfaces, thus leading to bioactive surfaces and interfaces. Figure 3.1 illustrates optical images of the F-A (subscript 1) and F-S (subscript 2) interfaces of p-MMA/nBA films: A1 and A2-images of p-MMA/nBA films with 0/1.0 CaCl₂/DLPC; B1 and B2-images of p-MMA/nBA films with 0.5/1.0 CaCl₂/DLPC; C1 and C2-images of p-MMA/nBA films with 1.0/1.0 CaCl₂/DLPC. As illustrated in optical micrographs shown in Figure 3.1, A1 and A2, if there is no stimuli, the F-A and F-S interfaces exhibit no differences. However, when Ca²⁺ and PLA₂ are present in colloidal dispersions, CaCl₂/DLPC ratio will dictate the existence of crystalline entities at the interfaces. As seen in Figure 3.1, B1-B2, when a 0.5/1.0 CaCl₂/DLPC ratio is used, only crystalline domains are present at the F-A interface. In contrast, for a 1.0/1.0 CaCl₂/DLPC ratio, both interfaces are decorated with crystalline entities in the presence of PLA₂. In an effort to identify molecular species responsible for the crystalline phase, spectroscopic analysis was performed and Figure 3.2A, Traces A/A' illustrate the F-A interface of SDOSS/DLPC stabilized p-MMA/nBA copolymer films recorded using TE and TM polarization modes. This approach allows us to identify preferable orientation of molecular entities at the F-A interface. When the CaCl₂/DLPC ratio changes in the presence of PLA₂, new bands at 1135, 1123 and 1089 cm⁻¹ are observed, which are attributed to surface localized ionic clusters (SLICs).^{4,8,9}

This is shown in Figure 3.2, Traces B/B' and C/C'. At the same time, enhanced intensity of the 1089 cm^{-1} band due to PO_4^- entities in the TE mode indicates a preferential parallel orientation of PO_4^- , thus DLPC molecules align perpendicularly to this interface. In addition, as shown in Figure 3.2B, Traces C/C', for a 1.0/1.0 CaCl_2 /DLPC ratio, the bands at 1135 , 1123 and 1089 cm^{-1} due to SLICs are suppressed at the F-S interface, as compared to the surfaces containing no Ca^{2+} and PLA_2 (Traces A/A') and 0.5/1.0 CaCl_2 /DLPC in the presence of PLA_2 (Traces B/B').

The combined effects of ionic strength and enzyme on the DLPC stabilized p-MMA/nBA dispersions were analyzed by utilizing 0.5/1.0 and 1.0/1.0 molar ratio CaCl_2 /DLPC solutions in the presence of PLA_2 . In this case, the entire colloidal dispersion precipitated out due to the hydrolysis effect of PLA_2 enhanced in the presence of Ca^{2+} .¹³ At this point the unprecipitated portion of the solution was analyzed in order to determine partitioning of DLPC molecules. Figure 3.3, A1 and B1 illustrates TEM images of solid residues obtained from 0.5/1.0 and 1.0/1.0 CaCl_2 /DLPC solution, respectively. As seen in Figure 3.3, A1 and B1, hydrolyzed phospholipids form aggregates to form branches as well as particles, but when the CaCl_2 /DLPC ratio changes in the presence of PLA_2 , the morphologies are different. As seen in Image B1 for 1.0/1.0 CaCl_2 /DLPC ratio, smaller fraction of aggregates are remained because higher concentration levels of Ca^{2+} result in DLPC precipitating in the latex particles, thus resulting in less DLPC aggregates. Detailed chemical compositional evidence is provided in Figure 3.3, A2 and B2, which illustrate corresponding IRIRI images recorded by turning into the 1089 cm^{-1} band due to the P-O vibrations of DLPC. As seen in Figure 3.3, A2, and B2, similar branched heterogeneous morphologies are observed. Furthermore,

Figure 3.3, A3 and B3 show IR spectra recorded from selected area. As illustrated in Figure 3.3, A3, the band at 1089 cm^{-1} due to the P-O vibrations of DLPC are detected. However, the band at 1735 cm^{-1} resulting from the C=O vibrations of DLPC shows a relatively low intensity, which is likely attributed to hydrolyzed dual tails by PLA₂. The same spectroscopic information was obtained for the specimen containing 1.0/1.0 CaCl₂/DLPC ratios and it shown in Figure 3.3, B3.

Based on these data, Figure 3.4 depicts SLIC formation as a function of concentration levels of Ca²⁺ in the presence of PLA₂ in the SDOSS/DLPC and DLPC stabilized colloidal dispersions. For SDOSS/DLPC stabilized p-MMA/nBA colloidal dispersions, SLICs which appear as crystalline domains form preferentially perpendicular to the F-A interface of the dispersions containing 0.5/1.0 CaCl₂/DLPC as well as the F-A and F-S interfaces of dispersions containing 1.0/1.0 CaCl₂/DLPC in the presence of PLA₂. In contrast, for DLPC stabilized p-MMA/nBA colloidal dispersions, excessive coagulation occurs and DLPC remains in the solution.

The activity of PLA₂ is strongly dependent upon pH. The pH of the initial colloidal dispersions was 3.0. pH values of colloidal dispersions were adjusted to 2.0, 5.0, and 8.0 before addition of Ca²⁺ and PLA₂, and results of spectroscopic analysis of the dispersions containing 0.5/1.0 CaCl₂/DLPC in the presence of PLA₂ are illustrated in Figure 3.5. As shown in Figure 3.5A (F-A), Traces A/A', at pH=2.0, the bands at 1135, 1123 and 1089 cm^{-1} are observed, which are attributed to SLICs formation. Also, the enhanced intensity of the 1089 cm^{-1} band due to PO₄⁻ entities in the TE mode indicates a preferential perpendicular orientation of DLPC molecules at the F-A interface. However, when pH changes to 5 and 8, these bands are not detected (Traces B/B' and C/C').

Furthermore, as shown in Figure 3.5B (F-S), Traces A-A', at pH=2.0, spectroscopic analysis of the F-S interface shows the presence of SLICs manifested by the bands at 1135, 1123 and 1089 cm^{-1} . However, the bands at 1135, 1123, 1100 cm^{-1} are detected, as shown in Traces B/B' and C/C' (pH=5.0 and 8.0). The dichroic ratio (R) values of the bands at 1089 and 1100 cm^{-1} are approximately R=1.0, indicating random orientation of DLPC molecules. Similar spectroscopic analysis was obtained when utilizing 1.0/1.0 CaCl_2 /DLPC in the presence of PLA_2 at various pHs, which is illustrated in Figure 3.6. In summary, pH changes significantly affect mobility of DLPC to the F-A and F-S interfaces.

The dispersions containing only DLPC containing Ca^{2+} and PLA_2 at various pH values showed different significantly responsiveness. For dispersions containing 0.5/1.0 and 1.0/1.0 CaCl_2 /DLPC in the presence of PLA_2 , at pH = 2.0 and 5.0, the entire dispersion precipitated out, but at pH=8.0, the dispersions remain stable. In the presence of Ca^{2+} , PLA_2 has lower hydrolysis activity at higher pHs and DLPC molecules are more sensitive to PLA_2 and Ca^{2+} than the presence of SDOSS and DLPC together. Figure 3.7, A and B, illustrates analysis of the F-A and F-S interfaces of p-MMA/nBA containing DLPC in the presence of Ca^{2+} and PLA_2 at pH = 8.0. As shown in Figure 3.7A, Traces A/A', the presence of SLICs at the F-A interface of the dispersions containing no Ca^{2+} and PLA_2 is observed, which is manifested by the bands at 1310, 1300, and 1265 cm^{-1} . However, these bands are not detected on the surfaces of films containing Ca^{2+} and PLA_2 at pH=8.0, (Traces B/B' and C/C'). Furthermore, spectroscopic analysis of the F-S interface of the dispersions containing no Ca^{2+} and PLA_2 is illustrated in Figure 3.7B, Traces A/A', and shows that the presence of SLICs is not observed. However, as shown

in Figure 3.7B, Traces B/B', the band at 1100 cm^{-1} with significant intensity increases at the F-S interface of the dispersions containing 0.5/1.0 $\text{CaCl}_2/\text{DLPC}$ in the presence of PLA_2 at $\text{pH} = 8.0$ is observed. For dispersions containing 1.0/1.0 $\text{CaCl}_2/\text{DLPC}$, the bands at 1310 , 1300 , and 1265 cm^{-1} are detected, which are again due to SLICs. As shown in Figure 3.7A, Traces A/A', and Figure 3.7B, Traces C/C', the enhanced intensity of the bands at 1061 cm^{-1} due to P-O-C entities in the TE mode indicates a preferential perpendicular orientation DLPC molecules to the interface.

The proposed mechanisms depicting molecular-level interactions in the p-MMA/nBA colloidal dispersion containing SDOSS/DLPC and DLPC stabilizing agents are illustrated in Figure 3.8. In the presence of the PLA_2 , DLPC are hydrolyzed to a single tailed lysophospholipid and lauric acid, which is enhanced by the presence of Ca^{2+} . For p-MMA/nBA dispersions stabilized with $\text{CaCl}_2/\text{DLPC}$ at 0.5/1.0 and 1.0/1.0 SDOSS/DLPC ratios, the presence of strong ionic interactions between Ca^{2+} , anionic SO_3^- of SDOSS, PO_4^- and $\text{N}(\text{CH}_3)^+$ groups of DLPC lead to ionic aggregates forming SLICs at both film interfaces. For DLPC dispersions, after the addition of PLA_2 and Ca^{2+} , DLPC molecules with single tails are unable to stabilize hollow particles and phosphocholine groups of DLPC interact with Ca^{2+} leading to the removal of DLPC around the particles.

Based on the spectroscopic analysis of SDOSS/DLPC and DLPC stabilized MMA/nBA colloidal dispersion in the presence of Ca^{2+} , PLA_2 and pH , the following physic-chemical phenomenon resulting from combined effects of ionic strength, enzyme and pH are depicted, which is illustrated in Figure 3.9. For SDOSS/DLPC stabilized colloidal dispersions containing 0.5/1.0 $\text{CaCl}_2/\text{DLPC}$ and PLA_2 , at $\text{pH}=2.0$, SLIC are

preferentially perpendicular to the F-A and F-S interfaces, whereas at pH=5.0 and 8.8, SLICs are randomly orientated at the F-S interface. The same results were obtained for dispersions containing 1.0/1.0 CaCl₂/DLPC. In contrast, for DLPC stabilized particles containing 0.5/1.0 and 1.0/1.0 CaCl₂/DLPC in the presence of PLA₂ at pH=8.0, SLICs revealed preferentially perpendicular orientation to the F-S interface. These results illustrate synergistic effects of ionic strength, pH, and enzyme, thus providing means for controlled stratification of stabilizing species during film formation.

Conclusions

In the presence of ionic species and biologically active enzymes, DLPC stabilized colloidal dispersions are highly sensitive to the enzymatic hydrolysis which is strengthened by Ca²⁺, and SLICs are observed in the F-A interfaces of colloidal particles containing SDOSS/DLPC. As biologically active dispersing agents are sensitive to pH changes, the synergistic effects of ionic strength, pH, and enzyme result in controlled stratification during film formation.

Table 3.1. Dichroic Ratios of Selected IR Bands^a of SDOSS/DLPC stabilized p-MMA/nBA colloidal dispersions.

^a $R = A_{\parallel} / A_{\perp}$, where A_{\parallel} and A_{\perp} are band areas for parallel (TE) and perpendicular (TM) polarizations. R values were obtained by ratioing the baseline corrected IR bands of interest. For each band, the same wavenumber range was used to determine the band area for TE and TM polarizations.

CaCl ₂ /DLPC	Interface	pH	$\overline{\text{PO}_4^-}$ 1089cm ⁻¹	$\overline{\text{P-O-C}}$ 1061cm ⁻¹
0.0/1.0	F-A	3	n/a	0.890
	F-S	3	n/a	0.482
0.5/1.0	F-A	3	4.555	0.398
	F-S	3	2.260	0.436
1.0/1.0	F-A	3	1.757	0.297
	F-S	3	2.640	0.317
0.5/1.0	F-A	2	1.648	0.398
		5	n/a	0.501
		8	n/a	0.440
	F-S	2	2.760	0.464
		5	n/a	0.903
		8	n/a	0.511
1.0/1.0	F-A	2	1.624	0.472
		5	n/a	0.509
		8	n/a	0.570
	F-S	2	1.735	0.289
		5	n/a	0.431
		8	n/a	3.946

Table 3.2. Dichroic Ratios of Selected IR Bands^b of DLPC stabilized p-MMA/nBA colloidal dispersions.

^b $R = A_{\parallel} / A_{\perp}$, where A_{\parallel} and A_{\perp} are band areas for parallel (TE) and perpendicular (TM) polarizations. R values were obtained by ratioing the baseline corrected IR bands of interest. For each band, the same wavenumber range was used to determine the band area for TE and TM polarizations.

CaCl ₂ /DLPC	Interface	pH	<u>SLIC</u> 1310cm ⁻¹	<u>SLIC</u> 1300cm ⁻¹	<u>SLIC</u> 1265cm ⁻¹	<u>P=O</u> 1250cm ⁻¹	<u>PO₄⁻</u> 1089cm ⁻¹	<u>P-O-C</u> 1061cm ⁻¹
0/1.0	F-A		0.933	1.404	0.862	4.639	n/a	0.235
	F-S		n/a	n/a	n/a	n/a	n/a	0.525
0.5/1.0	F-A	8	n/a	n/a	n/a	n/a	n/a	0.422
	F-S	8	n/a	n/a	n/a	n/a	n/a	0.420
1.0/1.0	F-A	8	n/a	n/a	n/a	n/a	n/a	0.487
	F-S	8	0.939	1.575	0.672	1.172	n/a	n/a

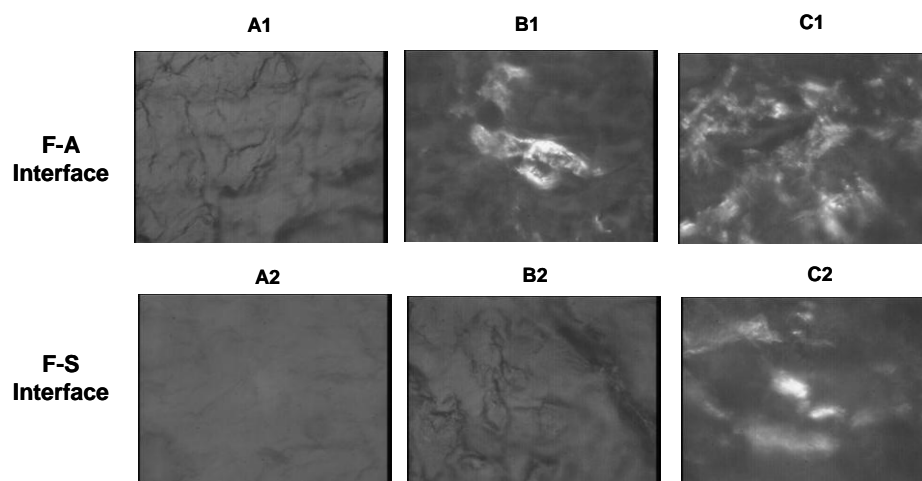


Figure 3.1. Cross-polarized optical micrographs of SDOSS/DLPC stabilized p-MMA/nBA films recorded from F-A and F-S interfaces at (A1) F-A; (A2) F-S; (B1) F-A, 0.5/1.0 CaCl_2 /DLPC, PLA_2 ; (B2) F-S, 0.5/1.0 CaCl_2 /DLPC, PLA_2 ; (C1) F-A, 1.0/1.0 CaCl_2 /DLPC, PLA_2 ; (C2) F-S, 1.0/1.0 CaCl_2 /DLPC, PLA_2 .

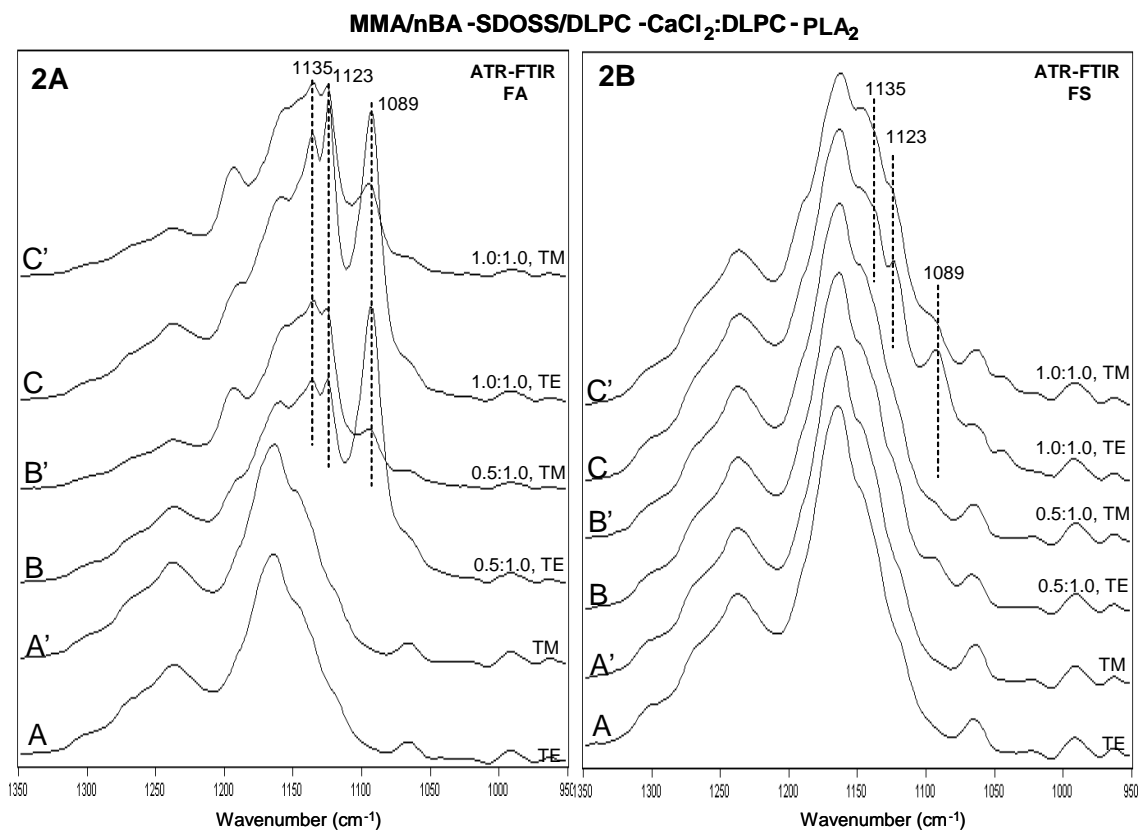


Figure 3.2. Polarized ATR-FTIR spectra at F-A interface (2A) and F-S interface (2B) of p-MMA/nBA copolymer films containing SDOSS/DLPC: (A) TE; (A') TM, and colloidal dispersions treated with CaCl₂/DLPC molar ratios: (B) 0.5/1.0, TE; (B') 0.5/1.0, TM; (C) 1.0/1.0, TE; (C') 1.0/1.0, TM in the presence of PLA₂.

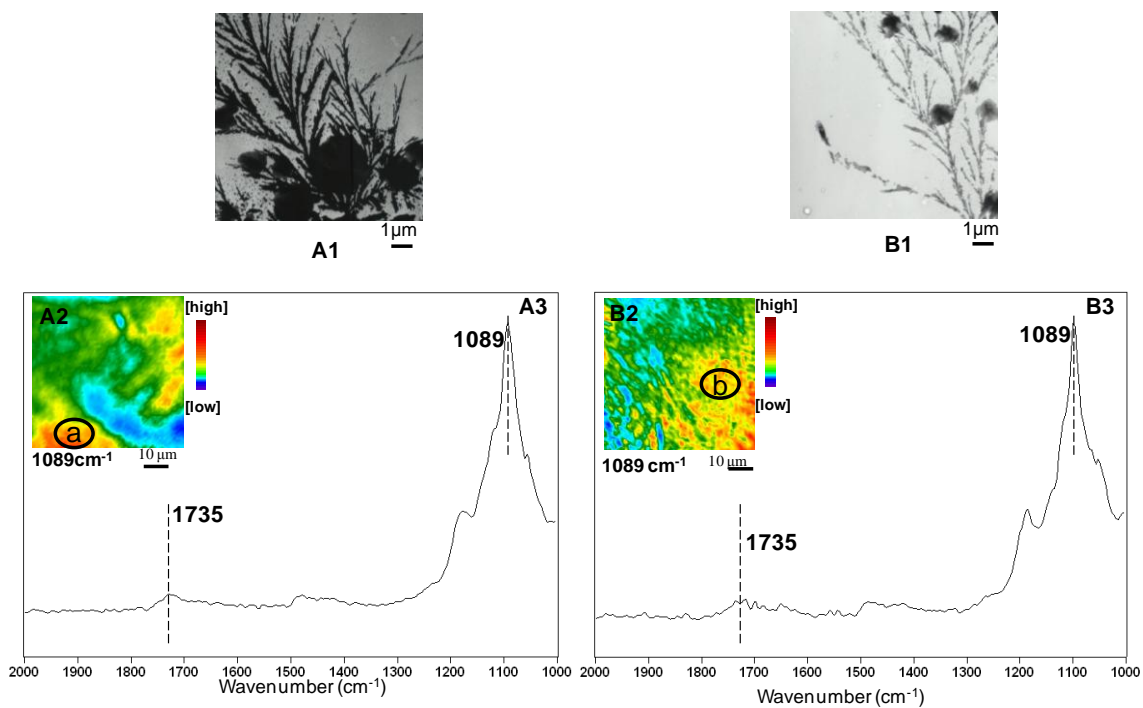


Figure 3.3. Analysis of colloidal residue of p-MMA/nBA dispersions containing DLPC treated with $\text{CaCl}_2/\text{DLPC}$ molar ratios: (A) 0.5/1.0 $\text{CaCl}_2/\text{DLPC}$; (B) 1.0/1.0 $\text{CaCl}_2/\text{DLPC}$ in the presence of PLA_2 including TEM images (A1) and (B1), IRIRI images (A2) and (B2), and IR spectra (A3) and (B3).

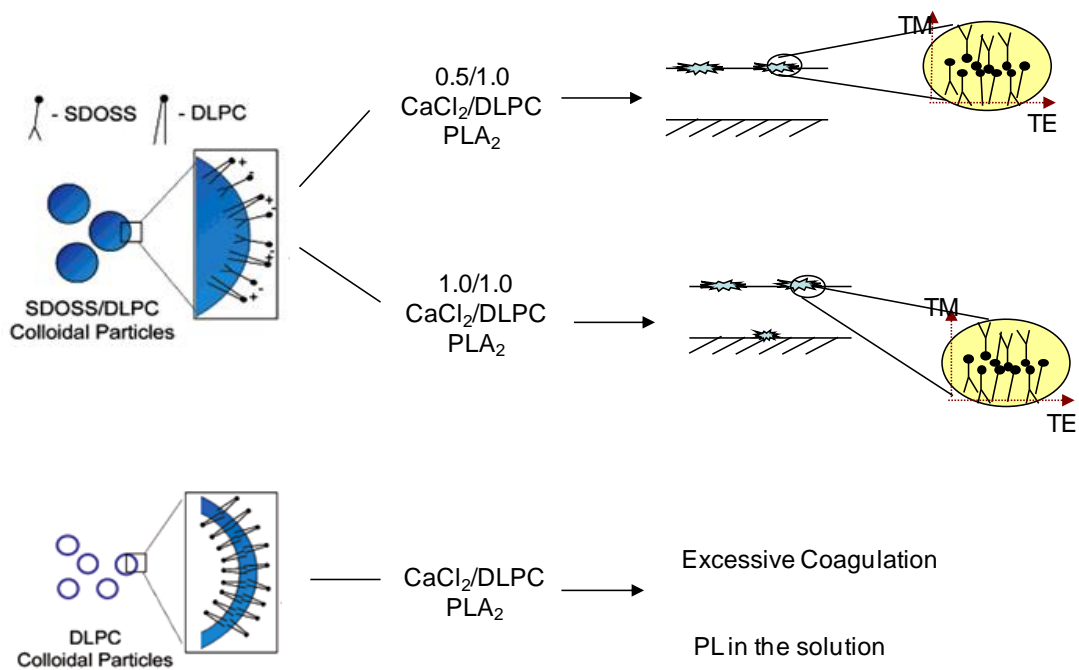


Figure 3.4. Schematic diagram depicting preferentially oriented manifestations at the F-A and F-S interfaces of SDOSS/DLPC and DLPC stabilized p-MMA/nBA copolymer prepared in the presence of $\text{CaCl}_2/\text{DLPC}$ molar ratios and PLA_2 .

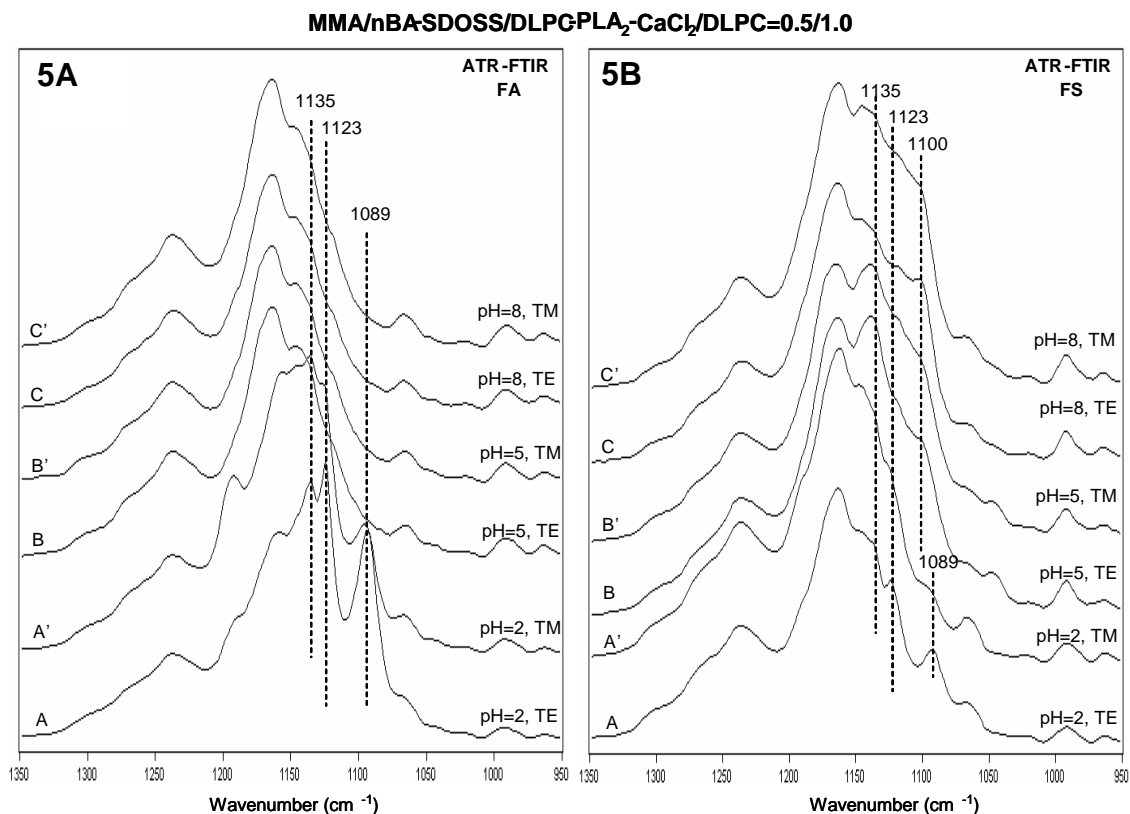


Figure 3.5. A. Polarized ATR-FTIR spectra at F-A interface of p-MMA/nBA copolymer films containing SDOSS/DLPC treated with PLA₂ and 0.5/1.0 CaCl₂/DLPC and adjusted to pH: (A) 2.0, TE; (A') 2.0, TM (B) 5.0, TE; (B')5.0, TM; (C)8.0, TE; (C') 8.0, TM.

Figure 3.5.B. Polarized ATR-FTIR spectra at F-S interface of p-MMA/nBA copolymer films containing SDOSS/DLPC treated with PLA₂ and 0.5/1.0 CaCl₂/DLPC and adjusted to pH: (A) 2.0, TE; (A') 2.0, TM (B) 5.0, TE; (B')5.0, TM; (C)8.0, TE; (C') 8.0, TM.

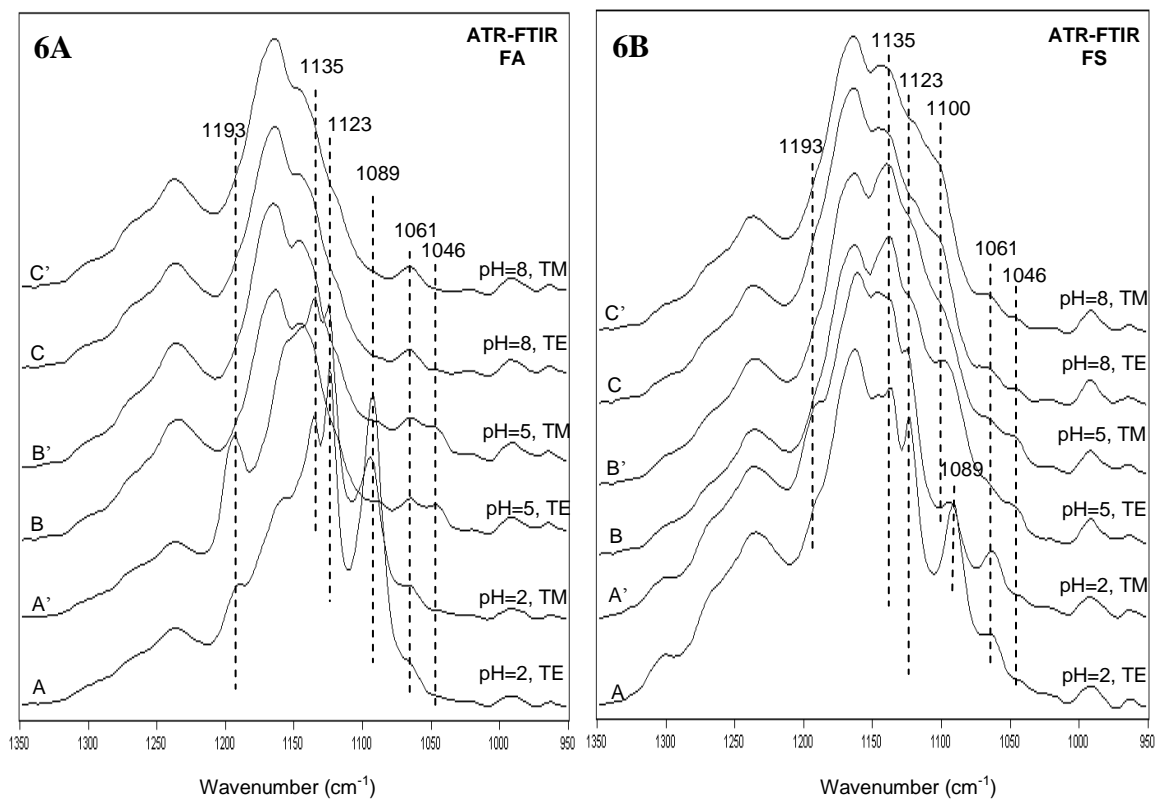
MMA/nBA-SDOSS/DLPC-PLA₂-CaCl₂/DLPC=1.0/1.0

Figure 3.6.A. Polarized ATR-FTIR spectra at F-A interface of p-MMA/nBA copolymer films containing SDOSS/DLPC treated with PLA₂ and 1.0/1.0 CaCl₂/DLPC and adjusted to pH: (A) 2.0, TE; (A') 2.0, TM (B) 5.0, TE; (B') 5.0, TM; (C) 8.0, TE; (C') 8.0, TM.

Figure 3.6.B. Polarized ATR-FTIR spectra at F-S interface of p-MMA/nBA copolymer films containing SDOSS/DLPC treated with PLA₂ and 1.0/1.0 CaCl₂/DLPC and adjusted to pH: (A) 2.0, TE; (A') 2.0, TM (B) 5.0, TE; (B') 5.0, TM; (C) 8.0, TE; (C') 8.0, TM.

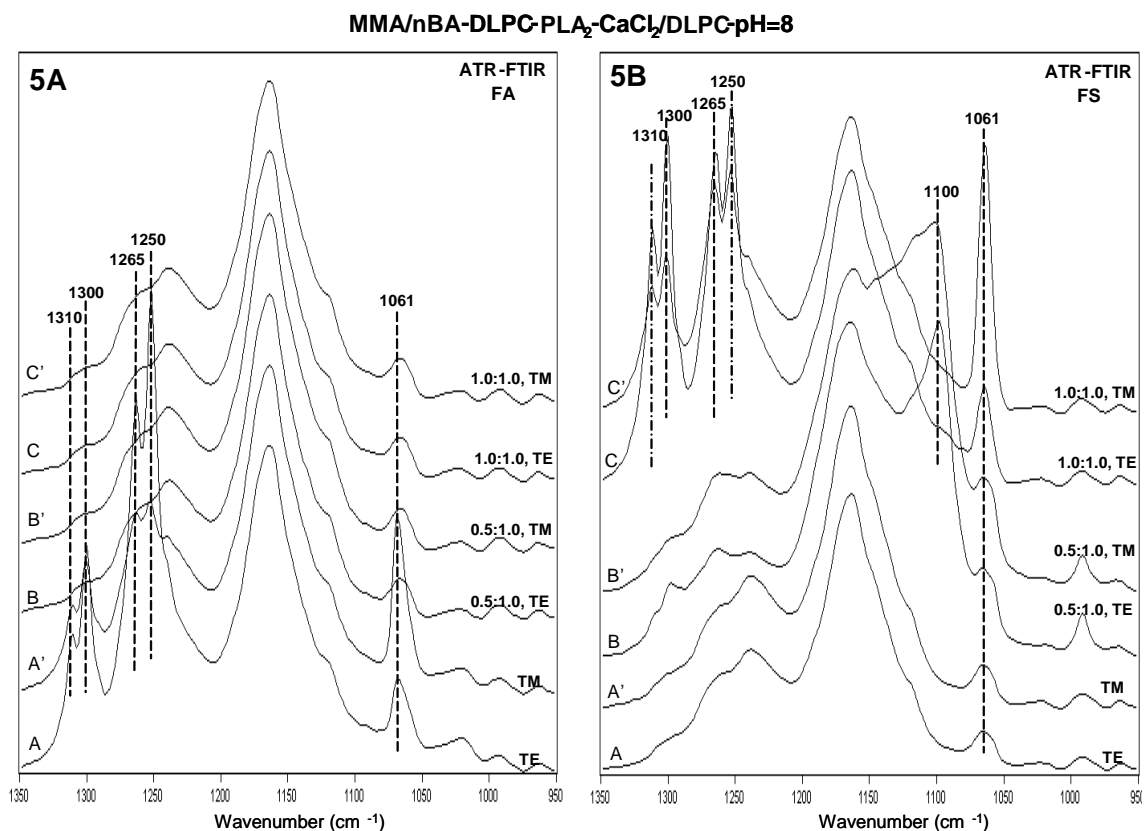


Figure 3.7.A. Polarized ATR-FTIR spectra at F-A interface of DLPC stabilized p-MMA/nBA copolymer films (A) TE; (A') TM, and treated with PLA₂ and various ratios of CaCl₂/DLPC and adjusted to pH 8: (B) 0.5/1.0 CaCl₂/DLPC, TE; (B') 0.5/1.0 CaCl₂/DLPC, TM; (C) 1.0/1.0 CaCl₂/DLPC, TE; (C') 1.0/1.0 CaCl₂/DLPC, TM.

3.7.B. Polarized ATR-FTIR spectra at F-S interface of DLPC stabilized p-MMA/nBA copolymer films (A) TE; (A') TM, and treated with PLA₂ and various ratios of CaCl₂/DLPC and adjusted to pH 8: (B) 0.5/1.0 CaCl₂/DLPC, TE; (B') 0.5/1.0 CaCl₂/DLPC, TM; (C) 1.0/1.0 CaCl₂/DLPC, TE; (C') 1.0/1.0 CaCl₂/DLPC, TM.

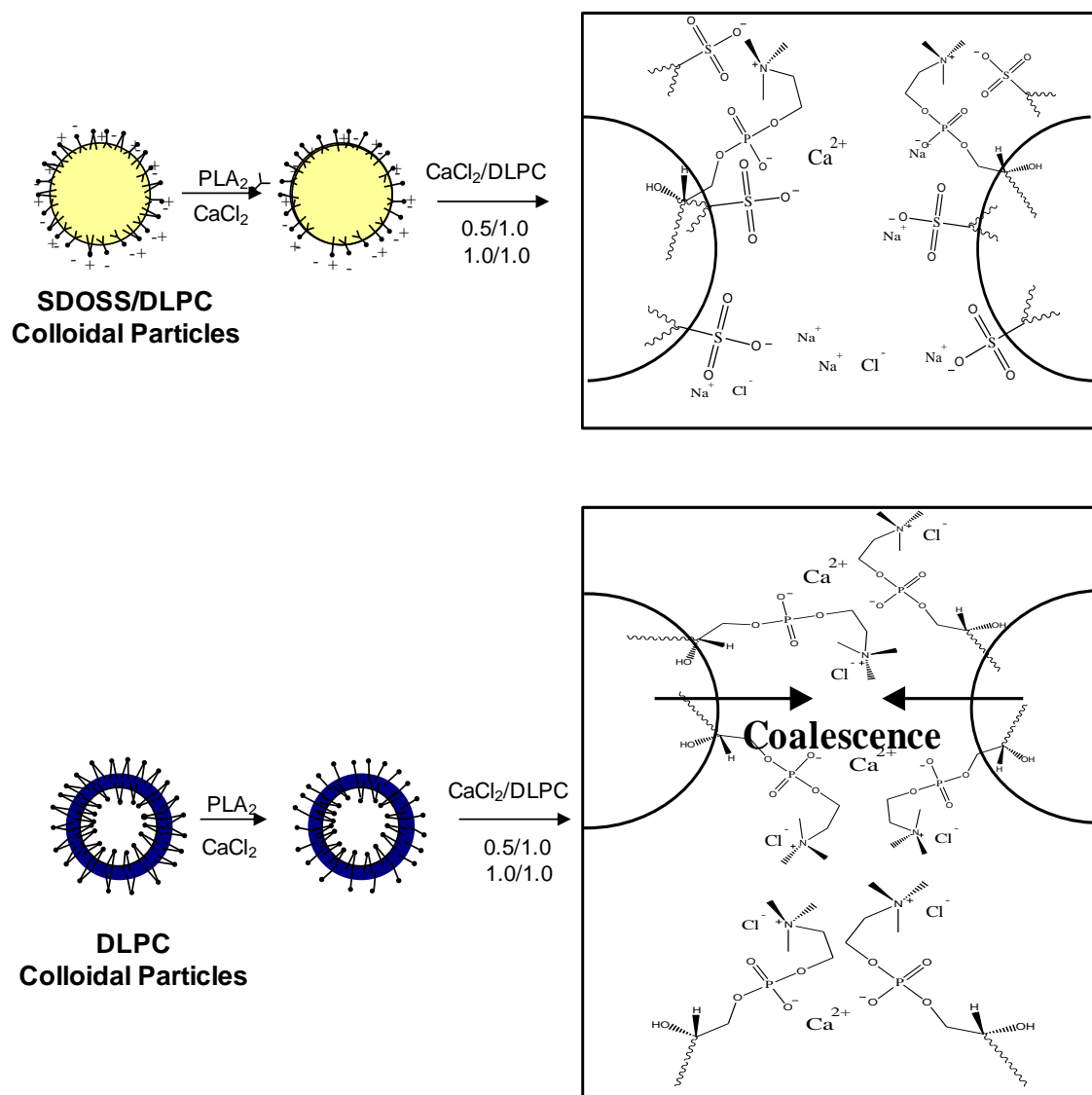


Figure 3.8. Schematic diagram depicting molecular-level interactions between SDOSS and DLPC species in the presence of Ca²⁺ and PLA₂.

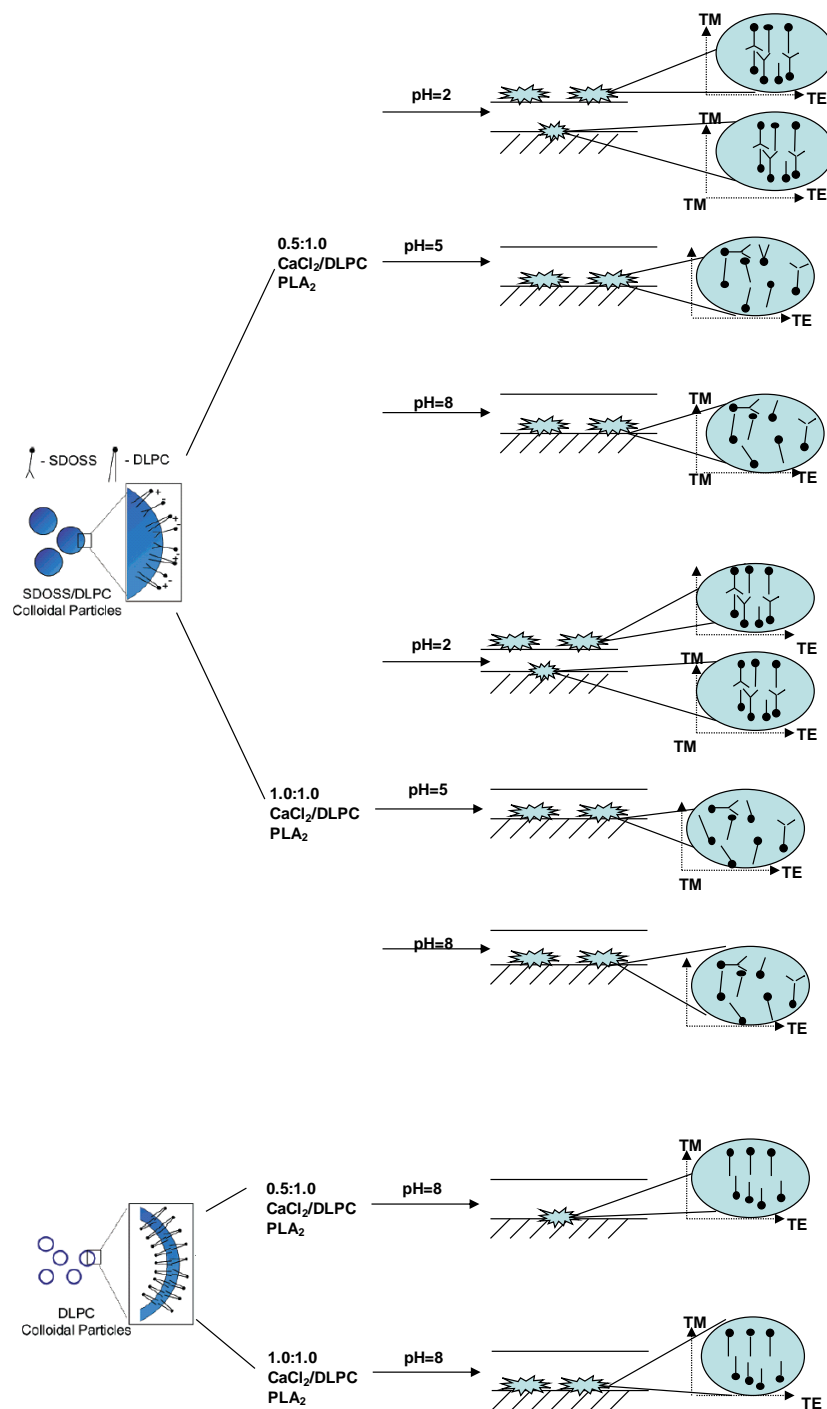


Figure 3.9. Schematic diagram depicting preferentially oriented manifestations at the F-A and F-S interfaces of SDOSS/DLPC stabilized dispersions and DLPC stabilized dispersions treated with various ratios of CaCl₂/DLPC and PLA₂ and adjusted to various pH.

References

- (1) Dreher, W. R.; Urban, M. W. *Langmuir* **2003**, *19*, 10254.
- (2) Dreher, W. R.; Zhang, P.; Urban, M. W.; Porzio, R. S.; Zhao, C. *Macromolecules* **2003**, *36*, 1228.
- (3) Zhao, Y.-Q.; Urban, M. W. *Macromolecules* **2000**, *33*, 7573.
- (4) Lestage, D. J.; Schleis, D. J.; Urban, M. W. *Langmuir* **2004**, *20*, 7027.
- (5) Davis, S. D.; Hadgraft, J.; Palin, K. J. *Encyclopedia of Emulsion Technology* New York, 1985; Vol. 2.
- (6) Winnik, M. A.; Feng, J. J. *Coat. Technol.* **1996**, *68*, 39.
- (7) Beltran, C. M.; Guillot, S.; Langevin, D. *Macromolecules* **2003**, *36*, 8506.
- (8) Lestage, D. J.; Urban, M. W. *Langmuir* **2005**, *21*, 2150.
- (9) Lestage, D. J.; Yu, M.; Urban, M. W. *Biomacromolecules* **2005**, *6*, 1561.
- (10) Yacoub, A.; Urban, M. W. *Biomacromolecules* **2003**, *4*, 52.
- (11) Lestage, D. J.; Urban, M. W. *Biomacromolecules* **2005**, *6*, 1561.
- (12) Tinker, D. O.; Low, R.; Lucassen, M. *Can. J. Biochem.* **1980**, *58*, 898.
- (13) Verheij, H. M.; Volwerk, J. J.; Jansen, E. H. J. M.; Puyk, W. C.; Dijkstra, B. W.; Drenth, J.; de Haas, G. H. *Biochem.* **1980**, *19*, 743.
- (14) Urban, M. W. *Attenuated Total Reflectance Spectroscopy of Polymers-Theory and Practice*; American Chemical Society: Washington DC, 1989.

CHAPTER IV
CONCENTRIC FERROMAGNETIC NANOTUBES
FROM BIOLOGICALLY ACTIVE PHOSPHOLIPIDS
PART I: SYNTHESIS

Introduction

A quest for unique magnetic nanomaterials continues to be driven by scientific curiosity as well as numerous potential applications ranging from information storage, ferro-fluidics, drug delivery systems, biosensing devices, magnetic resonance imaging, to name just a few. Iron oxides are of particular interest and since shape also contributes to magnetic properties,^{1,2} different shapes of α -Fe₂O₃, including nanorods,^{3,4} nanospheres,^{5,6} nanowires,⁷ and a spindle-type⁸ were prepared. Attempts to make hollow tubular structures^{9,10} have been made because this shape may exhibit unique magnetic properties, but the highest obtained magnetization values were 2.7-2.9 emu/g or smaller.

In this chapter, we report the development of a simple approach that utilizes 1,2-bis(10,12-tricosadiynoyl)-*sn*-glycero-3-phosphocholine (DC_{8,9}PC) phospholipid (PL) which self-assembles in water into unstable nanotubes,¹¹ which upon further redox and thermal reactions form ferromagnetic nanotubes (FMNTs) with exceptionally high magnetization.

Experimental

1,2-bis(10,12-tricosadiynoyl)-*sn*-glycero-3-phosphocholine (DC_{8,9}PC) was purchased from Avanti Polar Lipids, Inc. Ammonium iron (II) sulfate hexhydrate ((NH₄)₂Fe(SO₄)₂·6H₂O), and hydrogen peroxide (H₂O₂) (30 wt. % in water) were purchased from Aldrich Chemical Co. A schematic diagram illustrating the formation of

nanotubes containing inorganic layers is shown in Figure 4.1.1. Initially, DC_{8,9}PC nanotubes were obtained using the literature method.¹¹ 10 mL of an aqueous dispersion with 1.1 mol/L DC_{8,9}PC nanotubes was purged with N₂ for 0.5 hr, followed by the addition of 0.5 mL of 0.4 mol/L ammonium iron (II) sulfate hexhydrate aqueous solution, which served as a reducing agent. After 0.5 hr, the final step involved the addition of 0.2 mmol of hydrogen peroxide, which acted as an oxidizing agent to react with the reducing agent. The reaction continued for 1 hour after which time the product was collected by centrifuging and dialysis to remove excess ions. Due to the presence of Fe³⁺ oxidized from Fe²⁺ by H₂O₂ the final nanotube product exhibited a light yellow color. Finally, nanotubes were freeze dried and annealed at 550 °C for 0.5 hour.

Morphologies of nanotubes were analyzed using a Jeol JEM-2100 transmission electron microscope (TEM) operated at 200 kV, in which samples were diluted and deposited on formvar/carbon coated copper grids. Magnetic hysteresis measurements were performed using a MicroMag Model 2900 alternating gradient magnetometer (AGM, Princeton Measurement Corp.) at room temperature. Raman spectra and images were obtained with a Renishaw inVia Raman microscope equipped with a computer-controlled three-axis encoded (XYZ) motorized stage, a RenCam CCD detector, and a Leica microscope (DMLM series). The 785 nm diode laser provided Raman excitation with a maximum power output of 300 mW. The sample solutions were deposited on the gold surface and allowed to dry overnight. The Raman spectra of samples were collected with a 30 mW laser power on the sample and an acquisition time of 30 sec. Raman images were obtained with the dielectric tunable filter band-pass centered at 1508 cm⁻¹ using an acquisition time of 2 min and a ×100 objective.

Results and Discussion

The formation of FMNT process involves three steps which are illustrated in Figure 4.1.1. As seen, Step 1 involves DC_{8,9}PC self-assembly leading to the formation of PL nanotubes. In Step 2, after addition of (NH₄)₂Fe(SO₄)₂, these ionic species are attached onto the interior and exterior surfaces of DC_{8,9}PC nanotubes. Further addition of H₂O₂ leads to the fast Fe²⁺ → Fe³⁺ oxidization and the formation of the amorphous basic iron (III) sulfate layers on the interior and exterior of DC_{8,9}PC nanotubes. At the same time, HO· radicals generated from redox reactions initiate polymerization of diacetylene groups of DC_{8,9}PC, thus forming an alternating C=C/C≡C conjugated interlayer. As shown in Step 3, further thermal exposure to 550 °C of these materials result in the conversion of amorphous basic iron (III) sulfate to doped iron oxide phase and the formation of crosslinked carbon tubular interlayers.

The process of the nanotube formation was experimentally followed using transmission electron microscopy (TEM) and spectroscopically. Figure 4.1.2 illustrates TEM images of each step described in Figure 4.1.1. As shown by image A, self-assembly of DC_{8,9}PC nanotubes occurs, followed by Step 2 involving reactions of ammonium iron (II) sulfate hexhydrate ((NH₄)₂Fe(SO₄)₂·6H₂O) and crosslinking of diacetylene groups of DC_{8,9}PC in the presence of H₂O₂ oxidizing agent. The resulting nanotube is illustrated in Figure 4.1.2, B. The final third stage that leads to the exceptionally high magnetization involves annealing at 550 °C for 0.5 hour. As shown in Figure 4.1.2, C, concentric nanotubes separated by crosslinked carbon layers are formed. Supplemental section provides spectroscopic and selected area electron diffraction (SAD) data to support these results.

In order to follow chemical changes resulting from Steps 1 and 2, Raman analysis was performed, which is shown in Figure 4.1.3, A and B. Trace A, collected from Step 1, illustrates the Raman spectrum of DC_{8,9}PC nanotubes, which exhibit C≡C stretching vibrations manifested by the band at 2259 cm⁻¹. As shown in Trace B, Raman spectrum recorded after Step 2 exhibits the presence of the band at 1610 cm⁻¹ due to H₂O stretching vibrations, the band at 1021 cm⁻¹ due to SO₄²⁻ stretching vibrations, and the 602 cm⁻¹ band resulting from the Fe-O vibrations. It should be noted that after Step 2 nanotubes contains H₂O, SO₄²⁻, and Fe-O species. Based on the literature data, there are two types of structures which contain these species: iron (III) oxyhydroxy sulfate (Fe₈O₈(OH)_x(SO₄)_y)¹² and amorphous basic iron (III) sulfate (2Fe₂O₃·SO₃·xH₂O).¹³ Since the bands due to -OH vibrations are present in iron (III) oxyhydroxy sulfate, which is absent after Step 2, iron (III) oxyhydroxy sulfate is unlikely to be present. In contrast, amorphous basic iron (III) sulfate prepared from hydrolytic precipitation of the Fe₂(SO₄)₃ solution at pH 5-6 matches our spectroscopic data. Thus, chemical composition after Step 2 is believed to be amorphous basic iron (III) sulfate.¹³ As seen in Trace B (Step 2), the band at 2259 cm⁻¹ due to C≡C stretching vibrations exhibits lower intensity, and new bands detected at 2109 cm⁻¹ and 1508 cm⁻¹ are due to C≡C and C=C stretching vibrations of polymerized interlayer structures, respectively.¹⁴ The latter result from polymerization of diacetylenic groups of DC_{8,9}PC which is initiated by the radicals generated by Fe²⁺/H₂O₂ redox reactions, and the formation of alternating C≡C and C=C conjugated structures. The detailed Raman analysis of nanotubes recorded from Step 3 will be discussed in Part II.

In an attempt to combine morphological and chemical information, an optical microscopic image (insert C of Figure 4.1.3) and Raman imaging of a nanotube after Step 2 (insert D of Figure 4.1.3) are shown. While the optical image manifests the tubular morphology, Raman image of the same nanotube was collected by tuning into the C=C band at 1508 cm^{-1} . Again, tubular morphology is clearly observed, where green area represents the 1508 cm^{-1} band intensity.

Magnetic properties of the nanotubes are illustrated in Figure 4.1.4, A and B, respectively. As seen in Figure 4.1.4, A, after Step 2 nanotubes are paramagnetic. After Step 4, the hysteresis loop (M - H curve) of FMNTs with exceptionally high magnetization at room temperature is observed (Figure 4.1.4, B). The remanent magnetization (M_r), the saturation magnetization (M_s), the squareness (M_r/M_s), and the coercivity (H_c) values are 4.62 emu/g, 46.12 emu/g, 0.1002 and 51.35 Oe, respectively. These data also show that magnetic properties of FMNTs are significantly enhanced compared to those reported for chemically similar particles and rods, which is likely attributed to the formation of anion or cation-doped iron oxide phases altering localized oxidation state of Fe, thus resulting in exceptionally high magnetization values. Concentric doped iron oxide nanotubes separated by a carbon layer which may also influence magnetization.

Conclusions

In summary, DC_{8,9}PC phospholipid nanotubes were polymerized in the presence of Fe²⁺/H₂O₂ redox agents, which resulted in amorphous basic iron (III) sulfate concentric nanotubes separated by crosslinked PL layers. Further exposure of the nanotubes to 550 °C resulted in the formation of ferromagnetic iron oxide concentric nanotubes separated by carbon sheet interlayers with the remanent magnetization (M_r) of

4.62 emu/g, the saturation magnetization (M_s) of 46.12 emu/g, the squareness (M_r/M_s) of 0.1002, and the coercivity (H_c) of 51.35 Oe. To the best of our knowledge this is the first study illustrating that using biologically active phospholipids highly ferromagnetic nanotubes can be produced.

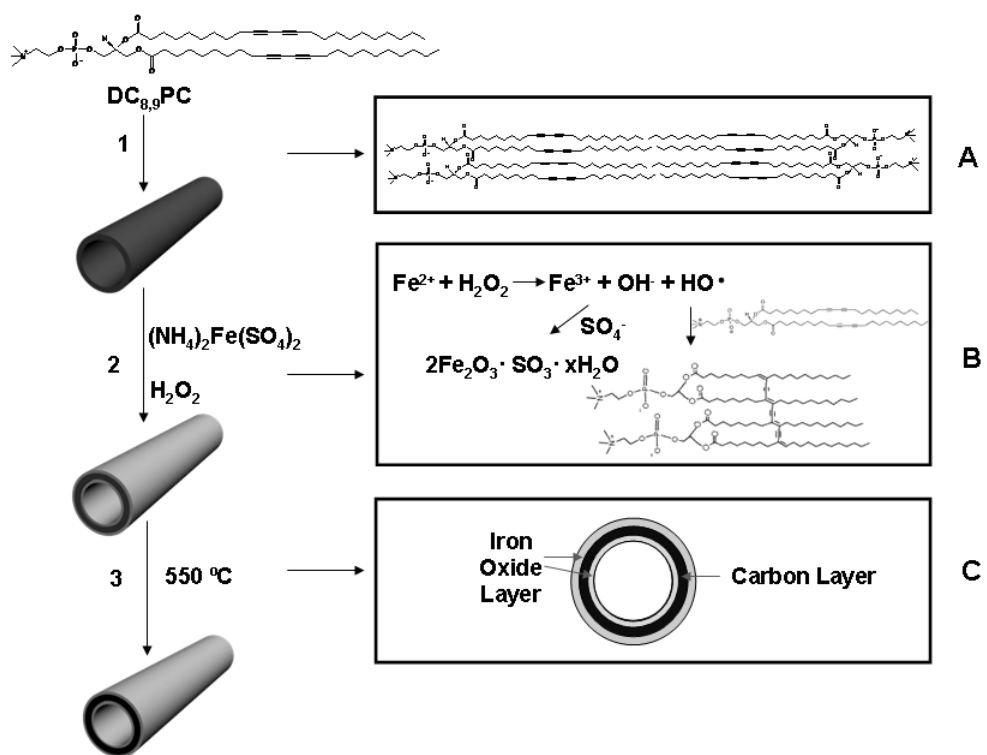


Figure 4.1.1. Schematic diagram illustrating reaction mechanisms responsible for formation of FMNTs.

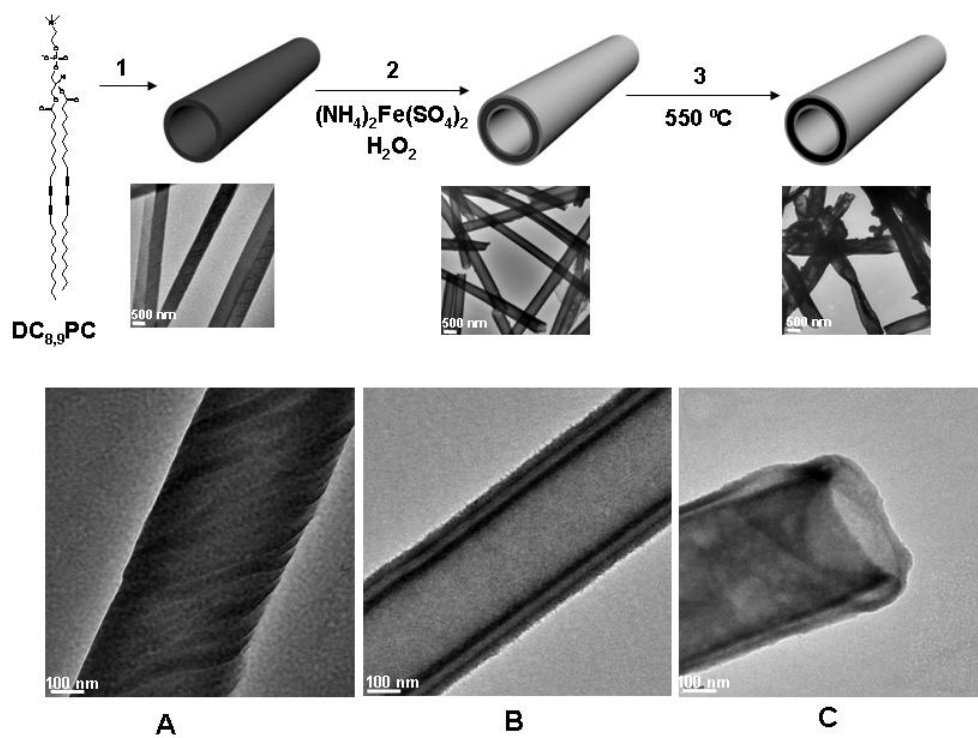


Figure 4.1.2. TEM images of nanotubes: (A) Step 1 — self-assembly of DC_{8,9}PC into nanotubes; (B) Step 2 — reactions of $(\text{NH}_4)_2\text{Fe}(\text{SO}_4)_2$ and H_2O_2 ; (C) Step 3 — thermal exposure to $550\text{ }^\circ\text{C}$ for 0.5 hour.

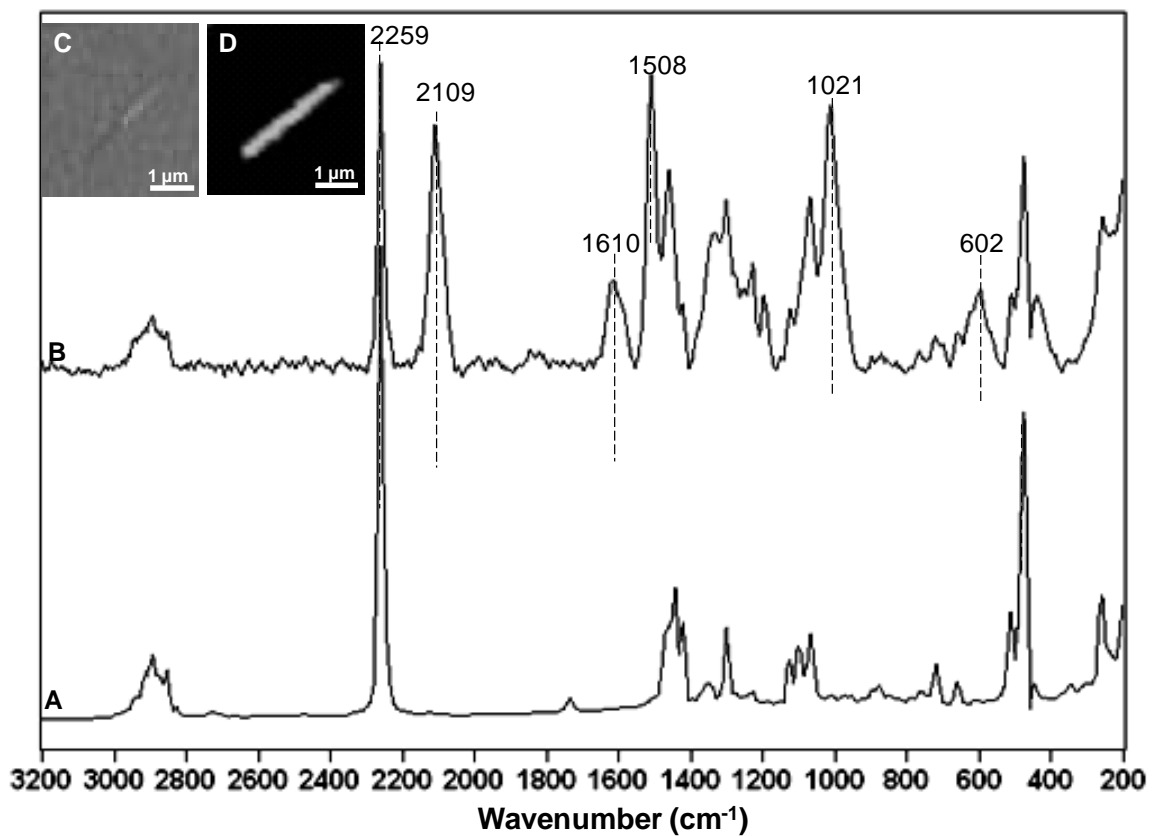


Figure 4.1.3. Raman spectra in the 3200-200 cm⁻¹ region of nanotubes after Step 1 (A) and Step 2 (B), Optical image (C) and Raman image (D) of nanotubes after Step 2.

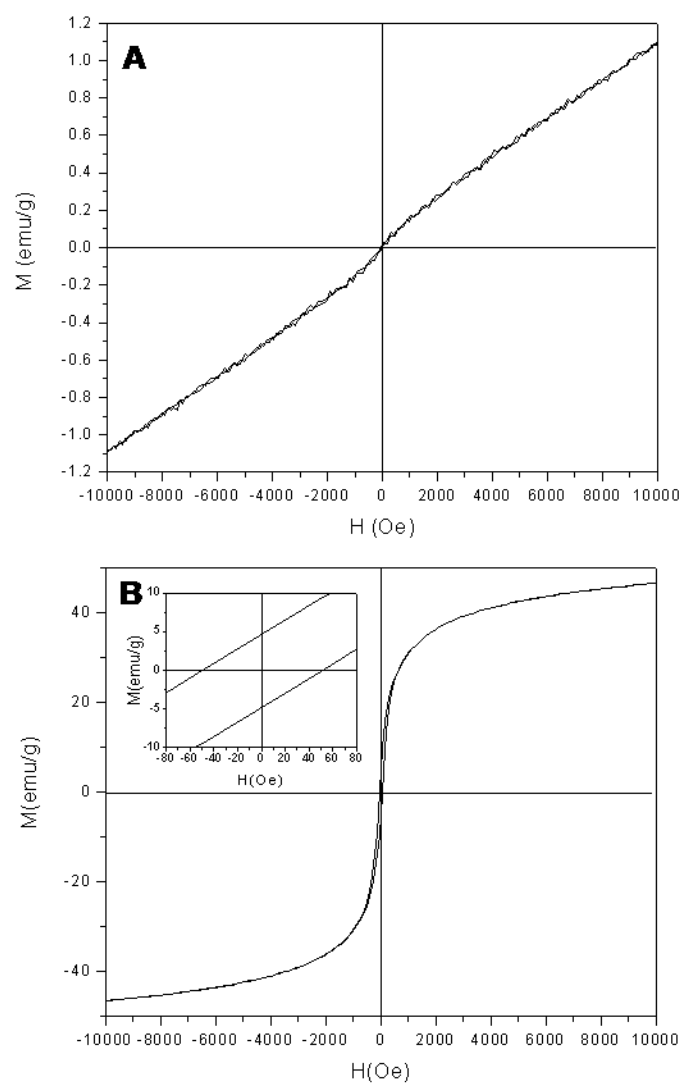


Figure 4.1.4. Magnetic hysteresis loops of nanotubes after Steps 2 (A) and 3 (B) in Figure 4.1.1.

References

- (1) Wachowiak, A.; Wiebe, J.; Bode, M.; Pietzsch, O.; Morgenstern, M.; Wiesendanger, R. *Science* **2002**, *298*, 577.
- (2) Choe, S.-B.; Acremann, Y.; Scholl, A.; Doran, A.; Stöhr, J.; Padmore, H. A. *Science* **2004**, *304*, 420.
- (3) Liu, L.; Kou, H. Z.; Mo, W. L.; Liu, H. J.; Wang, Y. Q. *J. Phys. Chem. B* **2006**, *110*, 15218.
- (4) Tang, B.; Wang, G. L.; Zhuo, L. H.; Ge, J. C.; Cui, L. J. *Inorg. Chem* **2006**, *45*, 5196.
- (5) Raming, T. P.; Winnubst, A. J. A.; van Kats, C. M.; Philipse, A. P. *J. Colloid Interface Sci.* **2002**, *249*, 346.
- (6) Cao, H. Q.; Wang, G. Z.; Zhang, L.; Liang, Y.; Zhang, S. C.; Zhang, X. R. *Chem. Phys. Chem.* **2006**, *7*, 1897.
- (7) Wen, X. G.; Wang, S. H.; Ding, Y.; Wang, Z. L.; Yang, S. H. *J. Phys. Chem. B* **2005**, *109*, 215.
- (8) Zhang, X. G.; Liu, H.; Wei, Y. *J. Mater. Res.* **2005**, *20*, 628.
- (9) Son, S. J.; Reichel, J.; He, B.; Schuchman, M.; Lee, S. B. *J. Am. Chem. Soc.* **2005**, *127*, 7316.
- (10) Suber, L.; Imperatori, P.; Ausanio, G.; Fabbri, F.; Hofmeister, H. *J. Phys. Chem. B* **2005**, *109*, 7103.
- (11) Yager, P.; Schoen, P. E. *Mol. Cryst. Liq. Cryst.* **1984**, *106*, 371-381.
- (12) Schwertmann, U.; Cornell, R. M. *Iron Oxides in the Laboratory: Preparation and Characterization* 2nd ed.; Weinheim: New York 2000.

- (13) Margulis, E. V.; Savchenko, L. A.; Shokarev, M. M.; Beisekeeva, L. I.; Vershinina, F. I. *Russ. J. Inorg. Chem* **1975**, *20*, 1045.
- (14) Schoen, P. E.; Yager, P. J. *Polym. Sci. Polym. Phys. Ed.* **1985**, *23*, 2203.

PART II: STRUCTURAL AND MORPHOLOGICAL FEATURES

Introduction

Magnetic nanomaterials are of particular interest due to their potential applications ranging from information storage to nano-fluidics, or drug delivery systems to biosensing devices or magnetic resonance imaging, to name just a few.¹ One of the recent examples of utilization of superparamagnetic nanoparticles was their ability to repair mechanically damaged polymer matrices upon exposure to the oscillating magnetic field.² Because shape significantly contributes to magnetic properties,^{3,4} thus providing an opportunity for diversified applications, a quest for developing new magnetic nanomaterials with unique shapes continues. Various magnetic nanotubes have been prepared including FePt,⁵ Fe₃O₄,^{5,6} NiFe₂O₄,⁷ Fe₃O₄/silica,^{8,9} Fe₃O₄/polymer,¹⁰ Fe₃O₄/polypeptide,¹¹ and cobalt/polystyrene¹² nanotubes, and applications in bioseparation,^{8,9} drug delivery,^{8,9,10} and gene transfer¹¹ have been demonstrated. If shape and size variations including wall thickness, diameter, and length can be controlled, magnetic properties may be altered, thus leading to new applications.

In view of these considerations we utilized biologically active phospholipids (PL) as templates to produce ferromagnetic iron oxide/carbon/iron oxide concentric nanotubes (FMNTs),¹³ where a carbon layer sheet was sandwiched between the iron oxide layers. The structural complexity of these multi-layered morphologies brought about questions regarding the makeup of the iron oxide layers as well as concentric carbon layer phase. These studies focus on the elucidation of the content of these phases, their location, and how multilayers are assembled.

Experimental

1,2-bis(10,12-tricosadiynoyl)-*sn*-glycero-3-phosphocholine (DC_{8,9}PC) was purchased from Avanti Polar Lipids, Inc. Ammonium iron (II) sulfate hexhydrate ((NH₄)₂Fe(SO₄)₂·6H₂O), and hydrogen peroxide (H₂O₂) (30 wt. % in water) were purchased from Aldrich Chemical Co.

A schematic diagram illustrating the formation of nanotubes containing inorganic layers is shown in Figure 4.2.1, which followed the procedures published previously.¹³ DC_{8,9}PC nanotubes were obtained using the literature method.^{14,15} 10 mL of an aqueous dispersion with 1.1 mol/L DC_{8,9}PC nanotubes was purged with N₂ for 0.5 hr, followed by the addition of 0.5 mL of 0.4 mol/L ammonium iron (II) sulfate hexhydrate aqueous solution, which served as a reducing agent. After 0.5 hr, the final step involved the addition of 0.2 mmol of hydrogen peroxide, which acted as an oxidizing agent to react with the reducing agent. The reaction continued for 1 hour after which time the product was collected by centrifuging and dialysis to remove excess ions. Finally, nanotubes were freeze dried and annealed at 550 °C for 0.5 hour. For reference purpose, final nanotubes mixed with 1 mol/L HCl for one week to remove iron oxide and final product were centrifuged and collected. DC_{8,9}PC powder was annealed at 550 °C for 0.5 hour and residue was collected.

Transmission electron microscopy (TEM) and selected area electron diffraction (SAD) images of nanotubes were obtained using a Jeol JEM-2100 TEM operated at 200 kV, and high-resolution TEM (HRTEM) images were collected by a Hitachi HF2000 TEM operated at 300 kv. Raman spectra were obtained with a Renishaw inVia Raman microscope with a 785 nm diode laser. The Raman spectra of samples were collected with

a 30 mW laser power on the sample and an acquisition time of 1500 sec. X-ray diffraction (XRD) was collected by X-ray diffractometer with CuK α radiation. Mossbauer spectroscopy was obtained by a Mössbauer spectrometer with ^{57}Co (Rh) source. The conductivity tests of nanotubes were conducted using focused ion beam (FIB). The nanotube was deposited on the oxidized wafer and two platinum pads were fixed at the both end of the nanotube. Current-voltage (I-V) curves of samples were measured when the electrode tips contacted with platinum pads.

Results and Discussion

Figure 4.2.1, A-D illustrates a schematic diagram of the synthesis of FMNTs which involves self-assembly of PL nanotubes (Step 1), followed by reactions of $(\text{NH}_4)_2\text{Fe}(\text{SO}_4)_2$ and H_2O_2 (Steps 2 and 3), and further thermal annealing at 550 °C (Step 4). Figure 4.2.1, A'-D' show TEM images of nanotubes produced in each step. As seen in Figure 4.2.1, A', a nanotube with a 500 nm length is observed, resulting from the PL self-assembly. Figure 4.2.1, Images B' and B'', illustrate the morphology of PL nanotubes upon iron oxide precursor $(\text{NH}_4)_2\text{Fe}(\text{SO}_4)_2$ reactions in step 2, which revealed that the darker layers resulting from higher electron density of Fe^{2+} ions are formed around PL nanotubes as well as in the PL interbilayers. This is attributed to the electrostatic interactions among Fe^{2+} , SO_4^- , NH_4^+ ionic species and phosphocholine groups of PL, allowing these ionic species to form nanotube surfaces or diffuse into the PL interbilayers. Upon further reactions using H_2O_2 oxidizing species (Step 3), Fe^{2+} ions are partially oxidized to Fe^{3+} and, as shown in the TEM image of Figure 4.2.1, C', uniform iron oxide layers are generated on PL nanotube surfaces. The final Step 4 involves thermal annealing of nanotubes at 550 °C, and as shown in Figure 4.2.1, D', nanotube

morphologies are retained. One of the intriguing features of this process is the formation of multilayer structures, where concentric iron oxide nanotubes are separated by a layer carbon sheet.

In an effort to dictate crystalline structure of FMNTs, XRD was performed. As shown in Figure 4.2.2, A and B, illustrates XRD patterns of FMNTs and standard magnetite (Fe_3O_4), respectively. The diffraction peaks of FMNTs (Trace A) are in good agreement with those of magnetite (Trace B). However, since maghemite ($\gamma\text{-Fe}_2\text{O}_3$) also exhibits a similar cubic lattice structure and the same lattice constants as magnetite, both of the phases may coexist in the iron oxide phase of FMNTs. Furthermore, the additional peak at $2\theta = 25^\circ$ is detected, corresponding to (012) diffraction of hematite ($\alpha\text{-Fe}_2\text{O}_3$). Thus, a small amount of hematite impurity is present in the iron oxide phase of FMNTs, and the Scherrer equation using the (311) peak of FMNTs predicts that the average crystallite size of iron oxide is approximately to be 10.6 nm.

To further confirm structural features of FMNT, SAD was utilized, and the image of FMNT is illustrated in Figure 4.2.3. The presence of amorphous halos with the d-spacing values of 4.85, 2.96, 2.53, 2.10, 1.72, 1.61, 1.48, and 1.08 Å is observed with correspond to magnetite (Fe_3O_4) and maghemite ($\gamma\text{-Fe}_2\text{O}_3$) d-spacings that exhibit 4.85, 2.95, 2.52, 2.09, 1.70, 1.61, 1.58, 1.09 Å values.¹⁶ To further elucidate localized structural details, phase analysis of FMNTs using HRTEM and Mossbauer spectroscopy were conducted. Figure 4.2.4, A, B, and C illustrate HRTEM images of the surface and walls of FMNTs as well as a schematic diagram of the FMNT morphology, respectively. As seen in TEM images of the FMNT surface in Figure 4.2.4, A, the surface layer consists of a number of small single crystals that exhibit different orientations. The enlarged images

A' and A'' show that the lattice spacing of 2.09 and 4.85 Å exist, and the insert images a' and b' show diffraction patterns of A' and A''. These results show that the image a' gives the diffraction patterns of magnetite or maghemite with the following reflections: 400 lattice spacing of 2.09 Å and 311 with 2.53 Å, whereas Image a'' represents the 111 lattice spacing of 4.85 Å, 220 of 2.95 Å, and 511 of 1.61 Å. Thus, the lattice analysis provides further evidence for the existence of magnetite or maghemite phases and the size of magnetite or maghemite crystalline phase as seen in Figure 4.2.4, A, is estimated to be approximately 10 nm. These results are in good agreement with the 10.6 nm values obtained from XRD data.

Further analysis of the data shown in Figure 4.2.4, B and B', illustrate that the darker layers represent iron oxide crystals, whereas lighter layers are carbon sheets resulting from crosslinking of PL bilayers after annealing. Iron oxide is deposited onto the external and internal surfaces of the nanotube and the interlayers between two carbon layers result from C≡C crosslinking of hydrophobic tails of PLs. Enlarged TEM image B' illustrates the presence of multi-layered carbon layers (arrows), which is schematically depicted in Figure 4.2.4, C and C'. The cross-section of the wall of the FMNT is composed of the carbon multilayers separated by iron oxide crystals. The carbon layered structure of FMNT, however, is different from multi-walled carbon nanotubes (MWNT). Typically, carbon nanotubes have an inner diameter of 10 nm and an interlayer distance of 3.3 Å. In contrast, the thickness of FMNT carbon layers is about 5 nm with a 3 nm interlayer distance, which results from PL spacing of the initial template which is reflected in the formation of amorphous carbon layer after annealing of PL bilayers

In an effort to determine the elemental composition of FMNT as a function of

distance from the FMNT wall, Energy dispersive X-ray spectroscopy (EDS) analysis was performed. The results are illustrated in Figure 4.2.5, where Image A shows TEM images of a FMNT and Image B show that the height contrast image of the selected area in A. As seen in B, two brighter layers result from magnetite, whereas the darker layers are due to the carbon phase. To determine spatial distribution of each element, the composition distribution was measured along the x-y direction and the results are shown in Figure 4.2.5, C. As seen, Fe and O dominate the content of the wall, and lesser quantities of C and S elements are detected. Also, the greater intensity of Fe and O appear at 15 and 45 nm which corresponds to the positions of the two magnetite layers (brighter areas) in the TEM Image B. Small contents of C and S show that, in addition of the magnetite phase, S is also present in the iron oxide lattice is detected, which is impurities in the iron oxide phase.

The presence of iron oxide phases provides an opportunity for utilizing Mössbauer spectroscopy as a function of temperatures. The results are shown in Figure 4.2.6, Traces A-G. As seen in Trace A collected at 295K, the spectrum exhibits two sextets (a and b) and two doublets (c and d). The two sextets of a and b exhibit characteristics of spinel Fe_3O_4 .¹⁷ Thus, the presence of $\gamma\text{-Fe}_2\text{O}_3$ can be excluded resulting from its single Fe^{3+} sextet and the detailed crystalline structure of Fe_3O_4 is depicted in Figure 4.2.7, A and B depicting the crystal Fe_3O_4 unit cell and its polyhedral network. As seen, Fe_3O_4 exhibits cubic spinel lattice, where the tetrahedral sites (A) are completely occupied by Fe^{3+} , where as octahedral sites (B) are filled by equal amounts of Fe^{3+} and Fe^{2+} , which are usually described as an average oxidation state of $\text{Fe}^{2.5+}$ resulting from fast electron exchange between the Fe^{2+} and Fe^{3+} . As seen from the Mössbauer spectrum analysis

shown in Figure 4.2.6, A, the spectrum a with the isomer shift of 0.167 mm/s indicates the presence of tetrahedral Fe^{3+} , whereas the spectrum b with the isomer shift of 0.502 mm/s corresponds to the octahedral $\text{Fe}^{2.5+}$. The magnetic hyperfine field values (H_{hf}) of tetrahedral a and octahedral b sites are 482 kOe and 450 kOe, respectively. In addition, as seen in the doublet spectra c and d, the doublet c with isomer shift of 1.059 mm/s corresponds to a paramagnetic Fe^{2+} phase, while the doublet d with isomer shift of 0.271 mm/s results from a paramagnetic Fe^{3+} phase. The presence of paramagnetic iron phase is attributed to the incomplete crystallization of Fe_3O_4 . Upon integration of the area for each component, the percentage of Fe^{2+} and Fe^{3+} in Fe_3O_4 , paramagnetic Fe^{2+} , and paramagnetic Fe^{3+} phase are 36.48, 40.41, and 23.11%, respectively. Traces B, C, and D of Figure 4.2.6 collected at 240, 180, 130 K exhibit similar spectral features as those observed in Trace A, indicating no structural changes within this temperature range. However, at 77, 40, and 4.2 K, the Fe^{3+} and $\text{Fe}^{2.5+}$ sextets exhibit broader line widths illustrated in Traces E, F and G. As seen, the most significant changes are shown in Trace G at 4.2 K illustrating that the isomer shift values for tetrahedral Fe^{3+} of 0.360 mm/s and for octahedral $\text{Fe}^{2.5+}$ is 0.604 mm/s. Furthermore, intensities of the two paramagnetic peaks decrease and the isomer shift values for paramagnetic Fe^{3+} and Fe^{2+} are 0.432 and 0.863 mm/s, respectively. Significant changes of paramagnetic phases result from the phase changes or electron mobility decreases at low temperatures, and these data show that FMNTs consist of Fe_3O_4 crystals as well as paramagnetic Fe^{2+} and Fe^{3+} , where Fe_3O_4 crystal structures are illustrated in Figure 4.2.7 depicting the coexistence of tetrahedral Fe^{3+} and octahedral $\text{Fe}^{2.5+}$ sites, whereas the paramagnetic phase results from the uncompleted crystallization of iron oxide.

Raman spectra were also utilized to analyze the chemical composition of FMNTs. Figure 4.2.8, A and B, Traces a, b, c, and d, show Raman spectra in the 900-200 and 2000-1000 cm^{-1} regions collected from FMNT, FMNT after acid reactions leading to the removal of the iron oxide layers, PL residues after annealing, and Fe_3O_4 control, respectively. As seen in Figure 4.2.8, A, Trace a, recorded from FMNTs, characteristic bands of magnetite are detected at 670 and 318 cm^{-1} , and the bands at 670 and 318 cm^{-1} due to magnetite are not present in Traces b and c. However, the presence of the bands at 878, 770, 673, 602, 622, 435, and 381 cm^{-1} in Traces a, b and c are detected and are attributed to the carbon layers resulting from the degradation of PL. It should be pointed out that the carbon layers of FMNT in Trace a are identical to the carbon layers of FMNT after acid reactions (Trace b) and PL residues after annealing (Trace c), but due to the low concentration levels, the Fe_3O_4 bands at 538 and 462 cm^{-1} are not detected in FMNTs (Trace a). For reference, Trace d illustrates Raman spectrum of standard Fe_3O_4 which shows bands at 670, 538, 462, and 318 cm^{-1} . In addition, as seen in the 2000-1000 cm^{-1} region (Figure 4.2.8, B) of FMNTs (Trace a), two bands at 1580 and 1330 cm^{-1} are observed which are characteristics of carbon nanotubes with the tangential G-band resulting from the graphite-like in plane modes and the disorder-induced D-band of carbon nanotubes, respectively.¹⁸ Similar G- and D-bands are detected for Traces c and d which are due to the presence of identical carbon layers in FMNTs. Thus, Raman measurements support previous conclusions that FMNTs consist of magnetite and carbon phases.

In view of above analysis, FMNTs are concentric magnetite/carbon/magnetite nanotubes, with a carbon layer sandwiched between two magnetite layers as well as

magnetite inside of the carbon interlayer. These unique structural features offer a number of promising properties for FMNTs. One of the examples is shown in Figure 4.2.9, A, which shows a setup for conductivity measurements FIB, where FMNT is deposited on the oxidized wafer and two platinum pads are fixed at the both ends of the nanotube. Using this setup, electrical conductivity of the nanotube was measured when the electrode tips were in contact with the platinum pads. Figure 4.2.9, B and B' illustrate the FIB image and current-voltage (I-V) characteristics of a FMNT. As seen in Figure 4.2.9, B, conductivity measurements (current (I) vs. voltage (V)) were performed on a 12 μm long FMNT and Figure 4.2.9, B' illustrates that the resistance (R) and resistivity (ρ) of the FMNT are 8.3 M Ω and $3.3 \times 10^{-2} \Omega\cdot\text{m}$, respectively. In contrast, the results for nanotube prepared from the FMNT after removal of magnetite layers using acid etching process are shown in Figure 4.2.9, C and C'. Upon removing the magnetite phase, only carbon phase is present, and as seen in the FIB image of Figure 4.2.9, C, the nanotube remains stable and the results of conductivity measurements illustrated in Figure 4.2.9, C' show that the R and ρ values are 75 k Ω and $5.06 \times 10^{-4} \Omega\cdot\text{m}$, respectively. Thus, the resistivity decreases by two orders of magnitude For reference purposes, Figure 4.2.10, A shows a comparison of electrical resistivity and conductivity of FMNT (A), FMNT after removal of magnetite outer and inter layers (B), standard magnetite (C), and multi-walled carbon nanotube (MWNT) (D). As seen the ρ value of $3.2 \times 10^{-4} \Omega\cdot\text{m}$ ¹⁹ for magnetite is two orders of magnitude larger than that of FMNT, thus showing that the resistivity of FMNT is enhanced compared with magnetite particles. In contrast, the reported resistivity of a multi-walled carbon nanotube (D) is about $1.2 \times 10^{-6} \Omega\cdot\text{m}$.²⁰ To illustrate the significance of these data it is also of interest to compare magnetic properties of these materials which

are illustrated in Figure 4.2.10, B. As shown, saturation magnetization (M_r) values of FMNT (A), FMNT after removal of magnetite outer and inter layers (B), standard magnetite (C), and MWNT (D) are 79, 0.52, 78, and 0.4 emu/g, respectively. FMNT (A) and magnetite (C) are ferromagnetic and show similar magnetization values. However, FMNT after removal of magnetite outer and inter layers (B) revealed a paramagnetic behavior, thus no saturation magnetization was obtained. For comparison, the magnetization values at the magnetic field of 10k Oe was labeled. Due to the presence of small quantities of catalyst impurities, MWNT shows weak ferromagnetic characteristics with a M_r value of 0.4 emu/g. Thus, strong ferromagnetic properties of FMNT were obtained similar as magnetite and FMNT after removal of magnetite exhibit paramagnetic properties.

Conclusions

FMNTs are concentric magnetite/carbon/magnetite nanotubes where the carbon layer is sandwiched between two magnetite layers as well as magnetite is present inside the carbon interlayer. Also, FMNTs contain magnetite single crystals of 10.6 nm in size as well as paramagnetic iron oxide impurity. Resulting from its unique structural feature, FMNT was demonstrated to make a nano-conductor device. The resistivity of FMNTs and FMNTs after acid treatment were measured as 3.3×10^{-2} and $5.06 \times 10^{-4} \Omega \cdot m$, respectively, and suggest that the FMNTs can be utilized to make conductive devices and their conductivity can be altered by changing their phase composition.

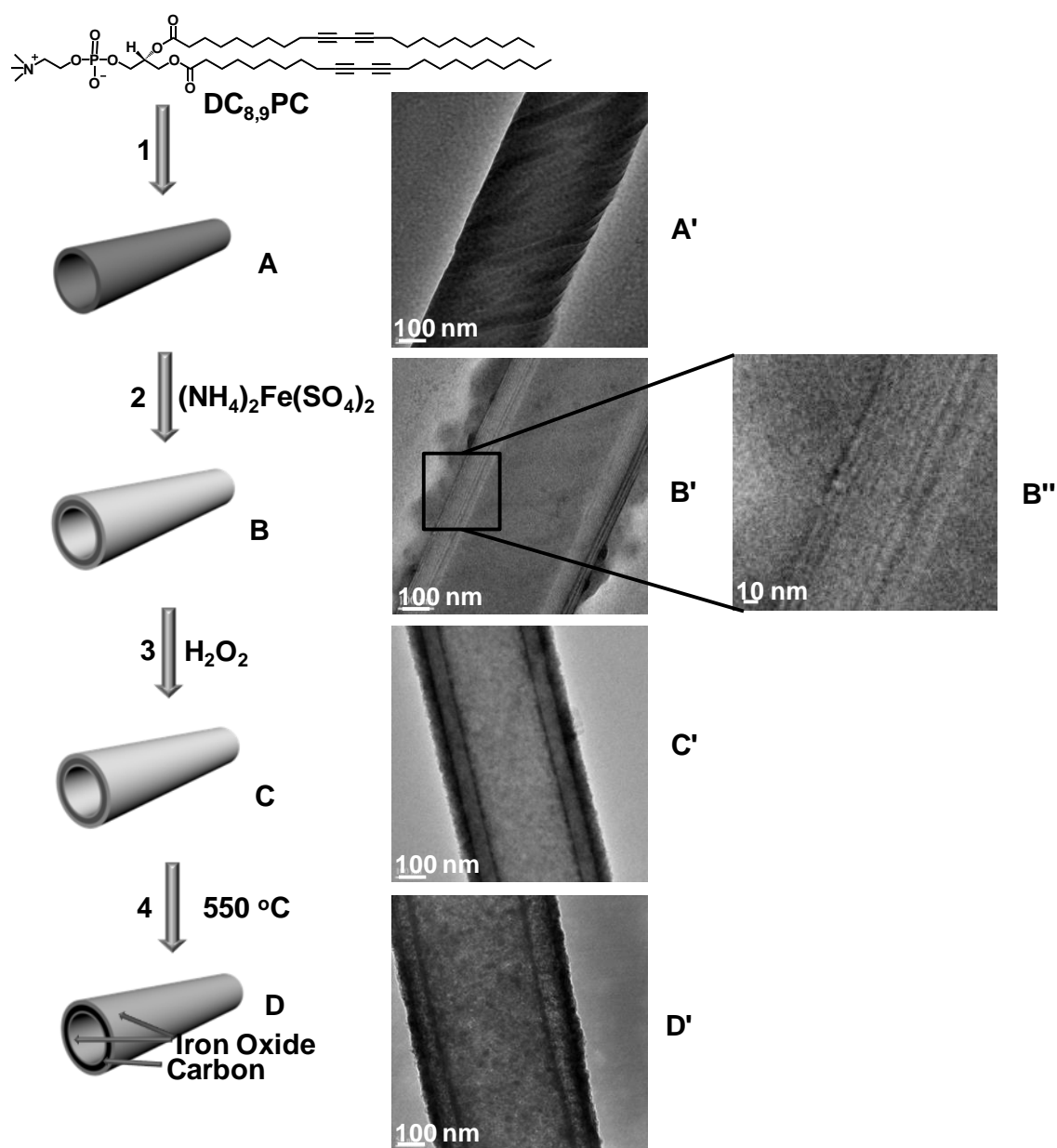


Figure 4.2.1. Schematic diagram of FMNT formation: (A) Step 1 – self-assembly of DC_{8,9}PC into nanotubes; (B) Step 2 – addition of (NH₄)₂Fe(SO₄)₂; (C) Step 3 – reactions of H₂O₂; (D) Step 4 – thermal exposure to 550 °C for 0.5 hour. TEM images of nanotubes in each step are show in A'-D'.

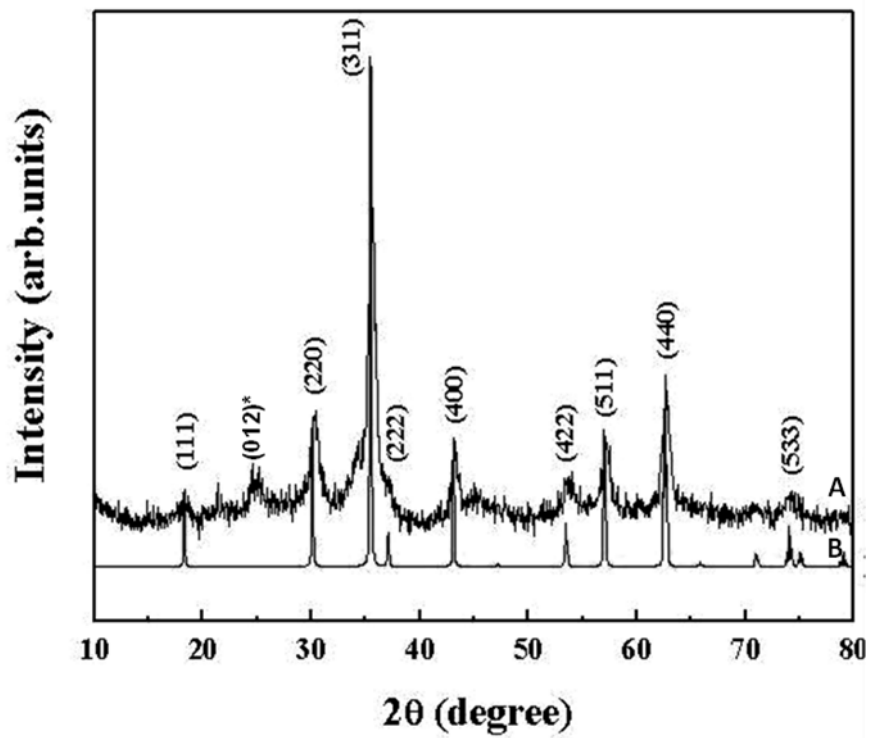


Figure 4.2.2. X-ray diffraction (XRD) of FMNTs (A) and Fe₃O₄ (B).

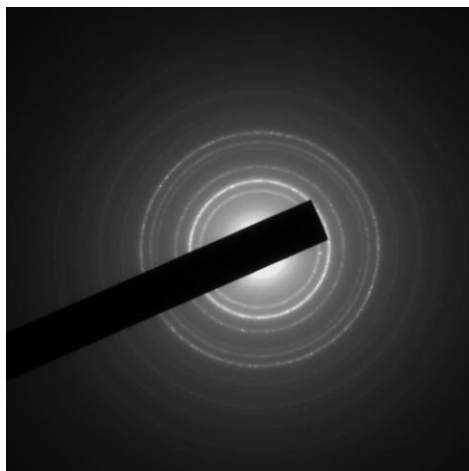


Figure 4.2.3. Selected area electron diffraction (SAD) of FMNTs.

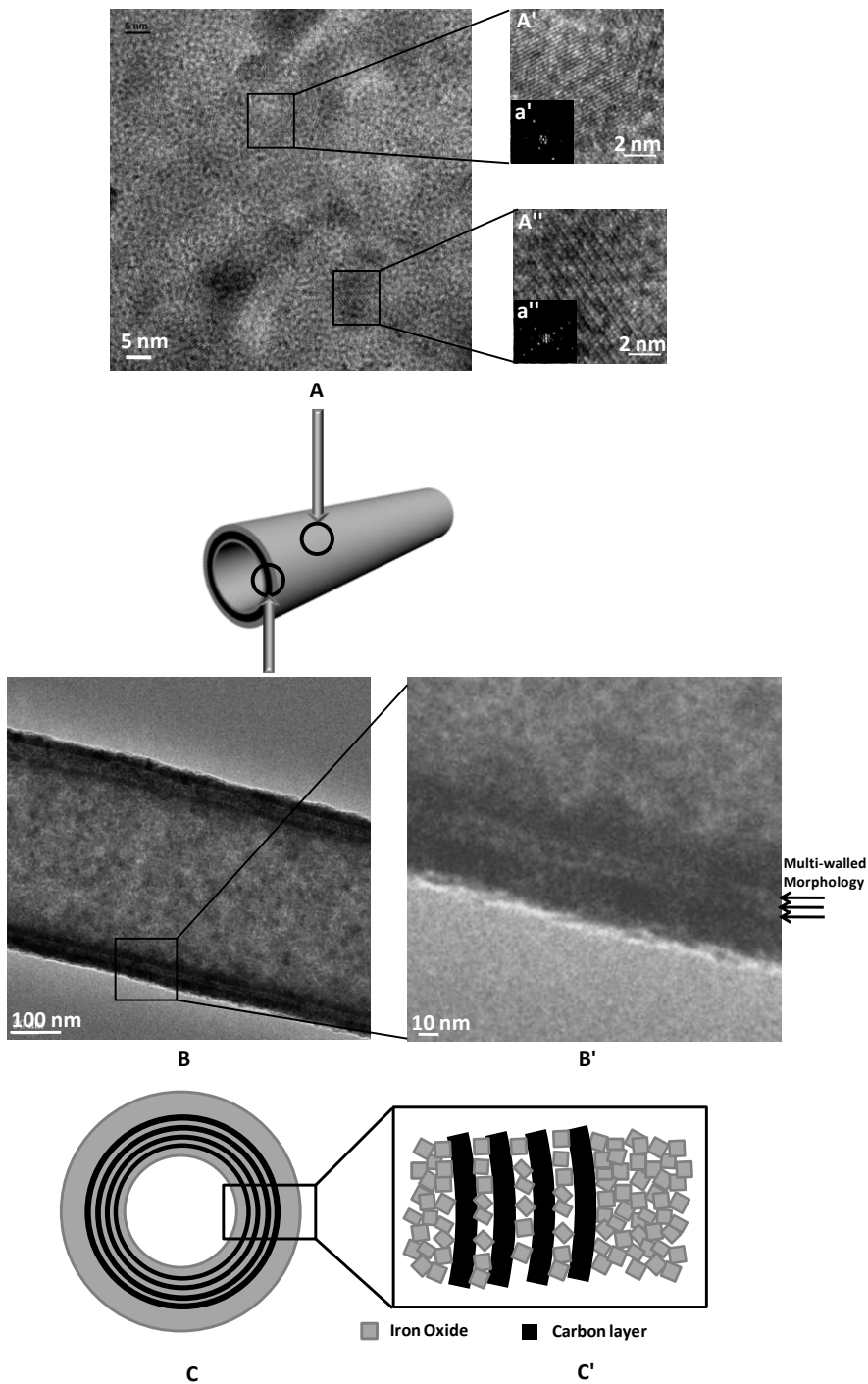


Figure 4.2.4. (A) High-resolution TEM image of FMNT surface and images (A') and (A'') demonstrate enlarged images of selected area where insert images a' and a'' show their diffraction patterns. a' reveals a diffraction pattern in 400 lattice spacing of 2.09 Å and

311 lattice spacing of 2.53 Å, while a" represents the 111 lattice spacing of 4.85 Å, 220 lattice spacing of 2.95 Å, and 511 lattice spacing of 1.61 Å; (B) and (B') TEM images of FMNT wall structures; (C) and (C') schematic diagram of structures of FMNT, which consist of concentric multilayered carbon sheet and iron oxide layers. Gray squares represent iron oxide single crystals and black rings represent carbon layers.

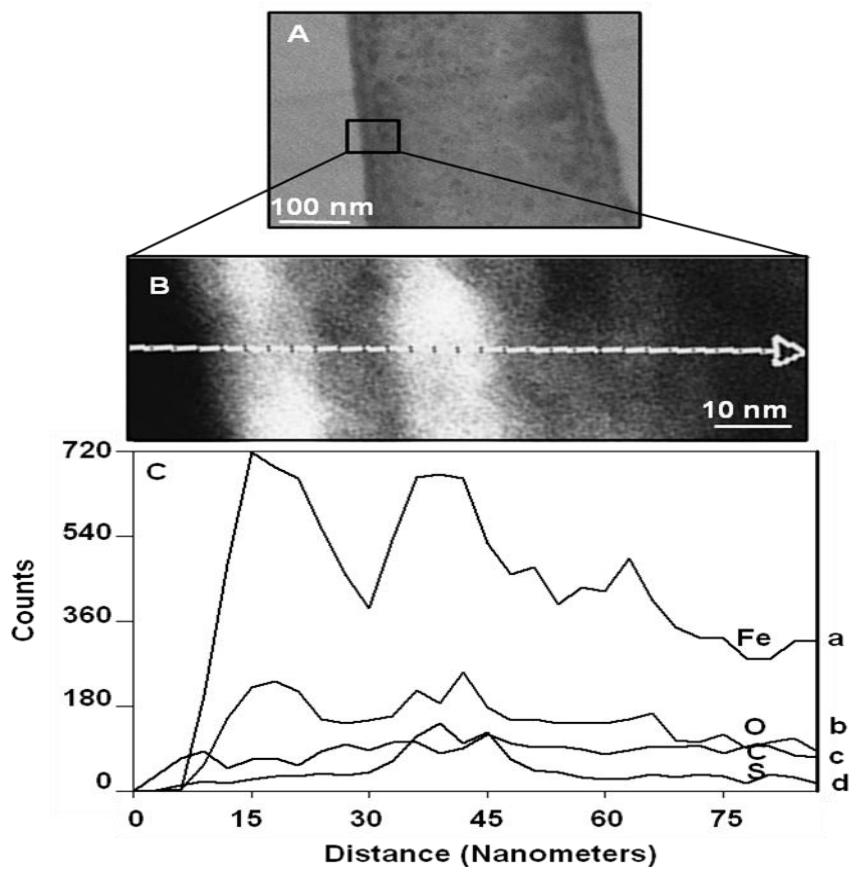


Figure 4.2.5. (A) TEM image of FMNT; (B) height contrast TEM image of selected area on FMNT; (C) energy dispersive X-ray spectroscopy (EDS) of element distribution along the arrow as draw in B, where trace a, b, c and d represent Fe, C, O, and S elements, respectively.

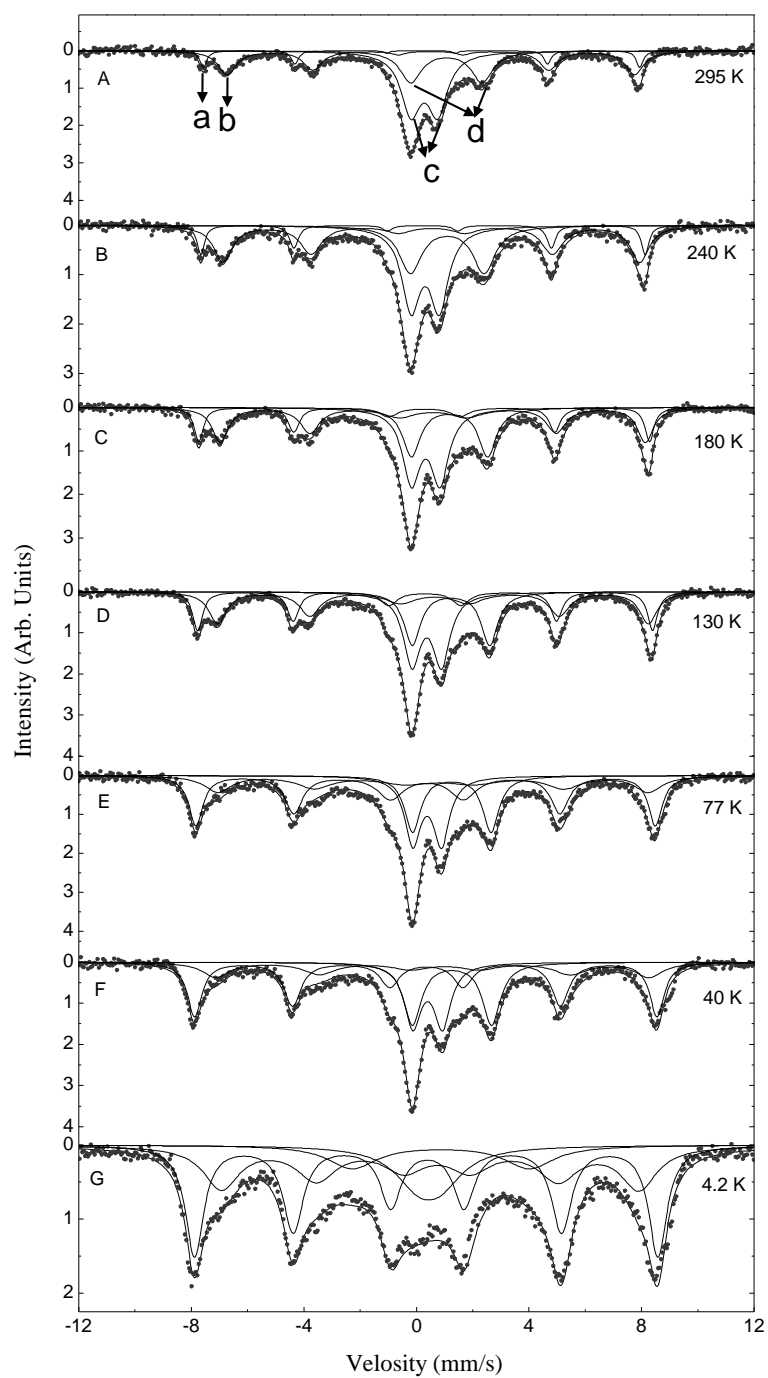


Figure 4.2.6. Mössbauer spectra of FMNTs recorded at various temperatures: (A) 295 K; (B) 240 K; (C) 180 K; (D) 130 K; (E) 77 K; (F) 40 K; (G) 4.2 K.

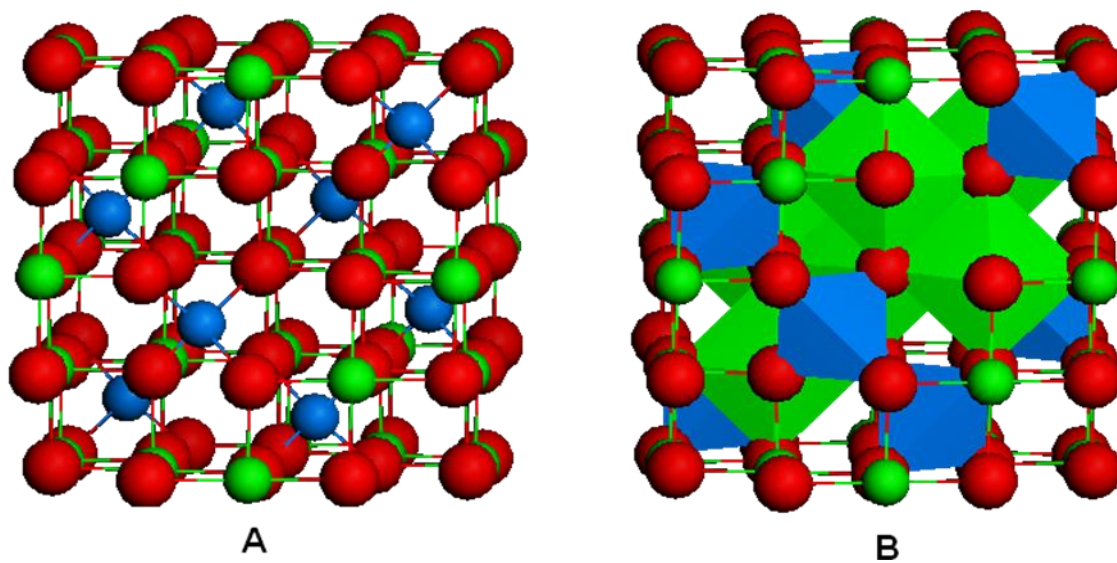


Figure 4.2.7. (A) Crystal lattice structure of magnetite: red-oxygen, blue-tetrahedral Fe^{3+} , and green-octahedral $\text{Fe}^{2+}/\text{Fe}^{3+}$; (B) Polyhedral network of magnetite.

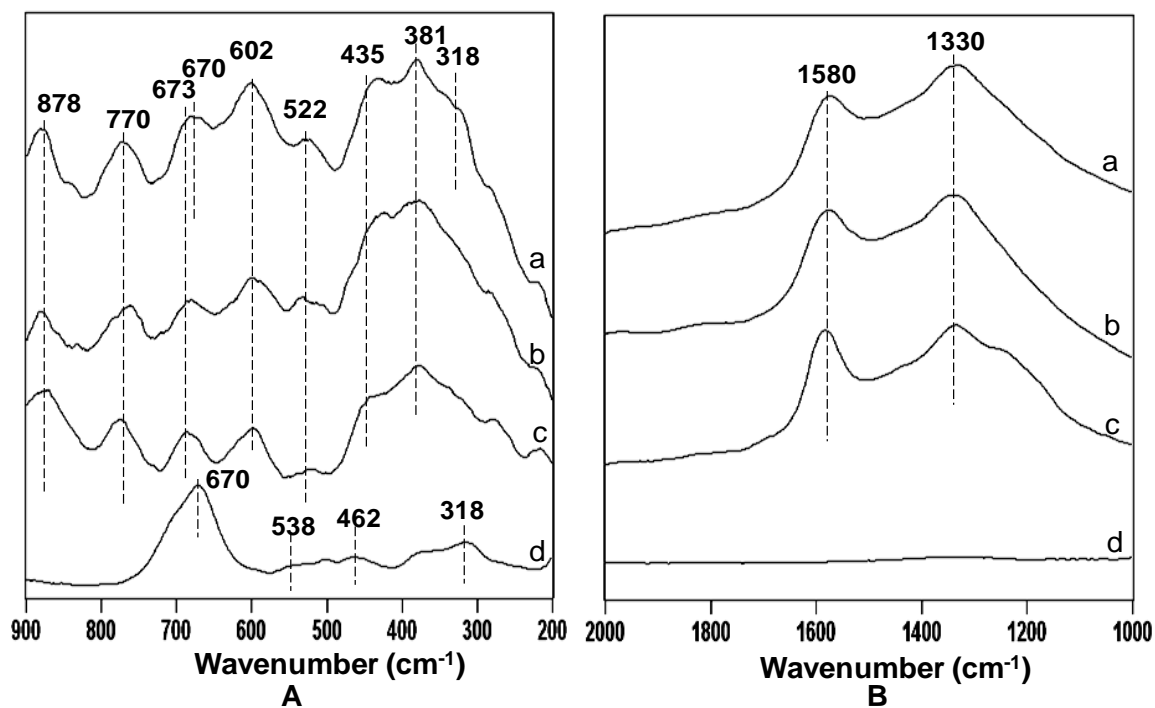


Figure 4.2.8. Raman spectra in the 900-200 cm^{-1} region (A) and 2000-1000 cm^{-1} region (B): (a) FMNT; (b) FMNT after acid reactions; (c) PL powder annealed at 550 $^{\circ}\text{C}$; (d) standard Fe_3O_4 .

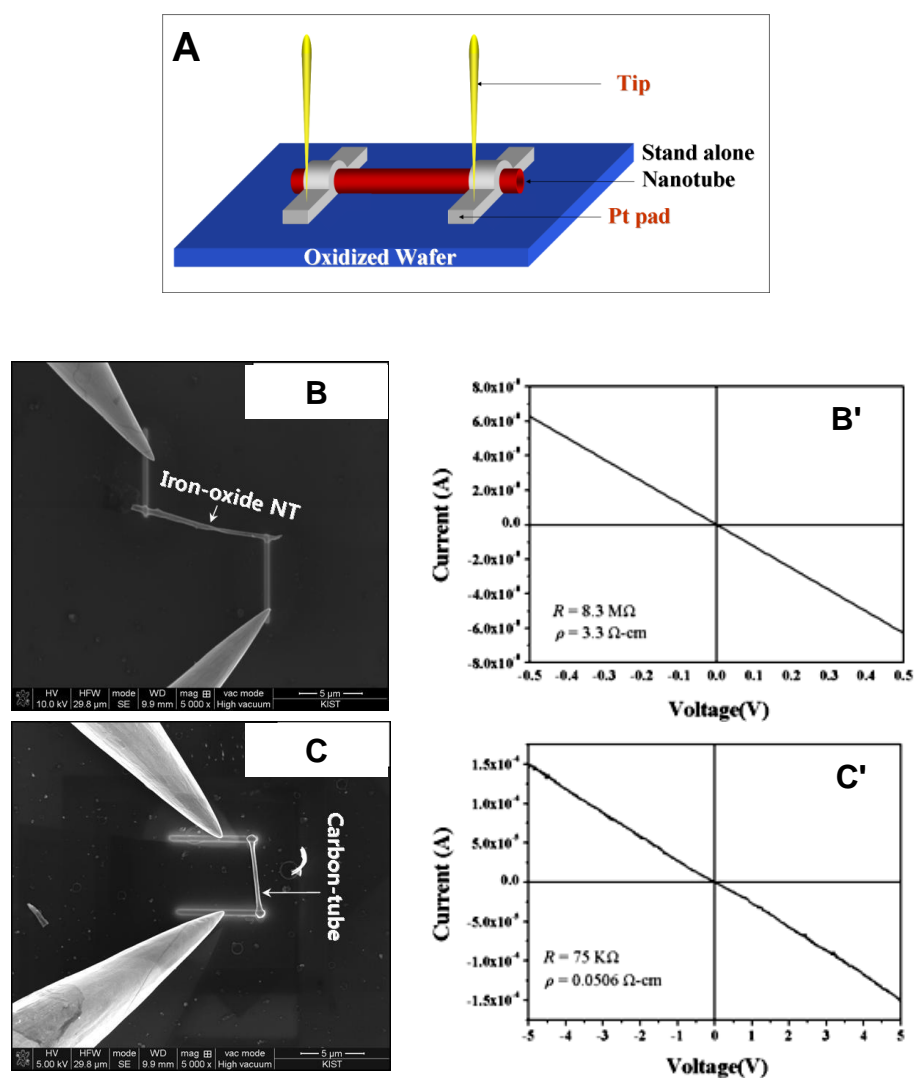


Figure 4.2.9. (A) Schematic diagram of measuring conductivity of a nanotube; (B) focused ion beam (FIB) image of FMNT; (B') Current-voltage (I-V) characteristics of FMNT; (C) FIB image of FMNT after acid treatment; (C') I-V characteristics of FMNT after acid treatment.

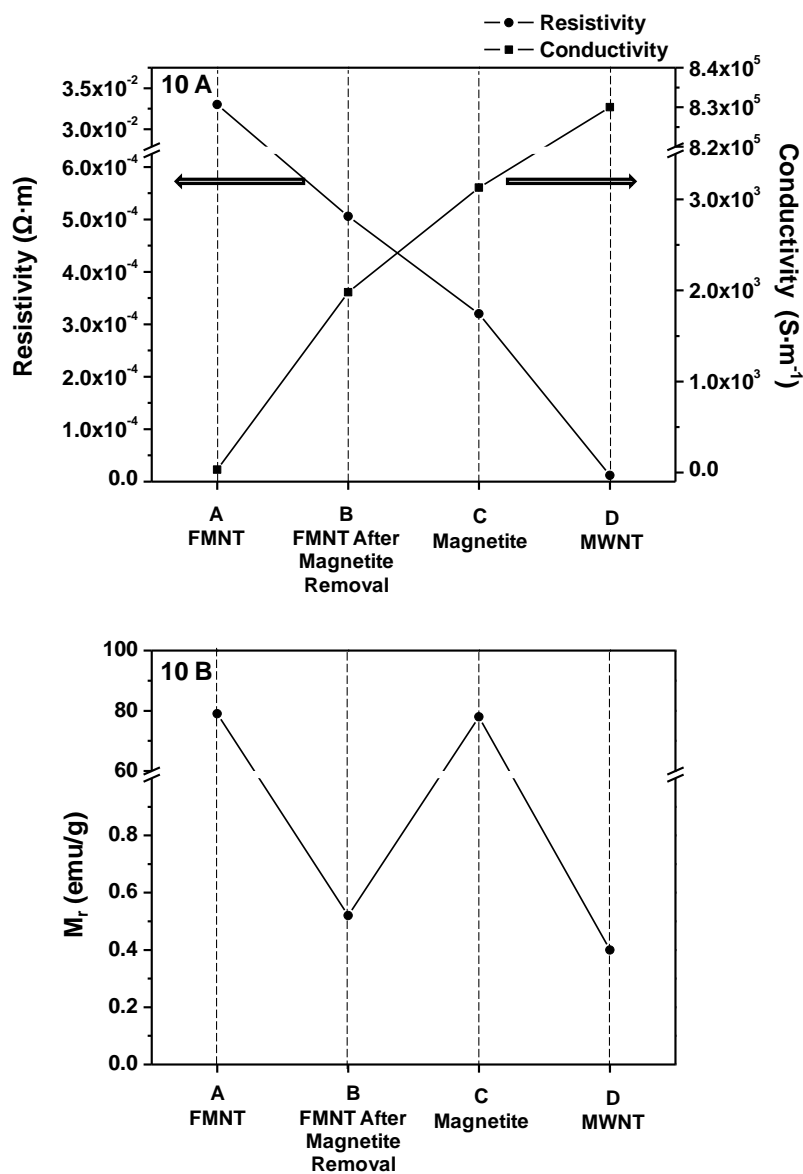


Figure 4.2.10. A. Electrical resistivity and conductivity comparisons: (A) FMNT; (B) FMNT after HCl reactions; (C) standard magnetite; (D) multi-walled carbon nanotube (MWNT). B. Saturation magnetization (M_r) comparisons: (A) FMNT; (B) FMNT after HCl reactions (paramagnetic behaviors and the magnetization value recorded at the magnetic field of 10k Oe); (C) standard magnetite; (D) multi-walled carbon nanotube (MWNT).

References

- (1) Pankhurst, Q. A.; Connolly, J.; Jones, S. K.; Dobson, J. *J. Phys. D: Appl. Phys.* **2003**, *36*, R167.
- (2) Corten, C.; Urban, M. W. *Adv. Mater.* **2009**, DOI: 10.1002/adma.200901940.
- (3) Wachowiak, A.; Wiebe, J.; Bode, M.; Pietzsch, O.; Morgenstern, M.; Wiesendanger, R. *Science* **2002**, *298*, 577.
- (4) Choe, S.-B.; Acremann, Y.; Scholl, A.; Bauer, A.; Doran, A.; Stöhr, J.; Padmore, H. A. *Science* **2004**, *304*, 420.
- (5) Sui, Y. C.; Skomski, R.; Sorge, K. D.; Sellmyer, D. J. *J. Appl. Phys.* **2004**, *95*, 7151.
- (6) Suber, L.; Imperatori, P.; Ausanio, G.; Fabbri, F.; Hofmeister, H. *J. Phys. Chem. B* **2005**, *109*, 7103.
- (7) Li, F.; Song, L. J.; Zhou, D.; Wang, T.; Wang, Y.; Wang, H. B. *J. Mater. Sci.* **2007**, *42*, 7214.
- (8) Son, S. J.; Reichel, J.; He, B.; Schuchman, M.; Lee, S. B. *J. Am. Chem. Soc.* **2005**, *127*, 7316.
- (9) Ma, H.; Tarr, J.; DeCoster, M. A.; McNamara, J.; Caruntu, D.; Chen, J. F.; O'Connor, C. J.; Zhou, W. L. *J. Appl. Phys.* **2009**, *105*, 07B309.
- (10) Lee, D.; Cohen, R. E.; Rubner, M. F. *Langmuir* **2007**, *23*, 123.
- (11) He, Q.; Tian, Y.; Cui, Y.; Mohwald, H.; Li, J. B. *J. Mater. Chem.* **2008**, *18*, 748.
- (12) Nielsch, K.; Castano, F. J.; Matthias, S.; Lee, W.; Ross, C. A. *Adv. Eng. Mater.* **2005**, *7*, 217.
- (13) Yu, M.; Urban, M. W. *J. Mater. Chem.* **2007**, *17*, 4644.

- (14) Schnui, J. M. *Science* **1993**, 262, 1669.
- (15) Yager, P.; Schoen, P. E. *Mol. Cryst. Liq. Cryst.* **1984**, 106, 371-381.
- (16) Cornell, R. M.; Schwertmann, U. *Iron oxides in the laboratory: preparation and characterization* John Wiley & Sons Ltd 2000.
- (17) Long, G. J.; Grandjean, F. *Mössbauer spectroscopy applied to inorganic chemistry*; Plenum Press: New York, 1989.
- (18) Dresselhaus, M. S.; Dresselhaus, G.; Saito, R.; Jorio, A. *Physics reports* **2005**, 409, 47.
- (19) Put, P. J. v. d. *The inorganic chemistry of materials*; Plenum Press: New York, 1998.
- (20) Ebbsen, T. W.; Lezec, H. J.; Hiura, H.; Bennett, J. W.; Ghaemi, H. F.; Thio, T. *Nature* **1996**, 382, 54.

CHAPTER V

MORPHOLOGICAL CONTROL OF FERROMAGNETIC NANOTUBES: WALL THICKNESS, DIAMETER, AND LENGTH

Introduction

Among synthetic routes to produce nanotubes the most common approach is to utilize tube-forming templates. Using this concept anodized aluminum oxide (AAO) templates were utilized to prepare magnetite (Fe_3O_4)/silica nanotubes,^{1,2} cobalt/polystyrene nanotubes,³ Ni and Co nanotubes,⁴ FePt and Fe_3O_4 nanotubes,^{5,6} NiFe_2O_4 nanocrystalline nanotubes,⁷ and magnetic carboxylated polypyrrole nanotubes containing Pd catalyst.⁸ Along the same lines, Fe_3O_4 /polymer⁹ and Fe_3O_4 /polypeptide nanotubes¹⁰ were prepared using layer-by-layer (LbL) assembly in the porous polycarbonate templates. Other approaches involved the template-based methods using pulsed laser deposition process of Fe_3O_4 onto MgO nanowires,¹¹ mineralization of tobacco mosaic virus (TMV) template,¹² bacterial Fe_3O_4 nanocrystal coated onto peptide nanotubes,¹³ and $\alpha\text{-Fe}_2\text{O}_3$ precursors to prepare Fe_3O_4 and $\gamma\text{-Fe}_2\text{O}_3$ nanotubes by hydrothermal methods.¹⁴ Although on one hand the drawback of using templates is that the final product dimensions are typically dictated by the size and shape of the template, on the other hand, if a nanotube diameter, length, and the wall thickness can be controlled, this approach offers fairly attractive alternatives compared to other approaches. Using this approach, functionalizing outer or inner template surfaces has led to Fe_3O_4 /silica¹, Fe_3O_4 /polypeptide¹⁰ and superparamagnetic Fe_3O_4 /polymer⁹ nanotubes.

Recent studies revealed that biologically active phospholipids (PL) nanotubes¹⁵ can effectively serve as precursors to produce ferromagnetic Fe_3O_4 /carbon/ Fe_3O_4

nanotubes (FMNTs),¹⁶ where using simple synthetic approaches a carbon layer sheet was sandwiched between the magnetite layers, thus resulting in concentric nanotubes. Since geometry and size considerations are important factors in achieving desirable magnetic properties, the ability to control the wall thickness, diameter, and the length are critical. Because equilibrium magnetization states identified as a uniform state with magnetic moments parallel to the tube axis and a flux-closure vortex state, the overall magnetization depends on the wall thickness and the aspect ratio.¹⁷⁻²⁰ Typically, the parallel orientation of magnetic moments with respect to the tube axis exists in the middle part of a nanotube, whereas the ends exhibit a vortex state.^{21,22} In the context of these considerations a diameter is also significant, and as shown, preferential parallel magnetic orientation in composite cobalt/polystyrene nanotubes with small diameters and isotropic magnetic features for larger diameters was observed.³ In view of these considerations, these studies describe a new synthetic platform allowing the control of wall thickness, length, and diameter of Fe₃O₄/carbon/Fe₃O₄ nanotubes.

Experimental

1,2-bis(10,12-tricosadiynoyl)-*sn*-glycero-3-phosphocholine (DC_{8,9}PC) was purchased from Avanti Polar Lipids, Inc. Ammonium iron (II) sulfate hexhydrate ((NH₄)₂Fe(SO₄)₂·6H₂O), hydrogen peroxide (H₂O₂) (30 wt. % in water), and cobalt naphthenate 6% were purchased from Aldrich Chemical Co. Extruder and polycarbonate membranes were obtained from Avanti Polar Lipids. Derakane polyester resin and methyl ethyl ketone peroxide (MEKP) were purchased from Ashland.

The procedures for preparation of FMNTs were followed the published previously.¹⁶ DC_{8,9}PC nanotubes were obtained using the literature method.^{15,23} 10 mL of an aqueous dispersion with 1.1 mol/L DC_{8,9}PC nanotubes was purged with N₂ for 0.5

hr, followed by the addition of 0.5 mL of 0.4 mol/L ammonium iron (II) sulfate hexahydrate aqueous solution, which served as a reducing agent. After 0.5 hr, the final step involved the addition of 0.2 mmol of hydrogen peroxide, which acted as an oxidizing agent to react with the reducing agent. The reaction continued for 1 hour after which time the product was collected by centrifuging and dialysis to remove excess ions. Finally, nanotubes were freeze dried and annealed at 550 °C for 0.5 hour.

In order to vary the thicknesses of the carbon layers, PL concentration and solvent environment were changed when preparing DC_{8,9}PC nanotube templates. DC_{8,9}PC nanotubes were obtained in 2 and 5 mg/mL PL in 85% methanol as well as 2 mg/mL PL in 70% ethanol solutions, respectively. The PL/Fe²⁺/H₂O₂ molar ratios were altered from 1:20:20, 1:40:40, 1:60:60, to 1:80:80, respectively. The diameter changes of PL nanotubes were obtained by incorporating saturated phospholipid spacers 1,2-dinonanoyl-sn-glycero-3-phosphocholine (DC₇PC) and 1,2-diundecanoyl-sn-glycero-3-phosphocholine (DC₉PC) into DC_{8,9}PC templates, which nanotube preparations were followed the literature procedures.²⁴ FMNTs were dispersed in water, followed by extruding nanotube/water solution using two 1 mL syringes through a 3 μm porous polycarbonate membrane without and within magnetic field paralleling to the membrane, respectively. FMNT/polyester nanocomposites were prepared by mixing FMNTs (4 % w/w) with Derakane polyester resin, followed by adding MEKP and cobalt naphthenate 6%. The composite were then deposited onto a mold and allowed to be cured in the presence of magnetic field along the mold long axis. After fully curing, the second layer of the composite was applied above the cured layer, where the magnetic filed direction was 90° with respect to the mold long axis.

Morphologies of nanotubes were obtained using a Jeol JEM-2100 transmission electron microscope (TEM) operated at 200 kV, and a FEI Quanta-200 scanning electron microscope (SEM). Magnetic hysteresis measurements were performed using a MicroMag Model 2900 alternating gradient magnetometer (AGM, Princeton Measurement Corp.) at room temperature.

Results and Discussion

Using the previously established protocol¹⁶ we prepared templates of 1,2-bis(10,12-tricosadiynoyl)-sn-glycero-3-phosphocholine (DC_{8,9}PC) phospholipid nanotubes that were further utilized to produce FMNTs. As depicted in Figure 5.1, FMNTs are concentric magnetite nanotubes separated by a carbon sheet concentric layer with the uniform diameter, wall thicknesses, and length. In an effort to vary the thickness of the carbon layer, magnetic nanotubes were prepared using DC_{8,9}PC nanotube templates by changing the PL concentration and solvent environments.²⁵ Figure 5.2, A, B, and C illustrate TEM images of magnetic nanotubes obtained from DC_{8,9}PC nanotubes in 2 and 5 mg/mL PL in 85% methanol as well as 2 mg/mL PL in 70% ethanol solutions, respectively. As seen in the enlarged images A', B' and C', nanotubes exhibit three concentric layers, where the darker layers are due to magnetite phase with a higher electron density and carbon layers (lighter). The thickness of the carbon layer increases from 6 to 12, to 50 nm, respectively, as the PL concentration changes from 2 to 5 mg/mL in methanol solutions and 2mg/ml in ethanol solutions. The ability to control geometry of the nanotubes is attributed to self-assembly of the PL template, which results from single-bilayered, double-bilayered, to multi-bilayered PL nanotubes and is achieved by changing PL concentration levels and solvent polarity, thus altering PL solubility.

Since PL is an amphiphatic molecule containing the hydrophilic phosphocholine head group and two hydrophobic hydrocarbon chains. The formation of PL nanotubes is attributed to the alcohol/water ratio which controls suitable solubility of PL. Also, the polarity of the alcohol plays a significant role. Considering formation of single and double vs multi-layered PL nanotube structures, it is apparent that the choice of solvent significantly affects PL structural features. For example, upon sonication of PL in H₂O, micelle or liposome solutions form. Addition of ethanol will change the solubility equilibrium such that the single or double-bilayered PL nanotubes can be formed. But no multi-bilayered nanotube formation exists due to strong affinity of methanol that prevents hydrophilic-hydrophilic interactions between PL bilayers. This is reflected in the solubility parameters due to hydrogen bonding interaction (δ_H) value of 11.0 (cal/cm³)^{1/2} for methanol,²⁶ which exhibits strong affinity to form H-bonding interactions with the PL head groups, thus, allowing formation of single bilayers. As the PL concentration increases, two bilayers have an opportunity to approach each other, thus facilitating the formation of double bilayered structures. In contrast, ethanol with the δ_H value of 4.3 (cal/cm³)^{1/2}²⁶ will promote solubility of hydrophobic ends. Thus, the PL δ value of 18.0 (cal/cm³)^{1/2} with respect to methanol and ethanol δ exhibits favorable interactions leading to the formation of single and double layers for methanol and multi-layers for ethanol. To schematically illustrate this process, Figure 5.3, A, B and C depicts the nanotube formation of 2 and 5 mg/ml PL in methanol solutions, and 2 mg/mL PL in ethanol solution, respectively. While detailed interactions between PL and alcohols are shown in Figure 5.3, A', B', and C', the H-bonding responsible for single, double, and multi-layers are illustrated in Figure 5.3, A" and C". As seen in Figure 5.3, A' and A", the stronger H-

bonding interactions between methanol and PLs provides denser packing of methanol molecules around PL bilayers, thus allowing each bilayer to be apart to form a stable single-bilayered structure. At higher PL concentrations, as shown in Figure 5.3, B', bilayers pack closer, thus leading to double-bilayered structures. In contrast, PL bilayers in ethanol/water form multi-bilayers due to significantly weaker interactions between ethanol and PL, as is depicted in Figure 5.3, C' and C''.

The magnetite phases of inner and outer layer thicknesses of magnetic nanotubes can also be altered by varying concentration levels of the reactive species. Figure 5.4, Images A-D, illustrate morphologies of nanotubes produced by changing the PL/Fe²⁺/H₂O₂ molar ratios from 1:20:20, 1:40:40, 1:60:60, to 1:80:80 after the redox reactions, respectively. Figure 5.4, Images A'-D', demonstrate the respective nanotubes annealed at 550 °C. As seen in Images A-D, the increasing concentrations of the reactive species result in the greater amorphous iron oxide layer thickness which changes from 12 to 45 nm. The variable thickness results from the ionic interactions between the phosphate groups of PL and precursors.

The kinetic studies indicated that the formation of DC_{8,9}PC nanotubes occurs through a reversible first-order phase transition from a disordered chain-melted L_α phase (multilamellar vesicles) to the ordered chain-frozen L_β' phase, where the cooling rate determines the length of the nanotube.²⁷ Upon cooling through the phase transition temperature, bilayer ribbons form an intermediate, which spontaneously twist into helices due to the chirality, followed by continuous growth to form nanotubes. The slower cooling rate allows ribbons to have greater growth time to form longer nanotubes. However, as the brittle PL nanotubes are easily damaged upon agitation during the

synthesis of FMNT, the control of their length by varying the cooling rate is often hard to achieve. In view of these considerations, we have chosen an alternative solution in which the nanotubes were extruded through a porous polycarbonate membrane, thus facilitating the length alternation by mechanical force. Figure 5.5, A-A' and B-B', illustrate SEM images of FMNT extruded through a 3 μm membrane without and with the presence of magnetic field parallel to the membrane, respectively. As seen in Figure 5.5, A and A', FMNTs after passing through a 3 μm membrane exhibit average length of 10 μm . In contrast, upon applying parallel magnetic field (Figure 5.5, B and B'), a uniform length of 3 μm is obtained. Since the long axis of FMNTs are aligned parallel to the pores of the membrane along the magnetic field direction, when FMNTs are forced to pass through the 3 μm pores, the lengths of nanotubes are split into a 3 μm size same as the membrane pore size. Thus, the combination of extrusion through a porous membrane and the magnetic field provides the ability to control the length of FMNTs and various lengths can be further obtained by changing the pore size of membranes.

It is well established that the formation of DC_{8,9}PC tubular structures is attributed to the chirality of the PL bilayers which leads to unparallel packing, and consequently the tilting of the molecules with regard to their neighbours.¹⁵ As a result of the chirality, diameter changes of PL nanotubes can be obtained when altering the magnitude of the chirality by incorporating saturated phospholipid spacers into DC_{8,9}PC templates.²⁴ Figure 5.6, A, B and C reveal nanotube morphologies prepared from 1,2-dinonanoyl-sn-glycero-3-phosphocholine (DC₇PC)/DC_{8,9}PC, 1,2-diundecanoyl-sn-glycero-3-phosphocholine (DC₉PC)/DC_{8,9}PC, and DC_{8,9}PC phospholipids and show that the nanotube diameter varies from 50, 70 to 500 nm, respectively.

As indicated earlier, magnetite layer thickness changes have a significant effect on nanotube magnetization properties. Figure 5.7, Traces A-D, manifest the hysteresis loops of nanotubes with various magnetite layer thicknesses ranging from 12-45 nm, as shown in Figure 5.4, A'-D'. The significant increase of the saturation magnetizations (M_s) for Traces A, B, C to D are detected, with the M_s values ranging from 40, 43, 63, and 79 emu/g. This is the result of the increased magnetite amount with respect to the carbon phase. In addition, the remanent magnetization (M_r) shown in Traces B, C and D with the M_r values at about 8 emu/g slightly increases with respect to Trace A with a M_r value at 2 emu/g. The coercivity (H_c) illustrated in Trace B, C and D with the H_c values at about 145 Oe also slightly increases with regard to Trace A with a H_c value of 27 Oe.

Two equilibrium magnetization states for magnetic nanotubes have been identified as a uniform state with all the magnetic moments parallel to the tube axis and a flux-closure vortex state, where the geometry of nanotubes has a significant influence.¹⁷⁻²⁰ The geometry parameter β is equal to the ratio of internal to external radius of a nanotube and a vortex state were found to be maximized with the β value of 0.546, while the vortex state decreases away from this value.¹⁷ The average β values for the external and internal magnetite layer of FMNT are 0.9 and 0.93, respectively. Thus, a parallel magnetization state is preferred for FMNTs, where β values are far away from maximum value for vortex state. Furthermore, the length and the aspect ratio of nanotube were also found to affect their evolution in external magnetic field. Usov et al revealed that for the nanotubes with the aspect ratio < 20 , the vortex state dominates at the ends of tubes and propagates toward the middle of the nanotube, and for nanotubes with the aspect ratio of 70-100, the propagation of head-to-head domain wall along the nanotube length was

found during the magnetization reversal process.²⁰ The diameter of FMNT is approximately 500 nm and due to controllable lengths ranging from 5 to 40 μm , the aspect ratio of FMNTs varies from 10-80. Based on the theory, FMNTs with the aspect ratio ranging from 10-20 may exhibit a dominant vortex state at the end, and FMNTs with the larger aspect ratio from 70-80 may show a parallel magnetization state, while both vortex and parallel states could be found for FMNTs with the medium aspect ratio from 20-70.

Due to ferromagnetic properties, FMNT can be aligned directionally, which provides opportunities for creating composites with desirable magnetic properties. FMNT/polyester nanocomposites were prepared and the alternating alignment of FMNT in the matrix were obtained by a two-step process, where the magnetic field direction were 0° and 90° with respect to the film long axis in two steps, respectively. While Figure 5.8, A, demonstrates a schematic diagram of alternating alignments of two layers, Figure 5.8, B illustrates SEM images of the cross-section of resulting films revealing a two-layered distinguished morphologies with detailed morphologies shown in Figure 5.8, B1 and B2 . As seen in Image B1, FMNTs are stable and well dispersed in the polymer matrix and all nanotubes are parallel to the specimen long axis which is parallel to the magnetic field direction. In contrast, as seen in Image B2, no nanotubes are observed, but as anticipated a number of holes resulting from the open ends of FMNTs are observed, which is due to the FMNT alignment at 90° direction with respect to the magnetic field. For reference purpose, Figure 5.8, C, shows a SEM image of a cross-section of FMNT/polyester composite in the absence of magnetic field, where random orientation of FMNTs are observed. These data demonstrated that using alternating magnetic field

direction a two-layered films containing alternating alignment of FMNTs were prepared and using such approach a number of desirable alignments of FMNTs can be obtained by simply varying the magnetic field directions.

Conclusions

These studies illustrated a new approach to achieve controllable diameter, wall thickness, and length of FMNTs. Changing concentration and solvent environments, the thicknesses of the carbon layers were altered from 6, 10 to 50 nm, respectively. Also, changing synthetic conditions the thicknesses of magnetite layers ranging from 12 to 45 nm was obtained. The lengths of FMNTs were controlled by extrusion through a porous polycarbonate membrane under a parallel magnetic field. The diameter changes of nanotubes were obtained by incorporating saturated phospholipid spacers such as DC₇PC and DC₉PC into PL templates, where diameters of nanotubes were 50 and 70 nm, respectively. As well, their magnetic properties can be varied by changing the thickness of magnetite layers and geometries. The saturation magnetizations are found with values ranging from 40, 43, 63, and 79 emu/g by increasing magnetite layer thickness from 12 to 45 nm. The geometry parameter β which is the ratio of internal to external radius of a nanotube for the external and internal magnetite layer of FMNT are around 0.9 and 0.93, respectively, and a parallel magnetization state is preferred for FMNTs. In view of the lengths and aspect ratios of FMNTs, which were found to affect their evolution in external magnetic field, the aspect ratios of FMNTs varied ranging from 10-80, and a parallel magnetization or a vortex state were obtained as a result of aspect ratio changes. In addition, by alternating magnetic field direction, the preparation of FMNTs/polyester nanocomposites containing alternating alignment of FMNTs was demonstrated.

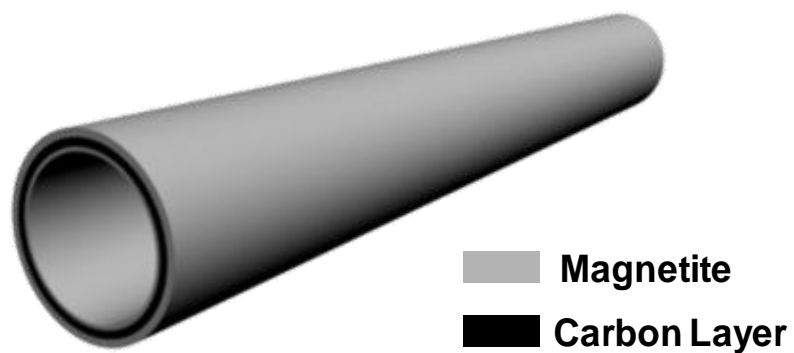


Figure 5.1. Schematic diagram of FMNT, which is a concentric magnetite nanotube separated by a carbon sheet concentric layer.

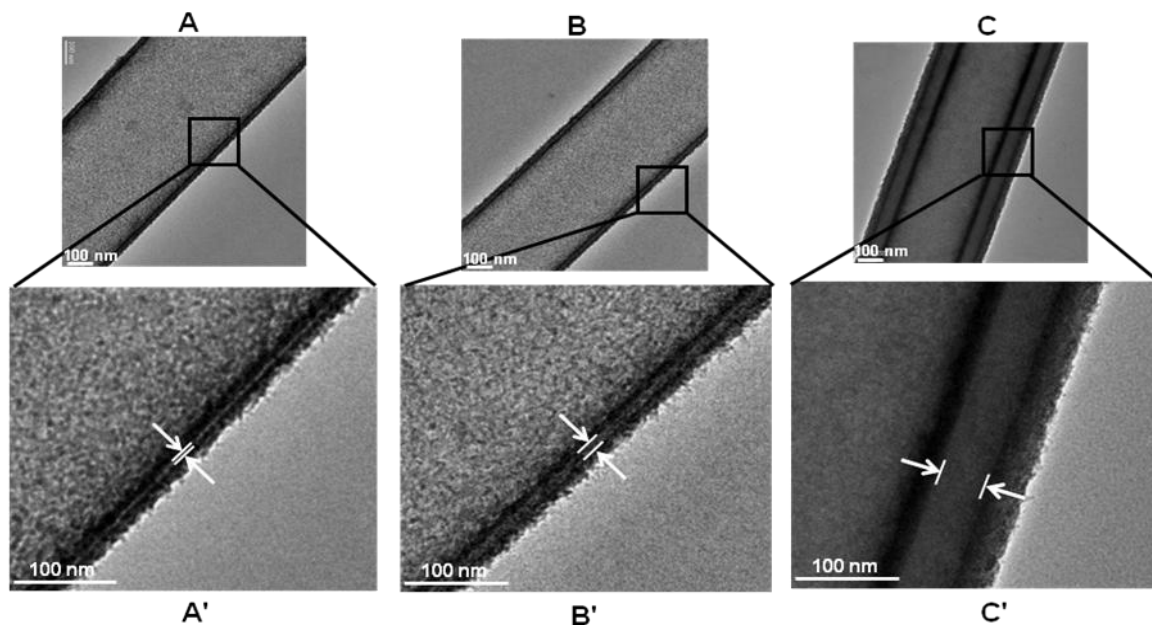


Figure 5.2. TEM images of nanotubes prepared from: (A) 2 mg/mL PL in 85/15 methanol/water; (B) 5 mg/mL PL in 85/15 methanol/water; (C) 2 mg/mL PL in 70/30 ethanol/water. Each enlarged image is shown in A', B' and C'. Respective thickness of carbon layers are: 6 nm (A), 10 nm (B), and 50 nm (C).

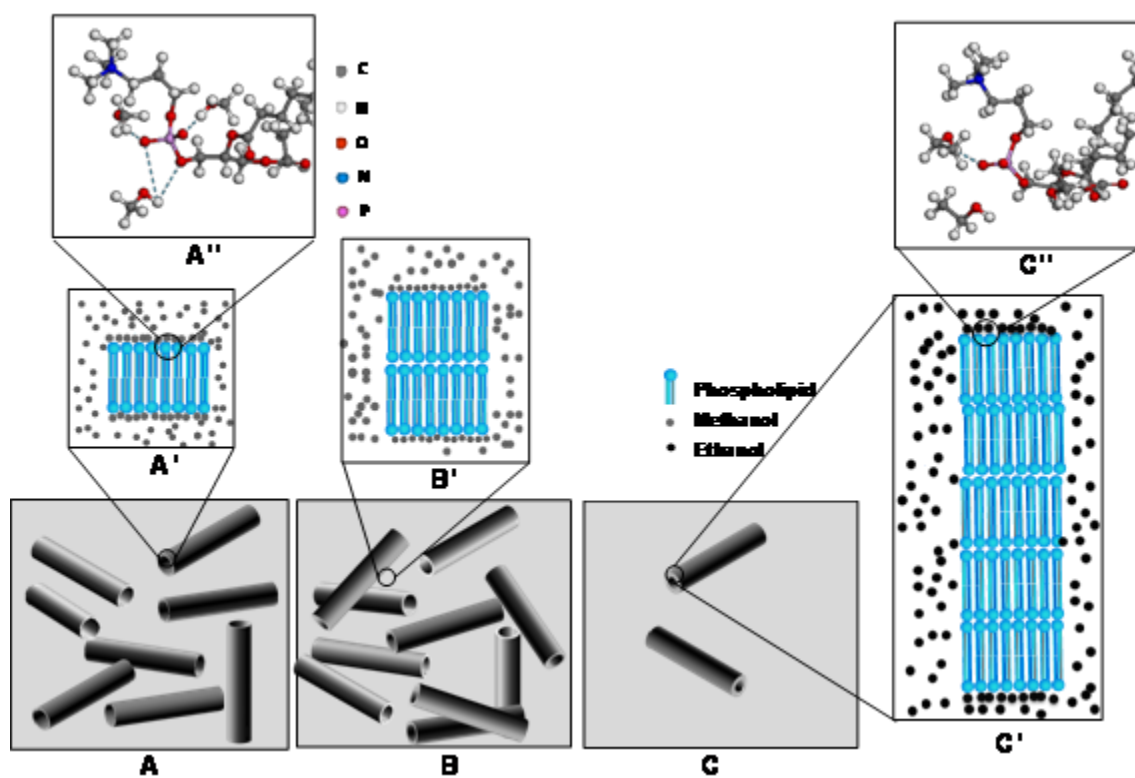


Figure 5.3. Schematic diagram of nanotubes prepared from (A) 2 mg/mL PL in methanol/water; (B) 5 mg/mL PL in methanol/water; (C) 2 mg/mL PL in ethanol/water. Images A', B' and C' illustrate interactions between PL and solvents, respectively. A'' and C'' show the H-bonding interactions between PL and methanol as well as PL and ethanol.

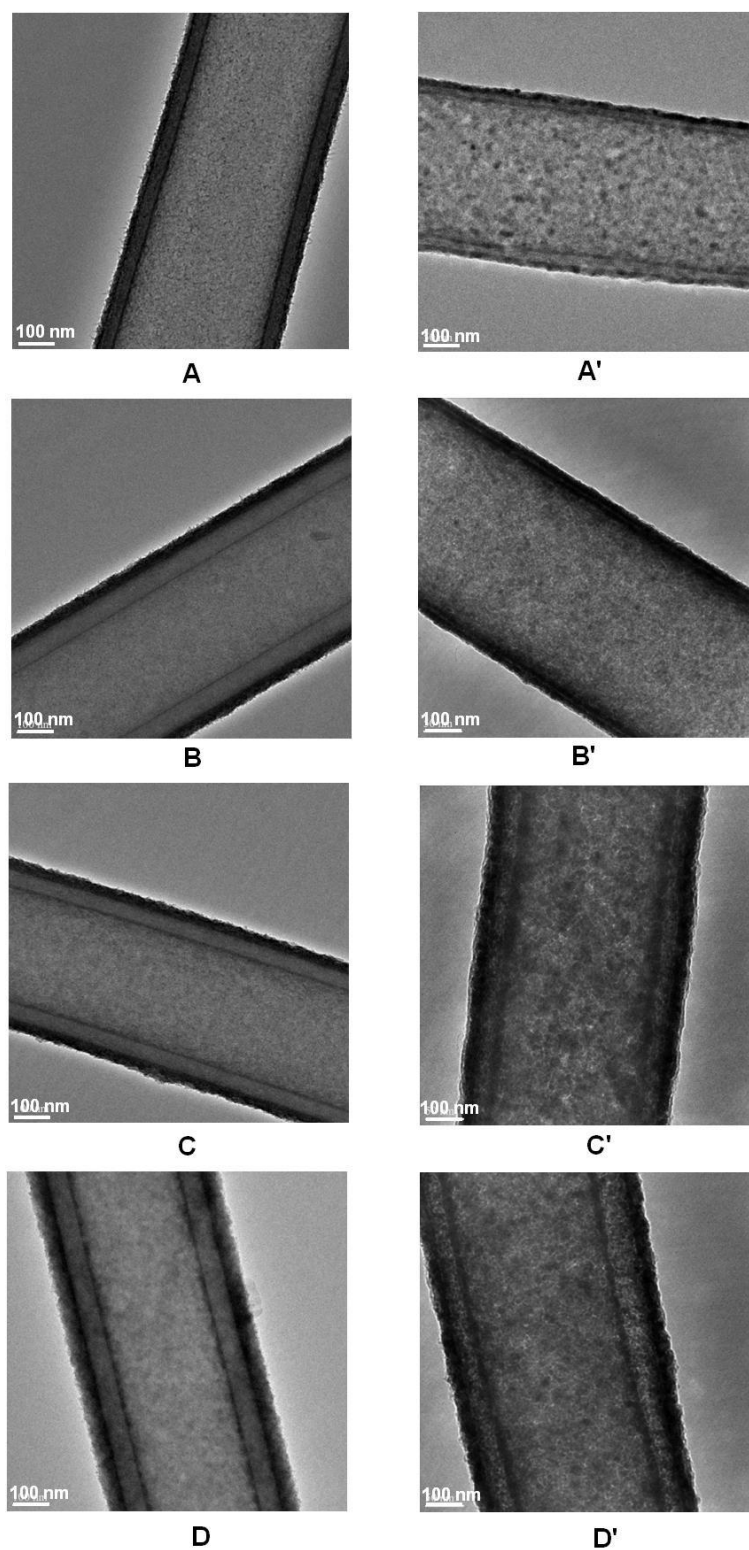


Figure 5.4. TEM images of nanotubes prepared with various PL: Fe^{2+} : H_2O_2 molar ratios of (A) 1:20:20; (B) 1:40:40; (C) 1:60:60; and (D) 1:80:80; Images A', B', C', and D' illustrate corresponding nanotubes after further annealing at 550 °C.

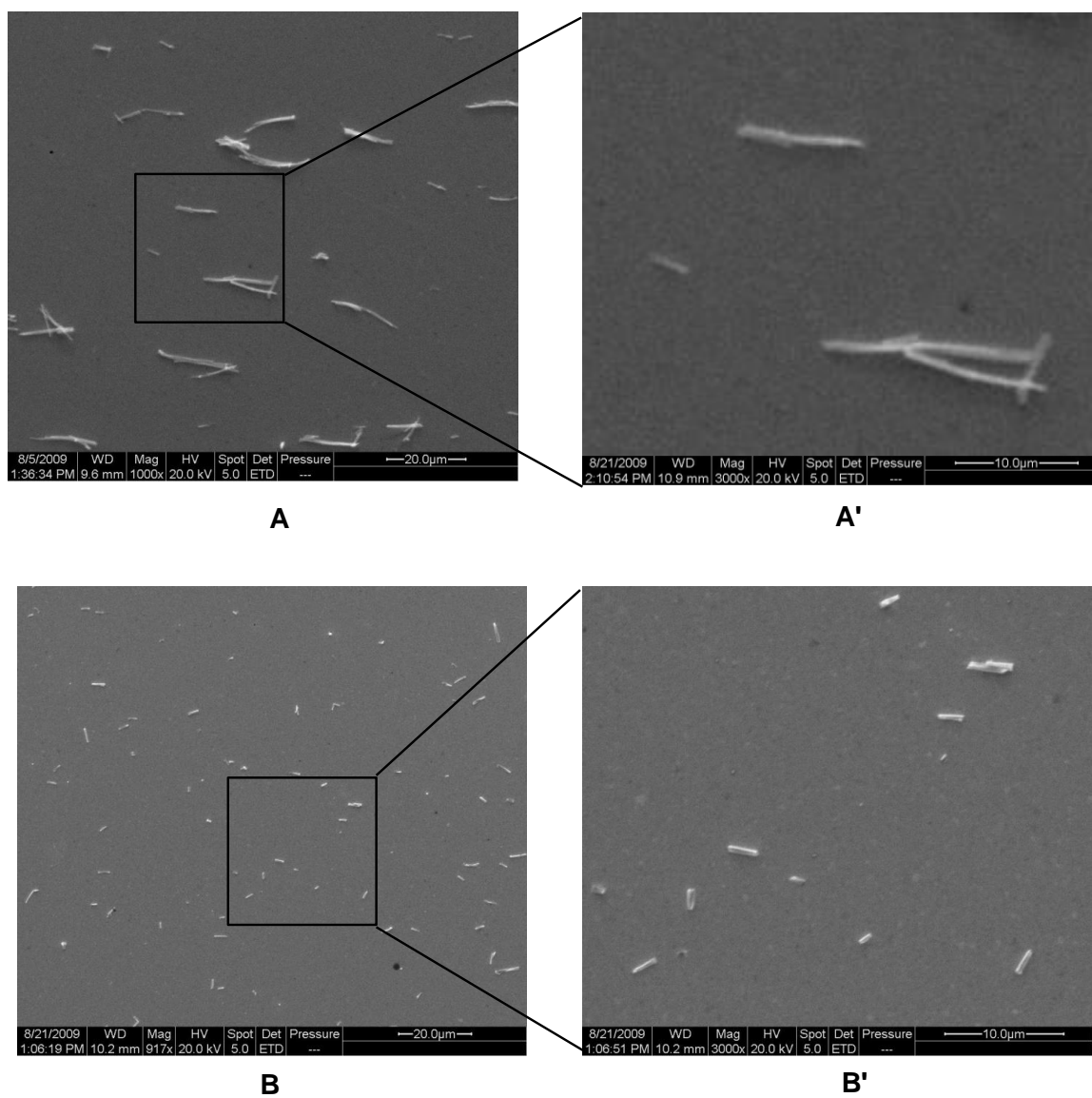


Figure 5.5. SEM images of FMNTs extruded through a 3 μm polycarbonate membrane without magnetic field (A) and (A'), and within magnetic field paralleling to the membrane (B) and (B').

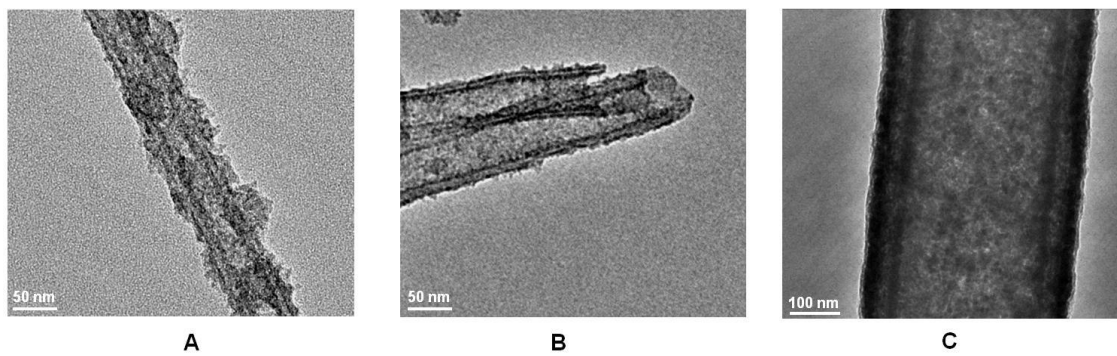


Figure 5.6. TEM images of nanotubes prepared from (A) DC₇PC/DC_{8,9}PC, (B) DC₉PC/DC_{8,9}PC, and (C) DC_{8,9}PC.

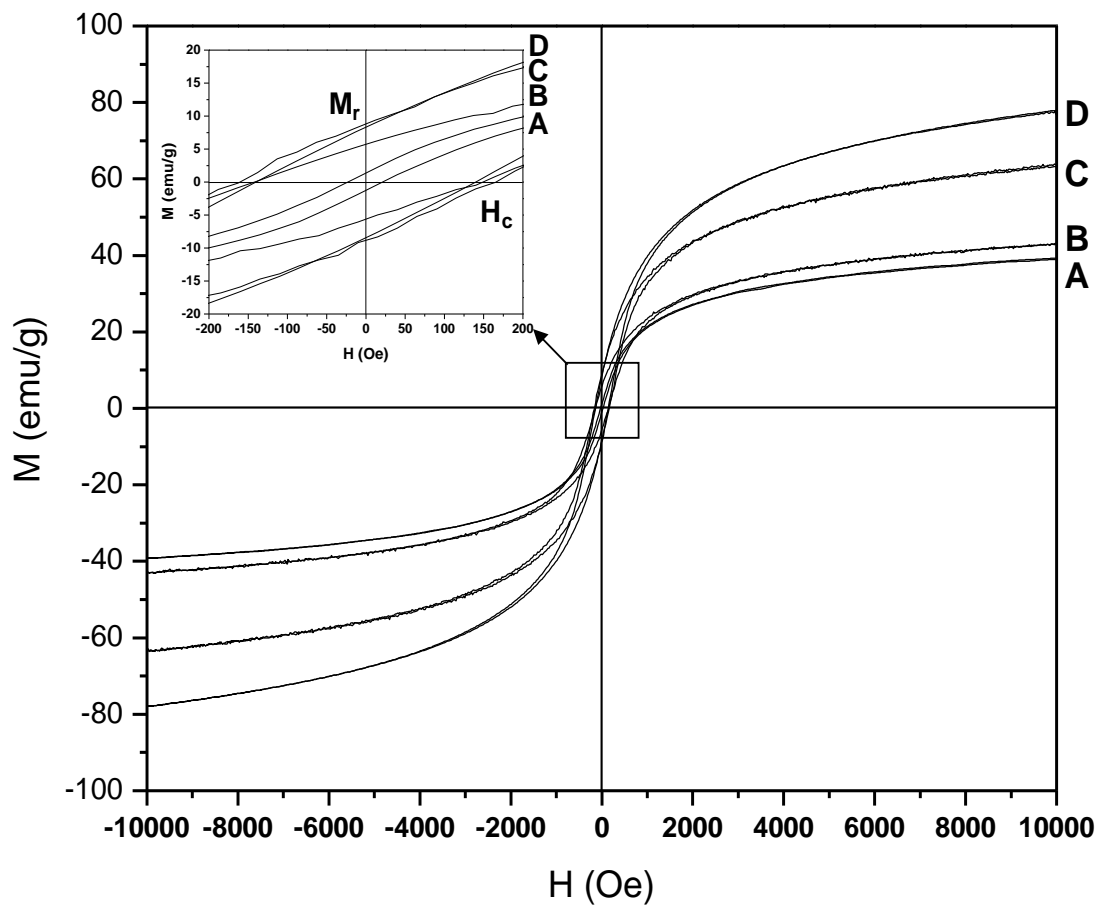


Figure 5.7. Magnetic hysteresis loops of FMNTs prepared with various PL: Fe^{2+} : H_2O_2 molar ratios of (A) 1:20:20; (B) 1:40:40; (C) 1:60:60; and (D) 1:80:80, which have increasing thickness of magnetite layers from 12 to 45 nm.

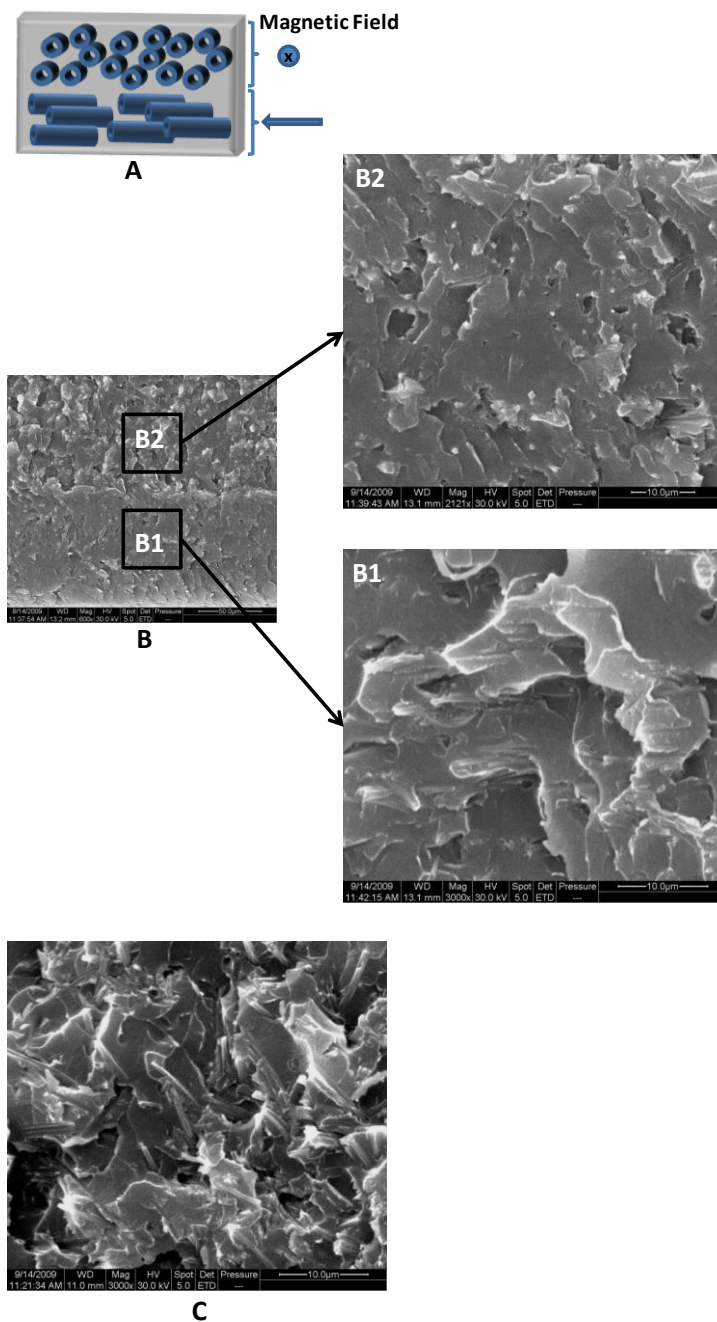


Figure 5.8. A. Schematic diagram of FMNT alternating alignment in polyester in the presence of magnetic field; B. SEM images of FMNT alternating alignment in polyester and enlarged images shown in B1 and B2; C. SEM image of FMNT in polyester without the presence of magnetic field.

References

- (1) Son, S. J.; Reichel, J.; He, B.; Schuchman, M.; Lee, S. B. *J. Am. Chem. Soc.* **2005**, *127*, 7316.
- (2) Ma, H.; Tarr, J.; DeCoster, M. A.; McNamara, J.; Caruntu, D.; Chen, J. F.; O'Connor, C. J.; Zhou, W. L. *J. Appl. Phys.* **2009**, *105*, 07B309.
- (3) Nielsch, K.; Castano, F. J.; Matthias, S.; Lee, W.; Ross, C. A. *Adv. Eng. Mater.* **2005**, *7*, 217.
- (4) Daub, M.; Knez, M.; Goesele, U.; Nielsch, K. *J. Appl. Phys.* **2007**, *101*, 09J111.
- (5) Sui, Y. C.; Skomski, R.; Sorge, K. D.; Sellmyer, D. J. *J. Appl. Phys.* **2004**, *95*, 7151.
- (6) Suber, L.; Imperatori, P.; Ausanio, G.; Fabbri, F.; Hofmeister, H. *J. Phys. Chem. B* **2005**, *109*, 7103.
- (7) Li, F.; Song, L. J.; Zhou, D.; Wang, T.; Wang, Y.; Wang, H. B. *J. Mater. Sci.* **2007**, *42*, 7214.
- (8) Ko, S.; Jang, J. *Angew. Chem. Int. Ed.* **2006**, *45*, 7564.
- (9) Lee, D.; Cohen, R. E.; Rubner, M. F. *Langmuir* **2007**, *23*, 123.
- (10) He, Q.; Tian, Y.; Cui, Y.; Mohwald, H.; Li, J. B. *J. Mater. Chem.* **2008**, *18*, 748.
- (11) Liu, Z. Q.; Zhang, D. H.; Han, S.; Li, C.; Lei, B.; Lu, W. G.; Fang, J. Y.; Zhou, C. W. *J. Am. Chem. Soc.* **2004**, *127*, 6.
- (12) Shenton, W.; Douglas, T.; Young, M.; Stubbs, G.; Mann, S. *Adv. Mater.* **1999**, *11*, 253.
- (13) Banerjee, I. A.; Yu, L. T.; Shima, M.; Yoshino, T.; Takeyama, H.; Matsunaga, T.; Matsui, H. *Adv. Mater.* **2005**, *17*, 1128.
- (14) Lv, B. L.; Xu, Y.; Wu, D.; Sun, Y. H. *Particuology* **2008**, *6*, 334.

- (15) Schnui, J. M. *Science* **1993**, 262, 1669.
- (16) Yu, M.; Urban, M. W. *J. Mater. Chem.* **2007**, 17, 4644.
- (17) Escrig, J.; Landeros, P.; Altbir, D.; Vogel, E. E.; Vargas, P. *J. Magn. Magn. Mater.* **2007**, 308, 233.
- (18) Escrig, J.; Altbir, D.; Nielsch, K. *Nanotechnology* **2007**, 18, 225704.
- (19) Konstantinova, E. *J. Magn. Magn. Mater.* **2008**, 320, 2721.
- (20) Usov, N. A.; Zhukov, A.; Gonzalez, J. *J. Magn. Magn. Mater.* **2007**, 316, 255.
- (21) Chen, A. P.; Usov, N. A.; Blanco, J. M.; Gonzalez, J. *J. Magn. Magn. Mater.* **2007**, 316, e317.
- (22) Landeros, P.; Suarez, Q. J.; Cuchillo, A.; Vargas, P. *Phys. Rev.* **2009**, 79, 024404.
- (23) Yager, P.; Schoen, P. E. *Mol. Cryst. Liq. Cryst.* **1984**, 106, 371-381.
- (24) Singh, A.; Wong, E. M.; Schnui, J. M. *Langmuir* **2003**, 19, 1888.
- (25) Ratna, B. R.; Baral-Tosh, S.; Kahn, B.; Schnui, J. M.; Rudolph, A. S. *Chem. Phys. Lipids* **1992**, 63, 47.
- (26) Brandrup, J.; Immergut, E. H. *Polymer Handbook*; John Wiley & Sons, Inc: New York, 1974.
- (27) Thomas, B. N.; Safinya, C. R.; Plano, R. J.; Clark, N. A. *Science* **1995**, 267, 1635.

CHAPTER VI

FORMATION OF ANTIBACTERIAL SURFACES ON CARBON BASED
NANOMATERIALS: THE EFFECT OF ANTIBIOTICS ON CYTOTOXICITY

Introduction

Recent studies examined carbon nanotubes and C₆₀ interactions with living cells or other biosystems, and revealed that this is a complex process. It appears that cytotoxicity of carbon nanotubes and C₆₀ is more complex than anticipated and size,^{1,2} shape,^{3,4} and surface functionalization^{5,6} have been attributed to their non-conclusive toxic behavior.⁷⁻¹⁰ Aside from cytotoxicity, even test methods^{11,12} raised some questions, but most studies conducted on nanotubes, and to some extent on C₆₀, agreed that these materials exhibit antimicrobial properties.^{2,10,13} For example, highly purified single-walled and multi-walled carbon nanotubes were found to show antimicrobial activity against *Escherichia coli* (*E. coli*) and their cytotoxicity resulted from a direct contact with the bacterial cell membranes, causing the severe cell membrane damage.^{2,10}

Regardless of the mechanisms of cytotoxicity and antimicrobial activity, size and shape of nano-objects may play an important role which is often difficult or even impossible to control. One approach to minimize geometrical considerations is to chemically modify surfaces of nano-objects and allow surface chemistry overcome cytotoxicity and antimicrobial properties. One of the useful surface modifications are microwave plasma reactions, which are fast and maintain the bulk properties as well as require no volatile solvents. Furthermore, the plasma reactions in the presence of suitable monomers such as maleic anhydride are able to produce acid groups which highly desirable for further reactions. Using this approach, poly(dimethylsiloxane) (PDMS),^{14,15}

poly(vinylidene fluoride) (PVDF)¹⁶ and poly (tetrafluoroethylene) (PTFE)^{17,18} were effectively modified, this allowing further surface reactions. Carbon nanotubes have been modified using radio-frequency or microwave plasma reactions,¹⁹⁻²⁴ but the primary purpose of these studies was to enhance dispersibility of multi-wall carbon nanotubes (MWNT) and mechanical properties of epoxy composites.¹⁹

Due to many potential applications in biomedical technologies and considering the fact that the bacterial growth on surfaces of various materials often results in detrimental infections, these studies examine the effectiveness of surface reactions of C₆₀, MWNT, nano-carbon fibers, and ferromagnetic nanotubes (FMNT)²⁵ against microbial film formation as well as cytotoxicity.

Experimental

MWNT, nano-carbon fiber, C₆₀, maleic anhydride (MA), polyethylene glycol (PEG) (MW 200 and 600), and penicillin V (PEN), thionyl chloride (SOCl₂), triethylamine, 4-(dimethylamino)-pyridine (DMAP) and N,N'-dicyclohexylcarbodiimide (DCC) were purchased from Aldrich Chemical Co. FMNTs were prepared from DC_{8,9}PC nanotubes, which have been previously reported.²⁵ C₆₀ MWCN, nano-carbon fiber, and FMNT samples were dispersed in chloroform and spread on a glass slide, which was allowed to dry overnight.

The process of surface modification of FMNT is shown in Figure 6.1 and C₆₀, MWNT, and nano-carbon fiber followed the same reaction procedure. In step 1, the glass slide containing FMNTs and 100 mg of solid maleic anhydride which were separated 8.5 cm apart were placed into a microwave reactor chamber. Plasma reactions were performed using open reactor conditions, as described elsewhere.^{14,18} In a typical

experiment, the reactor was evacuated to 150 mTorr, followed by purging it with Ar gas in order to obtain a steady-state pressure of 250 mTorr at a flow rate of 2.96 mL/min. Then, plasma formation occurred when applying microwave radiation at 600 W of power with an output frequency of 2.45 GHz. Under these conditions, the reaction chamber pressure increased continuously during the microwave plasma discharge. In an attempt to keep plasma environment during longer exposure times, a vacuum was applied continuously to maintain pressure conditions during the experiment. After plasma reactions, the sample was hydrolyzed in water for 30 min in order to generate carboxylic acid groups as well as remove excess and physisorbed MA on the sample as monomeric and polymeric forms of MA are soluble in water, and then stored in a desiccator under ambient conditions.

In step 2, in an attempt to facilitate esterification reactions, carboxylic acid groups were converted to carboxylic chloride groups in the presence of thionyl chloride under reflux conditions at 65 °C for 6 h. Then, the sample was washed using chloroform to eliminate excess thionyl chloride. The esterification reactions between the samples and PEG containing a 1:1 molar ratio of linear PEG with molecular weight=200 and 600 were employed in chloroform at room temperature for 18 h. A small amount (1-2 drops) of triethylamine was introduced into the reaction in the beginning of the reaction in order to neutralize hydrochloric acid that was produced during the reaction. The sample was washed with chloroform to remove excess PEG, followed by using distilled water for 30 min.

In an effort to chemically bond PEN onto the samples, an esterification reaction using DMAP catalyst and DCC coupling agent were utilized, as shown in step 3.²⁶ The K

salt of PEN (1.5 mmol) was dissolved in a small amount of water, cooled, and acidified with 0.1 M HCl. Then, precipitated PEN was filtered and dried in a vacuum oven at room temperature for 1 h.²⁷ The specimen and DMAP (0.25 mmol) were placed into a 100 mL flask with 20 mL of methylene chloride, followed by addition of PEN during stirring and cooling in an ice-water bath. After adding DCC (1.3 mmol), the reaction occurred and the mixture was continuously stirred for 4 h. Final samples were washed in methylene chloride sequentially for 30 min, dried for 24 h for further analysis.

Morphologies of nanotubes were analyzed using a Jeol JEM-2100 transmission electron microscope (TEM) operated at 200 kV, in which samples were diluted and deposited on formvar/carbon coated copper grids. Attenuated total reflectance Fourier transform infrared (ATR FT-IR) spectroscopy measurements were performed using a Bio-Rad FTS-6000 FT-IR single-beam spectrometer with 4 cm^{-1} resolution. The surfaces were analyzed using a 2 mm Ge crystal with a 45° angle maintaining constant contact pressure between the crystal and the specimens. All spectra were corrected for spectral distortions using software for the Urban-Huang algorithm.²⁸ Quantitative ATR FT-IR for each sample were performed and detailed regarding volume concentration measurement were described elsewhere.¹⁵ The extinction coefficient for 1728 , 1105 , 1780 cm^{-1} due to COOH, PEG, and PEN, respectively, were previously determined to be 544.32 ,¹⁶ 944.68 ,²⁹ 778.58 L/mol cm .²⁹ Using double Kramers-Kronig transformation (KKT) and previously developed algorithm for quantitative analysis employing ATR FT-IR spectroscopy,²⁸ volume concentration levels for each step were determined.

The antimicrobial activities of samples were analyzed. *Staphylococcus aureus* (RN 6390) were allowed to grow overnight in Luria-Bertani (LB) broth, and agar (0.7%)

was melted and mixed with LB broth, followed by addition of 50 μ L of staphylococcus aureus. This culture was spread over agar plates containing specimens, which were incubated for 16 h at 37 °C. In order to examine cytotoxicity of specimens, mouse embryonic stem cells were grown on cover glasses coated with specimens, which was cultured for 3 days and then stained with TB.

Results and Discussion

As stated in the Introduction, these studies focus on the modification of nano-objects to create chemically controlled antimicrobial activity as cytotoxicity. The general approach is illustrated in Figure 6.1 for a single FMNT, but the sequence of reactions 1 through 3 will be the applicable for C₆₀, MWNT, and nano-carbon fiber. As illustrated in Figure 6.1, Step 1, COOH were created on the surface using surface microwave plasma conditions in the presence of maleic anhydride, followed by surface hydrolysis.^{14,18} The advantage of having COOH groups on a surface is that other OH-containing species can be further reacted. However, it is first desirable to convert COOH to COOCl in the presence of SOCl₂ (Step 2) in order to facilitate easier reactions with hydroxyl groups, followed by the esterification reactions between COOCl and hydroxyl groups of PEG with 200 and 600 MW. The final Step 3 involves the esterification reactions of PEG-functionalized surfaces with PEN in the presence of DCC catalyst and DMAP coupling reagent. In order to increase antimicrobial activity of PEN, biocompatible PEG is introduced as a flexible spacer between surface and PEN. Using different length PEG facilitates molecular roughness resulting in the increased surface area ultimately leading to enhanced activity of PEN molecules against microbial film formation.

Figure 6.2 illustrates TEM images of C_{60} , MWNTs, nano-carbon fiber and FMNT before (A-D) and after (A'-D') the sequence of reactions shown in Figure 6.1. As seen in Figure 6.2, A', B', C', D' upon the PEN attachment, morphologies remain stable and increased wall thickness is observed. The increased thickness of PEN-MWNT and PEN-carbon fiber as shown in Figure 6.2, B' and C' are around 2 and 4.2 nm, respectively. However, as seen in Figure 6.2, D', the thickness of the layer of PEN-FMNT is not uniform and fluctuates between 6.5-9.5nm.

The same process was utilized to modify C_{60} , MWNTs, and carbon fibers. In order to analyze the extent of the surface reactions, ATR-FTIR spectra of C_{60} , MWNTs, carbon fibers, and FMNTs were recorded after each step shown in Figure 6.1. The results are shown in Figure 6.3, A, B, C and D. Figure 6.3.A, Traces A and B, illustrate the spectra of C_{60} before and after plasma reactions, respectively. As seen in Trace B, the bands at 1781 and 1728 cm^{-1} resulting from anhydride C=O and acid C-O stretching vibrations are detected, thus showing that C_{60} were chemically modified via a C=C bond opening of the maleic anhydride ring, followed by its hydrolysis. This is confirmed in Figure 6.3.A, Trace C, which illustrates IR spectrum with the bands at 1734 cm^{-1} due to C=O ester vibrations resulting from the esterification reaction. In the final step, PEN was attached to PEG-functionalized C_{60} , and Trace D illustrates the presence of the bands at 1648 , 1734 , and 1780 cm^{-1} resulting from amide, ester, and β -lactam C=O stretching vibrations, respectively, thus confirming the formation of PEN-PEG bands. The same data were collected on chemically modified MWNT, carbon fiber, and FMNT, which are illustrated in Figure 6.3, B, D, and D, and the presence of the same vibrational features

signify the attachment of PEN to carbon-based nanomaterials, and retention of the β -lactam ring remains intact during the reactions.

ATR FT-IR measurements provide a unique opportunity to quantitatively determine the extend of surface coverage, regardless of shape and size of a given object. This analysis requires the knowledge of the extinction coefficients of the 1728, 1105, 1780 cm^{-1} bands due to COOH, PEG, and PEN, respectively, which were previously determined to be 544.32,¹⁶ 944.68,²⁹ 778.58 L/mol cm .²⁹ Using this approach, the volume concentration of a given surface species can be quantitatively analyzed by using Beer-Lamber's law for ATR FT-IR analysis. Figure 6.4 illustrates COOH, PEG, and PEN volume concentration changes for C_{60} , MWNT, carbon fiber, and FMNT. As seen, COOH volume concentrations for FMNT after Step 1 in Figure 6.1 is highest with a value of $9.81 \times 10^{-4} \text{ mg/cm}^3$, which indicates that the iron oxide surface exhibits higher reactivity with MA in plasma reaction. The COOH volume concentrations for C_{60} , MWNT, and carbon fiber are 8.10×10^{-4} , 6.59×10^{-4} , and $3.75 \times 10^{-4} \text{ mg/cm}^3$, respectively. C_{60} exhibits higher volume concentration than MWNT and carbon fiber and similar tendency for their PEG and PEN volume concentrations were observed. Due to the overlap of the band at 1105 cm^{-1} resulting for PEG and the band of FMNT, volume concentration for PEG-FMNT were not calculated.

In an effort to examine antimicrobial activity of C_{60} , MWNT, carbon fiber, and FMNT upon PEN attachment, these specimens were exposed to gram-positive *staphylococcus aureus* bacteria. As controls, non-modified specimens were exposed to the same conditions and Figure 6.5, A, B, C, and D illustrate the results. As seen, Figure 6.5.A and 6.5.D of C_{60} and FMNT show the growth of bacteria. FMNT have iron oxide

outer layers which are not toxic for cells. However, Figure 6.5.B and 6.5.C of MWNT and carbon fiber indicate the slightly bacterial inhibition, which are consistent with the earlier reported.^{2,10,13} For example, multi-walled carbon nanotubes were reported to inhibit *Escherichia coli* (*E. coli*) cell growth resulting from a direct contact with bacterial cell membranes, thus causing the cell membrane damage and leakage.² In contrast, Figure 6.5, A', B', C', and D' demonstrate the antibacterial test of C₆₀, MWNT, carbon fiber, and FMNT after PEN reactions, which indicate the inhibition of bacterial growth around the specimen region resulting from the effectiveness of PEN against the bacterial. Compared with unmodified samples in Figure 6.5, A-D, samples with PEN surface modification illustrated in Figure 6.5, A'-D' exhibit enhanced and well-controlled antibacterial features, which demonstrates these carbon-based materials upon PEN modification are potentially utilized in biosystems.

The cytotoxicity of C₆₀, MWNT, carbon fiber, and FMNT were also examined and the specimens were exposed to partially differentiated mouse embryonic stem cells. Figure 6.6, A-D' illustrates the results of C₆₀, PEN-C₆₀, MWNT, PEN-MWNT, nano-carbon fiber, PEN-nano-carbon fiber, FMNT, and PEN-FMNT. The cell growth in all samples was observed using an optical microscope, where cells in all samples were intact and no apparent toxicity were observed. Figure 6.6, d and d' illustrate the optical micrograph of FMNT and PEN-FMNT. As seen in Figure A/A' and C/C', C₆₀ and PEN-C₆₀ as well as nano-carbon fiber and PEN-nano-carbon fiber show a very similar cell density around 0.9. It should be noted that due to the slightly detachment of cell during the washing process the cell number may vary within 0.1 experimental errors. In contrast, PEN-MWNT in Figure 6.6, B' shows a higher cell number (1.1) compared with MWNT

(0.86) in Figure 6.6, B. Although significant efforts have been made to study cytotoxicity of carbon nanotubes which may be attributed to size,^{1,2} shape,^{3,4} surface functionalizations,^{5,6} and even the choice of a test method,^{11,12} no apparent toxicity was observed for MWNT, as shown in Figure 6.6, B. The increased cell numbers of PEN-MWNT in Figure 6.6, B' elucidate the PEN attachments on MWNT offer a biocompatible environment and decrease the potential cytotoxicity. Similar observations were found in FMNT and PEN-FMNT, as shown in Figure 6.6, D and D', where a higher cell number (1.2) is obtained for PEN-FMNT compared with FMNT (0.9), thus demonstrating the cytotoxicity of FMNT upon PEN attachments significantly decreases. In view of above cytotoxic results, no apparent toxic effects were detected for these carbon-based materials, and significantly enhanced biocompatibility was obtained for PEN-MWNT and PEN-FMNT, thus manifesting the effectiveness of PEN on decreased cytotoxicity.

Conclusions

Antibiotics such as PEN were demonstrated to be functionalized onto surfaces of C₆₀, MWNTs, carbon fibers, and FMNTs. Upon surface modification with PEN through PEG spacer, these samples revealed highly effective and well-controlled anti-bacterial activity toward gram-positive *Staphylococcus aureus* bacteria. Furthermore, cytotoxic tests demonstrated no apparent toxic effect were found for all the samples, and significantly enhanced biocompatibility was obtained for PEN-MWNT and PEN-FMNT, thus manifesting the effectiveness of PEN attachments on decreasing cytotoxicity.

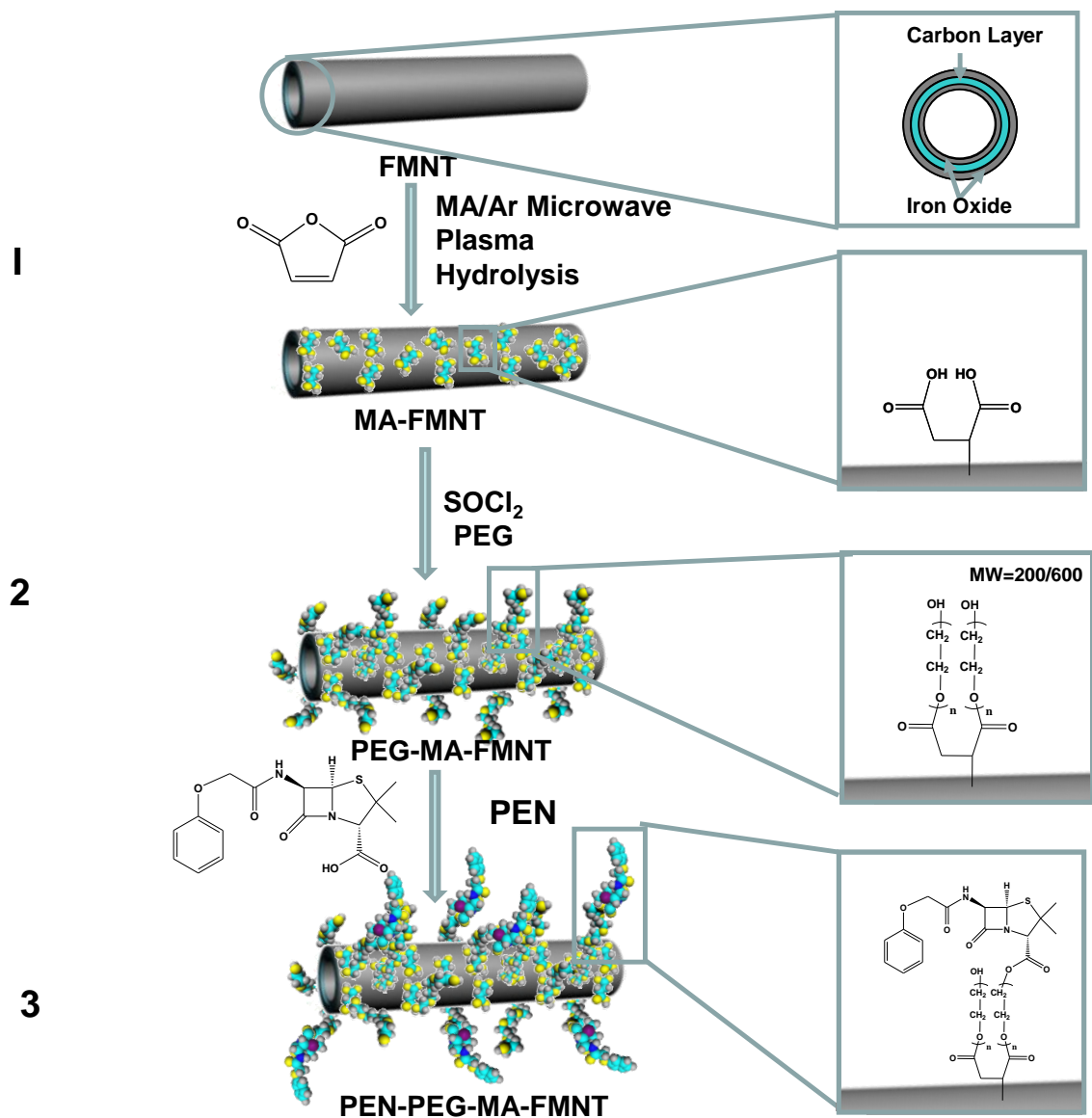


Figure 6.1. Schematic diagram of surface reactions on FMNTs: Step 1, Ar microwave plasma reaction and hydrolysis of MA-modified FMNTs; Step 2, conversion of acid group and PEG reaction; Step 3, PEN reaction.

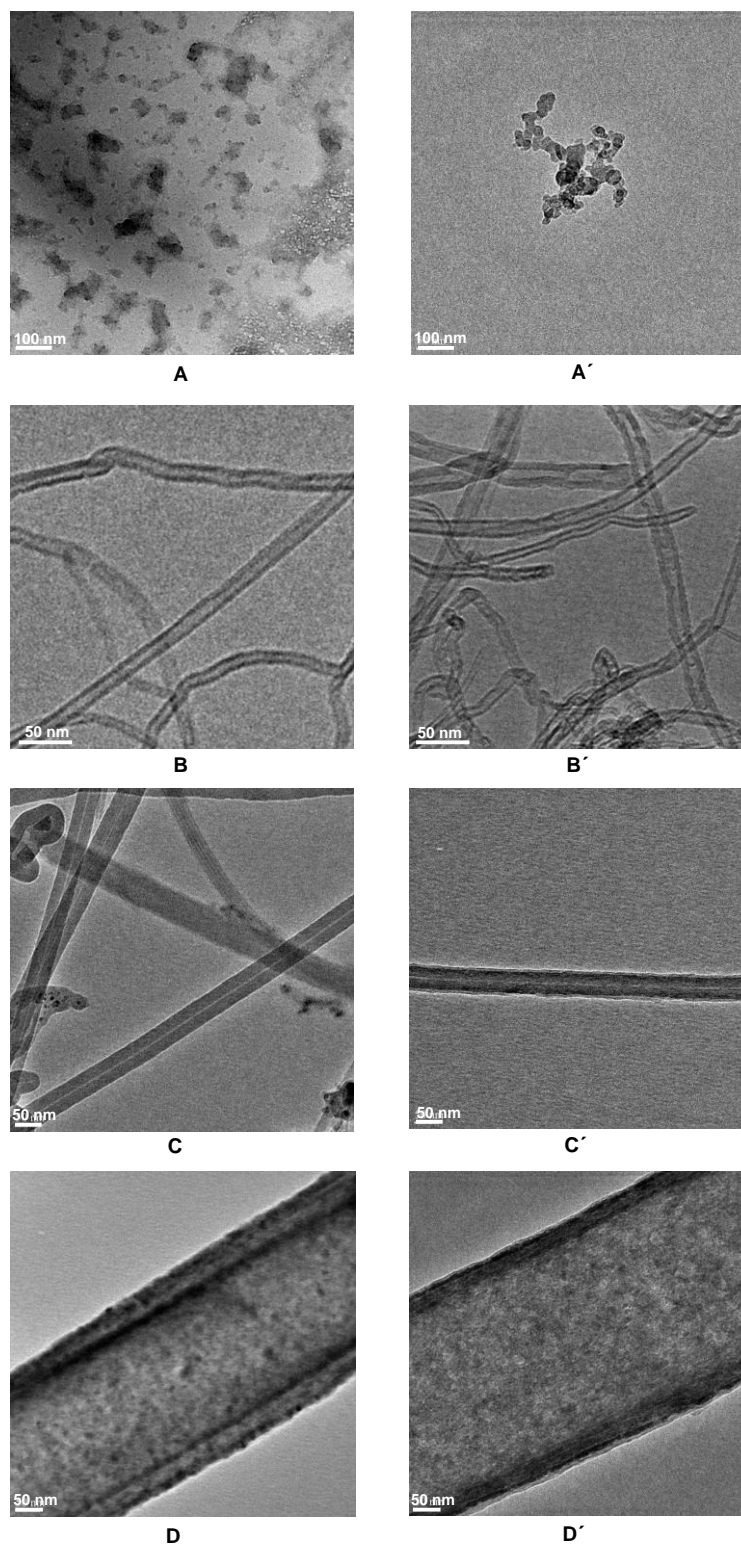


Figure 6.2. TEM images of (A) C_{60} ; (A') PEN-PEG-MA- C_{60} ; (B) MNCTs; (B') PEN-PEG-MA-MNCTs; (C) carbon fibers; (C') PEN-PEG-MA-carbon fibers; (D) FMNTs; (D') PEN-PEG-MA-FMNTs.

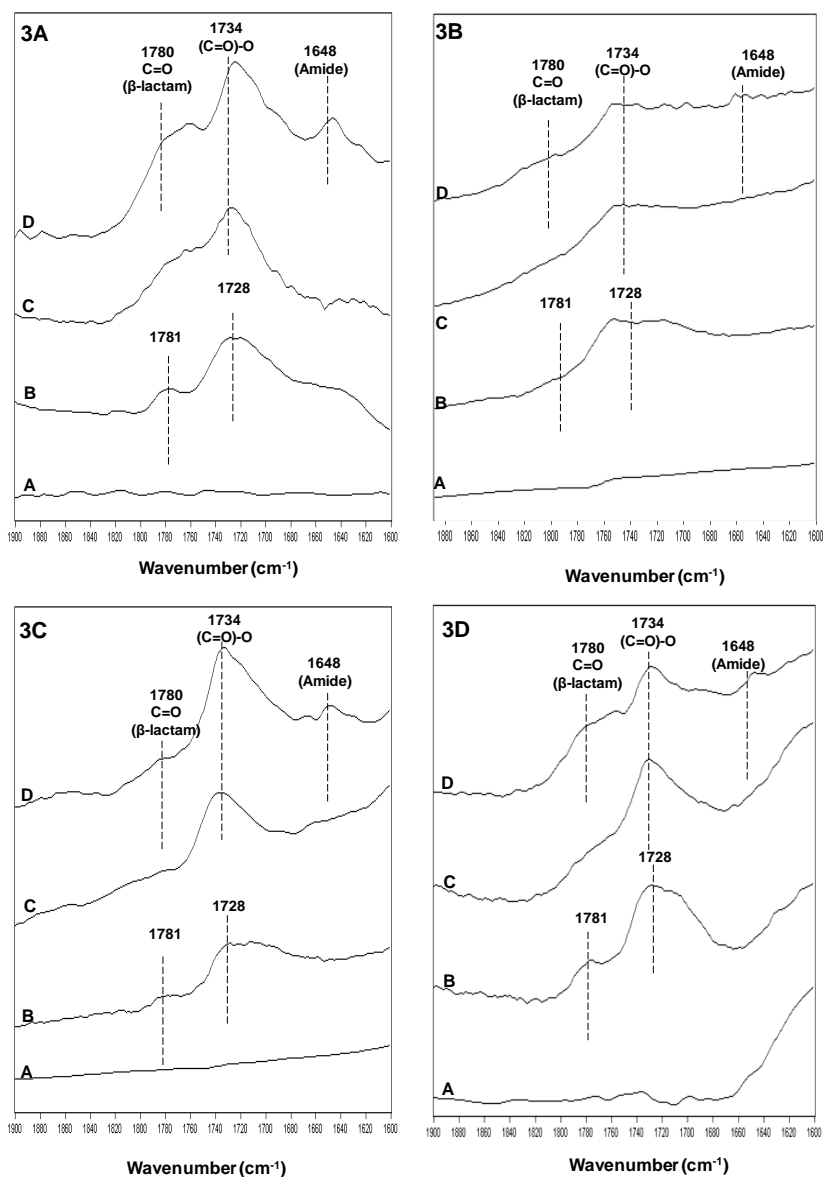


Figure 6.3. A. ATR FT-IR spectra of (A) C_{60} ; (B) MA- C_{60} ; (C) PEG-MA- C_{60} ; (D) PEN-PEG-MA- C_{60} . B. ATR FT-IR spectra of (A) MWNTs; (B) MA-MWNTs; (C) PEG-MA-MWNTs; (D) PEN-PEG-MA-MWNTs. C. ATR FT-IR spectra of (A) carbon fibers; (B) MA-carbon fibers; (C) PEG-MA-carbon fibers; (D) PEN-PEG-MA-carbon fibers. D. ATR FT-IR spectra of (A) FMNTs; (B) MA-FMNTs; (C) PEG-MA-FMNTs; (D) PEN-PEG-MA-FMNTs.

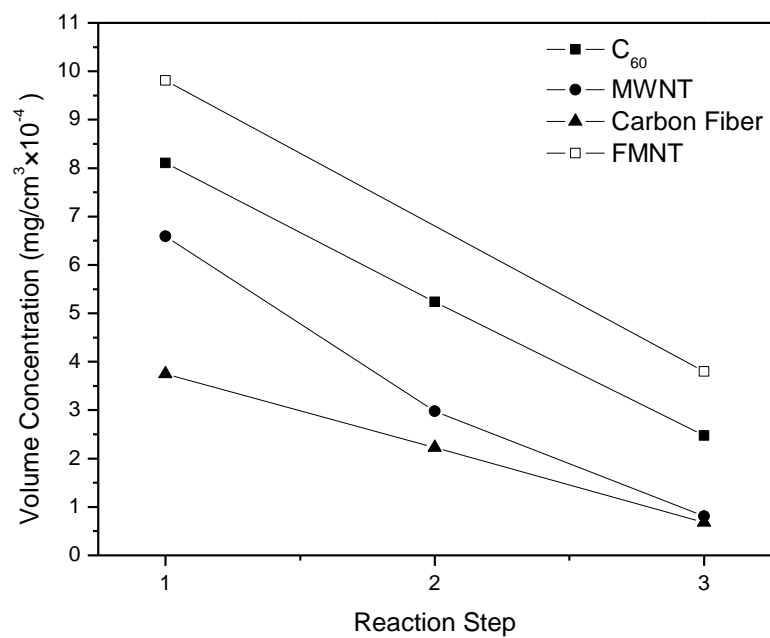


Figure 6.4. The volume concentration for C_{60} , MWNT, carbon fiber and FMNTs for each step.

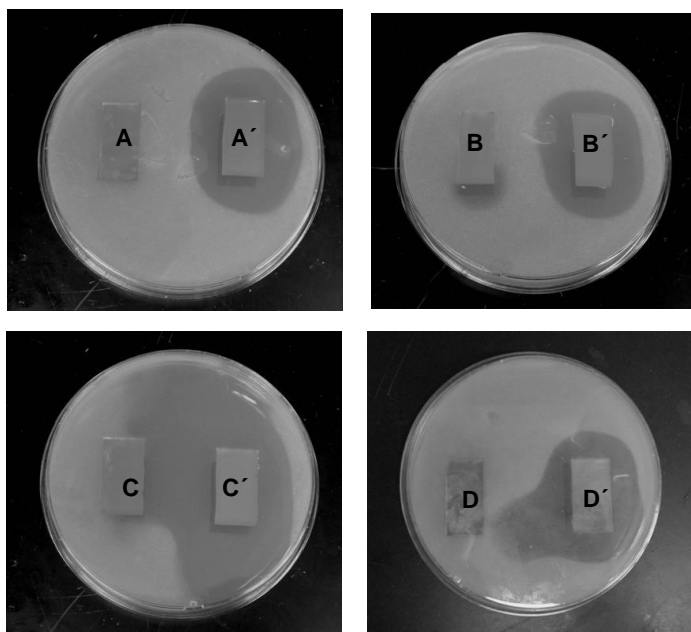


Figure 6.5. Photographs of agar plates containing (A) C_{60} ; (A') PEN-PEG-MA- C_{60} ; (B) MWNTs; (B') PEN-PEG-MA-MWNTs; (C) carbon fibers; (C') PEN-PEG-MA-carbon fibers; (D) FMNTs; and (D') PEN-PEG-MA-FMNTs in staphylococcus aureus cultures.

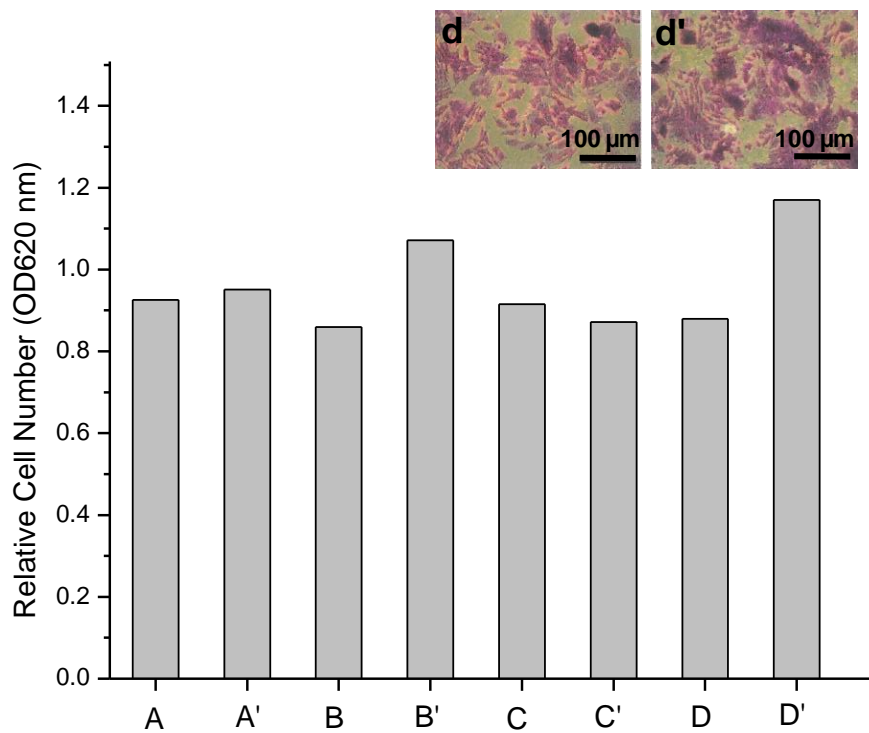


Figure 6.6. Cytotoxicity analysis of specimens: (A) C_{60} ; (A') PEN-PEG-MA- C_{60} ; (B) MNCTs; (B') PEN-PEG-MA-MNCTs; (C) carbon fibers; (C') PEN-PEG-MA-carbon fibers; (D) FMNTs; (D') PEN-PEG-MA-FMNTs; Optical images of cell growth on the specimens: (d) FMNTs; (d') PEN-PEG-MA-FMNTs.

References

- (1) Magrez, A.; Kasas, S.; Salicio, V.; Pasquier, N.; Seo, J. W.; Celio, M.; Catsicas, S.; Schwaller, B.; Forro, L. *Nano Lett.* **2006**, *6*, 1121.
- (2) Kang, S.; Herzberg, M.; Rodrigues, D. F.; Elimelech, M. *Langmuir* **2008**, *24*, 6409.
- (3) Jia, G.; Wang, H. F.; Yan, L.; Wang, X.; Pei, R. J.; Yan, T.; Zhao, Y. L.; Guo, X. *B. Environ. Sci. Technol.* **2005**, *39*, 1378.
- (4) Ding, Y. H.; Stilwell, J.; Zhang, T. T.; Elboudwarej, O.; Jiang, H. J.; Selegue, J. P.; Cooke, P. A.; Gray, J. W.; Chen, F. F. *Nano Lett.* **2005**, *5*, 2448.
- (5) Chen, X.; Tam, U. C.; Czapinski, J. L.; Lee, G. S.; Rabuka, D.; Zettl, A.; Bertozzi, C. R. *J. Am. Chem. Soc.* **2006**, *128*, 6292.
- (6) Dumortier, H.; Lacotte, S.; Pastorin, G.; Marega, R.; Wu, W.; Bonifazi, D.; Briand, J. P.; Prato, M.; Muller, S.; Bianco, A. *Nano Lett.* **2006**, *6*, 1522.
- (7) Manna, S. K.; Sarkar, S.; Barr, J.; Wise, K.; Barrera, E. V.; Jejelowo, O.; Rice-Ficht, A. C.; Ramesh, G. T. *Nano Lett.* **2005**, *5*, 1676.
- (8) Nel, A.; Xia, T.; Madler, L.; Li, N. *Science* **2006**, *311*, 622.
- (9) Pukansky, B.; Diabate, S.; Krug, H. F. *Toxicol. Lett.* **2007**, *168*, 58.
- (10) Kang, S.; Pinault, M.; Pfefferle, L.; Elimelech, M. *Langmuir* **2007**, *23*, 8670.
- (11) Worle-Knirsch, J. M.; Pulskamp, K.; Krug, H. F. *Nano Lett.* **2006**, *6*, 1261.
- (12) Zhu, Y.; Ran, T. C.; Li, Y. G.; Guo, J. X.; Li, W. X. *Nanotechnology* **2006**, *17*, 4668.
- (13) Nepal, D.; Balasubramanian, S.; Simonian, A. L.; Davis, V. A. *Nano Lett.* **2008**, *8*, 1896.

- (14) Gaboury, S. R.; Urban, M. W. *Langmuir* **1993**, *9*, 3225.
- (15) Gaboury, S. R.; Urban, M. W. *Langmuir* **1994**, *10*, 2289.
- (16) Zhao, Y.; Urban, M. W. *Langmuir* **1999**, *15*, 3538.
- (17) Aumsuwan, N.; Danyus, R. C.; Heinhorst, S.; Urban, M. W. *Biomacromolecules* **2008**, *9*, 1712.
- (18) Aumsuwan, N.; Heinhorst, S.; Urban, M. W. *Biomacromolecules* **2007**, *8*, 713.
- (19) Tseng, C. H.; Wang, C. C.; Chen, C. Y. *Chem. Mater.* **2007**, *19*, 308.
- (20) Felten, A.; Bittencourt, C.; Pireaux, J. J.; Van Lier, G.; Charlier, J. C. *J. Appl. Phys.* **2005**, *98*, 074308.
- (21) Chen, Q. D.; Dai, L. M.; Gao, M.; Huang, S. M.; Mau, A. *J. Phys. Chem. B* **2001**, *105*, 618.
- (22) Huang, S. M.; Dai, L. M. *J. Phys. Chem. B* **2002**, *106*, 3543.
- (23) Khare, B. N.; Wilhite, P.; Meyyappan, M. *Nanotechnology* **2004**, *15*, 1650.
- (24) Khare, B. N.; Wilhite, P.; Tran, B.; Teixeira, E.; Fresquez, K.; Mvondo, D. N.; Bauschlicher, C.; Meyyappan, M. *J. Phys. Chem. B* **2005**, *109*, 23466.
- (25) Yu, M.; Urban, M. W. *J. Mater. Chem.* **2007**, *17*, 4644.
- (26) Zalipsky, S.; Gilon, C.; Zilkha, A. *Eur. Polym.* **1983**, *19*, 1177.
- (27) Mole, B. *Plast. Reconstr. Surg.* **1992**, *90*, 200.
- (28) Urban, M. W. *Attenuated Total Reflectance Spectroscopy of Polymers-Theory and Practice*; American Chemical Society: Washington DC, 1996.
- (29) Aumsuwan, N.; Heinhorst, S.; Urban, M. W. *Biomacromolecules* **2007**, *8*, 3525.

CHAPTER VII

CONCLUDING REMARKS

Although a number of efforts focused on smart nanomaterials with sustainable biocompatibility that exhibit stimuli-responsiveness as well as a specific recognition, there are many advances to be made. The majority of studies are concerned with biological systems, where specific recognitions between individual entities were established using a sequence of empirical methods, recognition of synthetic molecules and naturally occurring species remain to be uncharted area. One of the challenges will be how to mimic biologically active species using synthetic materials at molecular levels and in view these considerations and limited literature data, PLs are of particular interest due to their unique structural features, biocompatibility, and the ability to self-assembly, which are capable of forming bilayers, micelles, liposomes, and tubules. The incorporation of biocompatible PL as stabilizing agents into colloidal dispersions offers a potential opportunity to prepare novel biomaterials, which may exhibit stimuli-responsive features and selectively recognitions.

As described in Chapter II and III, PL stratification resulted in the formation of preferentially orientated crystalline entities at p-MMA/nBA film interfaces, which were capable of recognizing MMA/nBA monomer interfaces along the p-MMA/nBA copolymer backbone and crystallizing at the monomer interface. These entities were responsive to external stimuli such as the combined effects of ionic strength, enzyme, and pH, thus affecting their mobility and stratifications. The incorporation of ab initio calculations and spectroscopic studies revealed the origin of PL recognition, where the

two neighboring MMA and nBA units along the polymer backbone provided conducive environments to signal and attract amphiphilic groups of PL.

Furthermore, due to their unique structural and morphological features, PL may serve as templates for developing nanomaterials with tailored properties thus offering novel avenues for creating new materials with diverse shapes which may exhibit stimuli-responsive features. Using bioactive nanotube-forming PL as templates, concentric ferromagnetic magnetite/carbon/magnetite nanotubes (FMNTs) were synthesized and their structural and morphological features were further investigated. Since geometry and size considerations are important factors in achieving desirable magnetic properties and applications, controllable and uniform diameter, wall thickness, and length of FMNTs were obtained using the synthetic approaches. Regardless of the mechanisms of cytotoxicity and antimicrobial activity, size and shape of nano-objects may play an important role which is often difficult or even impossible to control. One approach to minimize geometrical considerations is to chemically modify surfaces of nano-objects and allow surface chemistry overcome cytotoxicity and antimicrobial properties. Thus, the surface modifications of different nano-objects such as C₆₀, multi-walled carbon nanotubes, FMNTs, and carbon fibers were performed to attach polyethylene glycol spacer and penicillin, which resulted in inhibition of gram positive bacteria and cytotoxicity.

As new developments in nanotechnologies progress, the formation of nanomaterials with diverse shapes with sustainable and biocompatible properties continues to be a challenge. The incorporation of bioactive PLs into nanomaterials provides promising opportunities in creating shapes by serving as stabilizing agents for

colloidal dispersions as well as templating of depositing other species, which may open new avenues in development of nanomaterials with various shapes.